PARAMETRIC THERMAL MODELING OF SWITCHED RELUCTANCE AND INDUCTION MACHINES

A Thesis
Presented to
The Academic Faculty

by

Chad Michael Bednar

In Partial Fulfillment
of the Requirements for the Degree
Master of Science in the
G. W. Woodruff School of Mechanical Engineering

Georgia Institute of Technology
May 2014

PARAMETRIC THERMAL MODELING OF SWITCHED RELUCTANCE AND INDUCTION MACHINES

Approved by:

Dr. J. Rhett Mayor, Advisor
G. W. Woodruff School of Mechanical Engineering
Georgia Institute of Technology

Dr. Sheldon Jeter
G. W. Woodruff School of Mechanical Engineering
Georgia Institute of Technology

Dr. Ronald Harley
School of Electrical and Computer Engineering
Georgia Institute of Technology

Date Approved: 11/18/2013

In Dedication to my friends and family

ACKNOWLEDGEMENTS

First, I would like to thank my committee members, Dr. Jeter and Dr. Harley, for their time spent improving this thesis. They have been a great help in my growth as an engineer.

I would like to thank Dr. Habetler, Jie Dang and Yi Du from the Electrical Engineering department for their collaboration. They were always willing to help with this work and answer any electromagnetic questions that arose.

I would like to thank my lab mates, Ben Loeffler, Dr. Jacob Kunz, Howard Liles and Sam Glauber, for their help and collaboration throughout the years.

I would especially like to thank Dr. Andrew Semidey for his help and guidance during my graduate degree. His willingness to help me understand difficult engineering problems and advance me as an engineer was paramount to my success.

Finally, I would like to thank Dr. J. Rhett Mayor. His guidance always encouraged me to become a better engineer. His advice has strengthened my ability to think critically in all situations.

TABLE OF CONTENTS

LIST OF TABLES

LIST OF FIGURES

SUMMARY

This research focuses on the creation of a thermal estimator to be used in an integrated electromagnetic, thermo-mechanical design tool for the rapid optimal initial sizing of switched reluctance and induction machines. The switched reluctance model includes heat generation in the rotor due to core losses, heat transfer across the air gap through convection, and a heat transfer path through the shaft to ambient. Empirical Nusselt correlations for laminar shear flow, laminar flow with vortices and turbulent flow are used to estimate the convective heat transfer coefficient in the air gap. The induction model adds ohmic heat generation within the rotor bars of the machine as an additional rotor heat source. A parametric, self-segmenting mesh generation tool was created to capture the complex rotor geometries found within switched reluctance or induction machines. Modeling the rotor slot geometries in the R-θ polar coordinate system proved to be a key challenge in the work. Segmentation algorithms were established to model standard slot geometries including radial, rectangular (parallel-sided), circular and kite-shaped features in the polar coordinate system used in the R-θ solution plane. The center-node mesh generation tool was able optimize the size and number of nodes to accurately capture the cross sectional area of the feature, in the solution plane. The algorithms pursue a tradeoff between computational accuracy and computational speed by adopting a hybrid approach to estimate three dimensional effects. A thermal circuits approach links the R-θ finite difference solution to the three dimensional boundary conditions. The thermal estimator was able to accurately capture the temperature distribution in switched reluctance and induction machines as verified with experimental results.

CHAPTER 1

INTRODUCTION

1.1 Introduction

The overall goal of the research described herein is to create a multi-physics design tool to size switched reluctance and induction machines by estimating the mechanical, thermal and electromagnetic effects. The final design tool will produce solutions that are physically tractable instead of relying on interpolation between known data points. The design tool sacrifices the overall accuracy of the solution to gain this physical tractability.

A majority of current electric machines are designed to run at constant load and speed as seen in applications such as pumps, conveyor motors, and fans. These machines are selected by the user from predesigned commodity machines that are not specifically designed for the user's individual task. Recently, there has been a push to use electric machines in a wider variety of applications, which requires a more application-specific design approach. Machines may be constrained by volume, speed, weight, or the ambient condition in which they operate. One of the areas of ongoing research is that of high-speed low power electric machines. In general, as the speed of the machine increases, the overall rotor diameter is decreased to reduce the losses due to viscous dissipation, a function of surface rotor speed. Ultra-high speed electric machines are becoming more popular in a variety of industries due to their ability to provide a more uniform torque profile over a large range of speeds. Presently, dental drills use an air turbine drive system that requires multiple tool holders to vary the rotational speed required for different tasks. The air turbines have poor torque curves with low torque values at low and high speeds. An electric drive would give the user control of the speed and provide

better torque performance at start up and at high speed. Precision machining uses tools that are on the micro scale. As the tool diameter decreases, the surface velocity of the cutting edge decreases. A minimum surface velocity is needed to ensure proper cutting and reduction of burr formation, while maintaining acceptable feed rates. The use of ultra-high speed machines for portable power generation and energy storage can reduce the overall mass and volume of the system. Electrically assisted turbochargers are being implemented to reduce the turbo lag experienced at low engine speeds. This ultra-high speed electric machine would be subjected to high temperature due to its connection to the exhaust gas turbine. The unique ambient and boundary conditions of this machine application must be acknowledged during the design of this machine. A few examples of machines that fulfill these application-specific tasks are illustrated in Figure 1.1.

Figure 1.1 - High speed non-commodity electric machine applications: BorgWarner electrically assisted turbocharger (A) [1], Sirona dental tool (B) [2], and NSK electric spindle (C) [3]

Another area of increased research interest is in machines with widely varying load profiles. Inverter-fed machines, such as traction drives used in hybrid electric vehicles (HEV), have time dependent speeds and torque loadings. Increased performance and torque density can be achieved by expanding beyond the 60 Hz operation of line fed machines. Driving machines at higher frequencies produces a new set of challenges. The

steady state rated load assumptions commonly used in the machine design process are no longer valid under these transient operating conditions. Furthermore, core loss, a function of signal frequency, becomes increasing factors in the total loss of the machine. These new challenges need to be addressed in the front-end design of the machine.

The work presented here focuses on the creation of an extended R-θ plane thermal model used for the estimation of thermal gradients within ideal switched reluctance and induction machine design candidates. The enhanced thermal model uses a combination of finite difference and thermal circuits to capture radial and circumferential temperature gradients and axial three dimensional thermal effects and boundary conditions. The thermal module predicts temperature gradients and hot spot locations that can lead to winding insulation failure, magnetic property degradation, and thermo-mechanical stresses. With the increasing demand for application-specific machines, the need to combine the electromagnetic and thermal designs into one intuitive and time efficient design program is inherent.

1.2 Electric Machine Design Process

The design of an electric machine can be broken down into three main categories; electromagnetic, mechanical and thermal. In the current design process, the electrical and mechanical design teams usually work separately resulting in many design iterations before the design is accepted by both groups. Most electric machines used today are designed to run at a constant load and/or speed. This allows the machine to be designed for steady state conditions. The design process used to create these machines produces products that are acceptable, not optimal. The final design usually ends up being

overdesigned to satisfy separately both the electromagnetic and thermal design specifications.

Initial electromagnetic machine sizing is driven by the governing equation, illustrated in (1.1) [4]. In this equation, S is the motor rating, K_{w1} is the winding factor, $\overline{B}$ is specific magnetic loading, ac is the specific electrical loading, D is stator bore diameter, L is active length, and n is rated speed. Electromagnetic sizing using this approach requires a great deal of experience to be efficient. Designers use many rules of thumb and heuristics that cannot be found in textbooks.

$$S = 11 K_{w1} \cdot \overline{B} \cdot ac \cdot D^2 \cdot L \cdot n \tag{1.1}$$

Results from the initial electromagnetic design are given to the mechanical team to size the machine for structural and thermal challenges. The shaft is sized to transmit the produced mechanical power out of the machine as well as hold the rotor concentric to the stator. Efficient machines require a small air gap and accordingly require a stiff shaft to maintain very minimal deflection over its unsupported length. The purpose of the frame of the machine is often thought to be sized primarily to resist the torque produced by the machine; however it is the thermal capacitance that drives its design. This thermal capacitance helps absorbs large spikes in heat generation due to high currents seen during start up or acceleration. Improved machine cooling can be achieved by shortening the conduction length to ambient, or by increasing the convective heat transfer coefficient through the use of internal or external fans. In the typical design approach, detailed thermal analysis is performed using a finite element analysis (FEA) software packages. Furthermore, computational fluid dynamics (CFD) provides a complex analysis tool that can be used to examine the complex air flow within or around the electric machine. The

resulting mechanical design is then either sent back to the electromagnetic design team for tweaking or is further analyzed using FEA or CFD for design finalization. This process, illustrated in Figure 1.2, can take months to complete, due to the separated electromagnetic and mechanical approaches to the design.

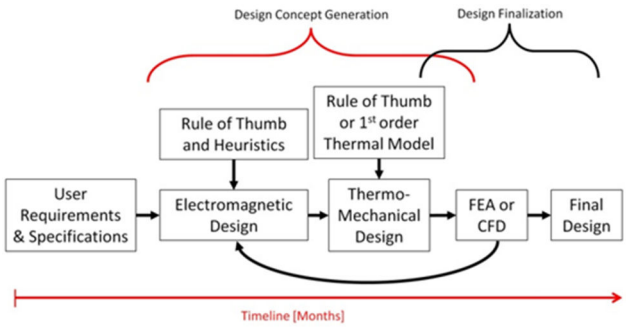

Figure 1.2 - Current design progression of an electric machine [5]

Whereas current machine design uses tables and simple governing equations, the proposed design tool will use a thermal estimation technique for rapid domain searching of machine sizes. This model does not attempt to obtain the same level of accuracy needed to replace a full three dimensional FEA. The overall accuracy is sacrificed in order to reduce the computational power needed to solve the model, thus resulting in shorter solution times. By gaining a better understanding of the electromagnetic and thermal effects simultaneously during the initial sizing, the number of design iterations is expected to decrease drastically. This new design approach, illustrated in Figure 1.3, is tailored to provide an optimal starting point for the design of non-commodity machines. Mayor, Harley, Duan and Semidey hypothesized that this approach would reduce the design phase of the machine from months to weeks.

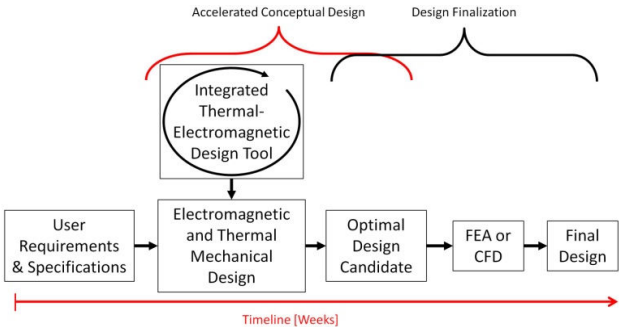

Figure 1.3 - Proposed design approach for non-commodity electric machines [5]

1.3 Motor Topology

Electric machines vary in the way they turn electrical energy into mechanical energy. Permanent magnet machines (PM), switched reluctance machines (SRM), and induction machines (IM) are common types of machines considered for applications such as electric vehicles and are the focus of this work [6]. The components within an electric machine are quite similar in each of the different machine topologies. The source of the magnetic flux within the machine can be permanent magnets, direct electrical current through a coil of wire (winding), or induced current in rotor bars. The magnets, windings, and rotor bars are surrounded by electric steel to concentrate and direct the magnetic field. The pole shoe reduces the gap between two adjacent poles. This reduces cogging by smoothing the transition from one tooth to the next. The back iron provides a pathway for the magnetic flux while also providing structural support for the stator and rotor. The frame is designed to resist the torque created by the machine while also providing thermal capacitance. This thermal capacitance can help absorb large temperature spikes due to startup or acceleration of the machine. The components described are illustrated in Figure 1.4.

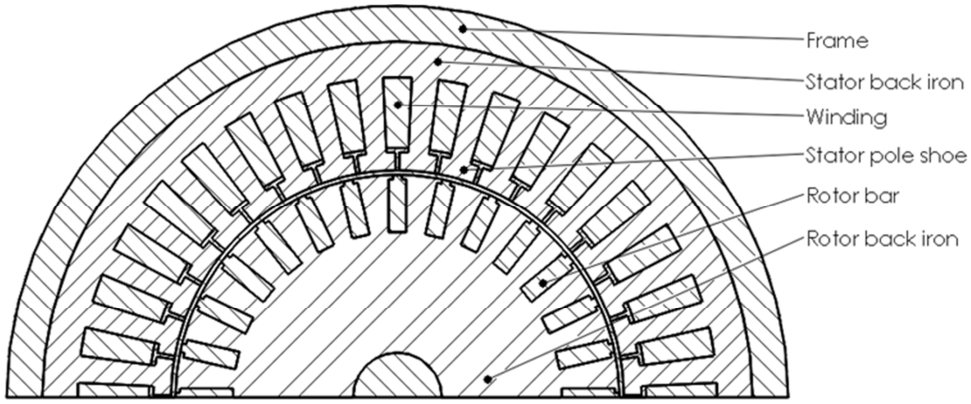

Figure 1.4 - Stator and rotor components of an induction machine

Permanent magnet machines are the simplest to model thermally as rotor heat generation can be assumed to be negligible. The thermal model of the PM machine includes heat generation due to resistive heating in the windings and core loss in the stator back iron. The limited supply and challenges of mining rare earth metals used to produce permanent magnets attributes to the high cost of a PM machine [7, 8]. Therefore, alternative machine topologies have become an increasingly important topic of research.

A switched reluctance machine uses a stator similar to a permanent magnet machine, but the rotor is composed only of electric steel. The common components of a SRM are illustrated in Figure 1.5. Torque is created using magnetic reluctance or the rotor's desire to complete the "magnetic circuit". SRMs do not have permanent magnets or a second set of windings in the rotor, thus greatly reducing the complexity and cost of the machine. The robust construction and low inertia of the monolithic rotor gives the SRM an advantage at higher rotational speeds when compared to the PM machine and IM. SRMs have been identified as a suitable choice for high speed application due to their simple and robust construction. Unlike the peripheral surface of a PM or IM rotor, the rotor of an SRM has exposed bluff body teeth that lead to acoustic noise when rotated. The void in

the off poles of the rotor can be filled with a potting material, as illustrated in Figure 1.5, to reduce the viscous drag and acoustic noise. In a high speed SRM, the physical dimensions are kept small to reduce rotor tip speed, thus reducing acoustic noise and machine losses due to viscous air drag. SRMs are not widely in production due to difficulties with precision manufacturing, bearing forces on small bearings, acoustic noise and a design process that is not optimal [9].

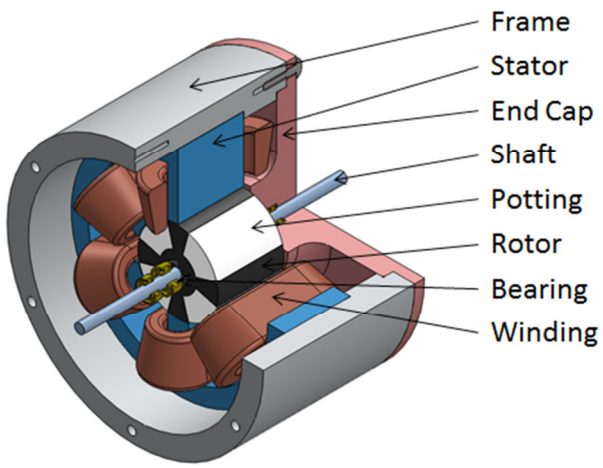

Figure 1.5 - Common components of a switched reluctance machine

An induction machine, illustrated in Figure 1.6, contains windings or rotor bars that are enclosed within the back iron of the rotor. Electrical current is supplied to these windings or rotor bars by electromagnetic induction. The stator creates a rotating magnetic field which induces a current in the windings or rotor bars in the rotor. This current creates separate magnetic fields in the rotor which rotates at a slower speed than that of the stator. This lag or slip results in torque and thus mechanical energy. The set of windings or rotor bars in an IM creates a significant heat source within the rotor, thus adding to the complexity of the thermal model.

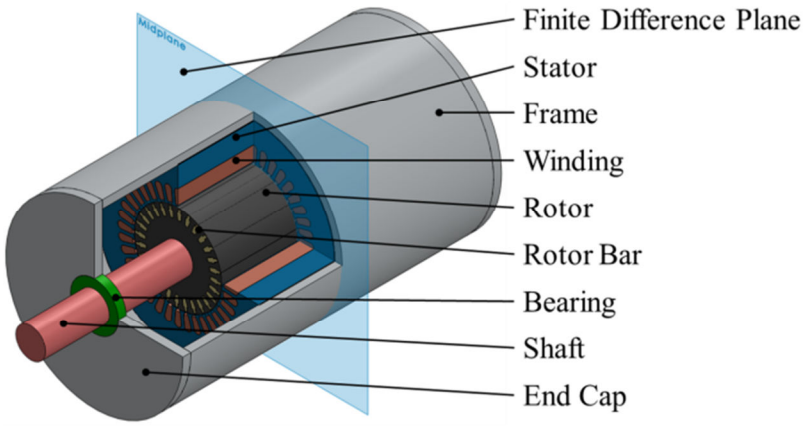

Figure 1.6 - Common components of an induction machine

1.4 Heat transfer

The thermal estimation or analysis of the electric machine can be achieved using many different approaches. Thermal circuit analysis uses a linked combination of thermal resistances values that require experimental values for non-standard geometries to estimate temperature at the nodes. Another approach uses finite element analysis, which involves long setup and computational time. Whilst balancing a tradeoff between model accuracy and solution time, a hybrid finite difference and thermal circuit analysis approach is used in the thermal model to solve the temperature distribution and identify maximum temperature locations in the machine.

Thermal analysis must be performed under steady state and transient conditions to ensure certain components do not overheat. The insulation on the machine windings degrades at temperatures above a certain threshold and can lead to short circuiting. Electric machines are commonly modeled in the R-Z plane, illustrated in Figure 1.7, which simplifies the analysis to a two dimensional problem [10].

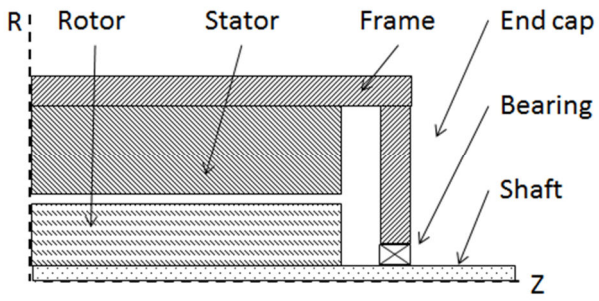

Figure 1.7 - Common R-Z plane used in the thermal solution of electric machines

The electromagnetics need to be solved using the R-θ plane. Therefore, the thermal model in the integrated design tool uses a polar coordinate system to describe the machine. Modeling the rotor slot geometries in the R-θ polar coordinate system becomes a challenge addressed in the mesh generation and segmentation work. The cylindrical heat equation, displayed in (1.2), is used to describe the machine in this coordinate system. The first three terms describe conduction in the radial, circumferential, and axial directions respectively. The last term on the left side of the equation is the energy generation term which includes copper loss, core loss, windage loss and frictional loss. Windage and frictional losses are assumed to be small and therefore not included in the model. The right side of the equation describes the change in stored thermal energy. The steady state assumptions used in commodity machine sizing simplify the heat equation by setting the change in temperature over the change in time to zero.

$$\frac{1}{r}\frac{\partial}{\partial r}\left(kr\frac{\partial T}{\partial r}\right)+\frac{1}{r^2}\frac{\partial}{\partial \phi}\left(k\frac{\partial T}{\partial \phi}\right)+\frac{\partial}{\partial z}\left(k\frac{\partial T}{\partial z}\right)+\dot{q}=\rho C_p\frac{\partial T}{\partial t} \tag{1.2}$$

The interior of the machine includes a variety of materials and non-cylindrical geometries making it difficult to solve the equation analytically.

Whilst conduction is used to describe the heat transfer through the solid material in the machine, convection is used to describe the heat transfer in the air gap and on the

surface of the frame, shaft, and end caps. Natural convection is due to buoyancy forces, whilst forced convection is produced by an external means such as a shaft mounted fan.

1.5 Research Objectives

The work of Mayor and Semidey established a successful method for estimating the temperature distribution in the stator of a permanent magnet machine. Their work did not include model the rotor, the air gap heat transfer, or the thermal transport through the shaft. Switched reluctance and induction machines require these components to be accounted for in the thermal model as rotor heat generation become significant. The first objective of this work is to establish the algorithms needed to transform common rotor geometries in to polar coordinates. This includes how to sufficiently size the mesh nodes to accurately capture the cross section area of the features. A second objective is to develop a method for capturing the heat transfer between the stator and rotor across the air gap. The final objective is to develop a method to capture the heat rejection through the shaft to the ambient.

1.6 Thesis Organization

This chapter describes the details of the proposed thermal estimator for switched reluctance and induction machines. Chapter 2 provides a detailed review of the salient literature. Chapter 3 describes the algorithms that generate the finite difference mesh and segment the common rotor geometries. Chapter 4 details the hybrid finite difference and thermal circuits thermal model of switched reluctance machines including rotor heat generation, air gap heat transfer, and heat rejection through the shaft. Chapter 5 advances the thermal model to include the rotor bar heat generation found in induction machines. Chapter 6 presents the conclusions, contribution, and recommended future work.

CHAPTER 2

REVIEW OF SALIENT LITERATURE

2.1 Introduction

A detailed literature survey was conducted to gain a better understanding of electric machine thermal modeling approaches for electric machines, heat transfer between concentric rotation cylinders and heat transfer in ball bearings.

The thermal modeling of electric machines has been widely studied and has focused on analysis of temperature profiles in the machine. The ability to effectively remove heat from the motor is an important factor in machine performance and torque density. The frame of the motor resists the torque created by the motor, but more importantly provides thermal storage to prevent overheating. The heat generated within the machine from copper, core, friction and windage losses is dissipated through convection and radiation on the surface of the frame and shaft. Fins on the frame increase the surface area for convection thus allow more heat to be dissipated. Fans used to create forced convection increase the convective coefficient thus provide more efficient heat transfer.

2.2 Electric machine design

With the high cost of rare earth materials, many researcher are looking into machine topologies with less or no permanent magnets such as induction and switched reluctance machines [11]. The use of SRMs in many applications is limited by inadequate knowledge of the design procedures instead on technical deficiencies [12, 13].

There are many different areas of interest in designing an electric machine include electromagnetic, thermal, and mechanical. Kunz et al investigated viscous air losses,

rotating natural frequencies, bearing reaction loads, centrifugal forces, and copper and core losses in the design of a ultra-high speed switched reluctance machine [14].

2.3 Electric machine thermal modeling

2.3.1 Thermal circuits

Mellor et al proposed using thermal circuits to model the temperature distribution in an electric machine [15]. The thermal circuit approach replaces the components and interfaces within the machine with calculated thermal resistance values. While some of the resistance values can be calculated from the geometric and material parameters, others must be obtained through experimentation. Researchers continually increase the number of resistance values in the thermal network to capture the complex heat transfer in certain components [16-18]. Kral et al developed an improved thermal lumped element network that corrects the thermal resistance values with an embedded temperature sensor but the model still requires experimental data [19].

In the motor design software package Motor-CAD, a lumped-circuit analysis is used to solve the temperature distribution. A screenshot of the thermal circuit diagram for a permanent magnet machine using Motor-CAD is illustrated in Figure 2.1.

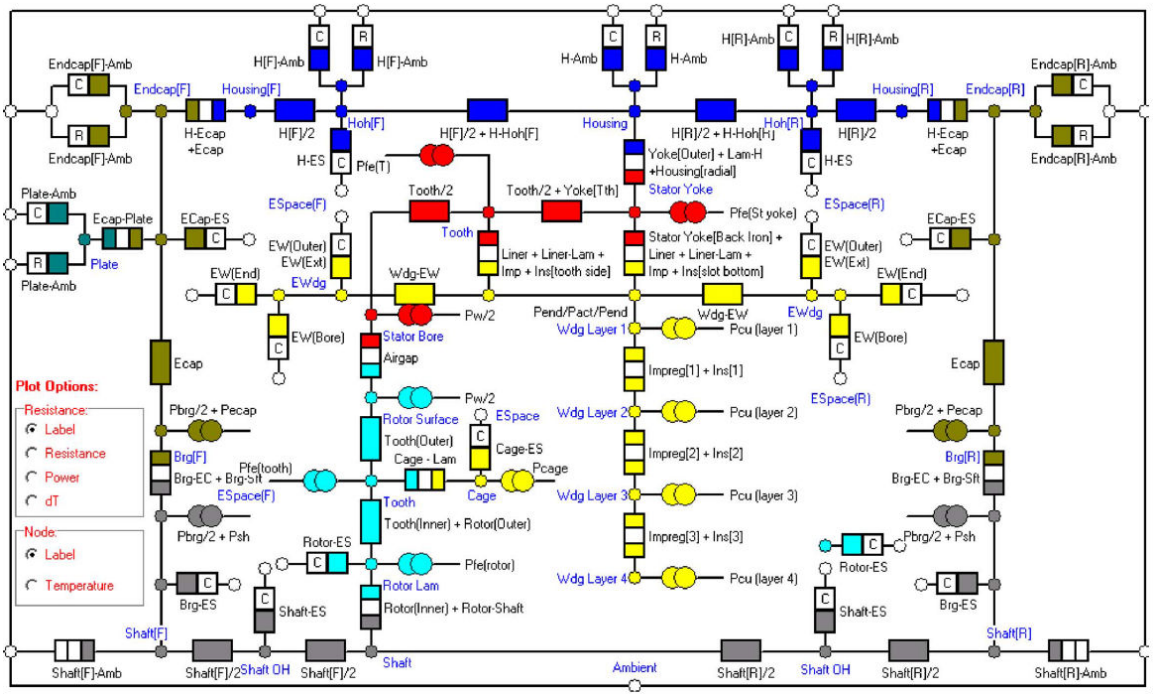

Figure 2.1 - Lumped thermal circuit diagram from Motor-CAD [20]

The need for certain thermal resistance values to be determined or verified through experimentation hinders the lumped thermal circuit approach as an initial design tool.

2.3.2 Finite element analysis

Another approach, finite element analysis (FEA), converts the physical machine into small individual elements and produces a solution using the interactions between elements. This approach can produce accurate results for complicated geometries but requires a large amount of computational power and time. The overall solution time must not only consider the analysis solution time, but also the setup time involved in creating the computer aided design (CAD) models. The high accuracy of FEA makes it an ideal choice as an analysis tool, such as the thermal cycling study conducted by Sun et al [21]. FEA is used to determine temperature distribution in a specific machine under various design modifications, load condition and boundary conditions [22-24]. The tedious setup

and larger computational power required by FEA does not make it an ideal choice for the rapid initial design selection for electric machines.

2.3.3 Computational fluid dynamics

Computation fluid dynamics (CFD) is a powerful tool commonly used to determine heat transfer coefficients in electric machines. It is helpful in model fluid flow through complex channel that are not easily described by analytical formulations. Jungreuthmayer et al uses CFD in conjunction with FEA to model the complex heat transfer in the water jacket of a radial flux permanent magnet synchronous machine [25]. Whilst CFD is ideal for complex heat transfer analysis, it is not well suited for rapid thermal estimations used in initial design candidate selection.

2.3.4 Finite difference

Finite difference uses thermal circuits between adjacent nodes to solve the temperature distributions. Whilst FEA is the common choice for thermal analysis, Park et al used a linked thermal network to estimate the temperature distribution in a traction motor for thermal life estimations [26]. Finite difference is an ideal choice for design optimization due to its ability to be parametric and fast solving. Semidey et al combined the electromagnetic, thermal and mechanical design factors into a single model to optimally design surface-mount permanent-magnet machines [4, 5, 27-30]. However, this model is only for the design of surface mount permanent magnet machines.

2.4 Air gap heat transfer

The heat transfer in the annulus between rotating concentric cylinder has been a widely researched topic. The heat transfer correlations in the air gap are used link the rotor and stator. In 1935, Taylor was the first to research the heat transfer and velocity

profile between two concentric rotating cylinders [31]. The velocity radius product remained constant for a majority of the annulus as illustrated in Figure 2.2. The temperature distribution, illustrated in Figure 2.3, exhibits higher temperature in the boundary layers when compared to the center of the annulus.

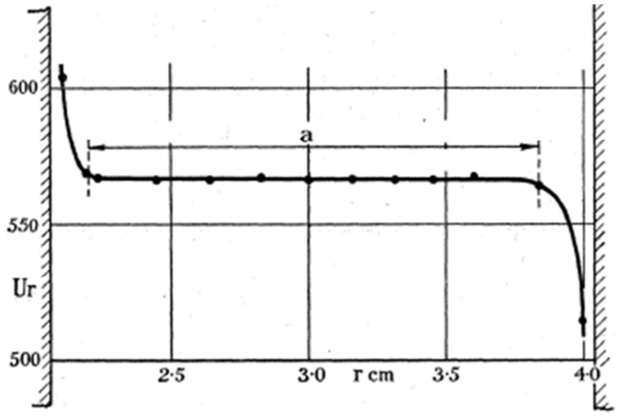

Figure 2.2 - Velocity radius product distribution in the annulus of two rotating concentric cylinders [31]

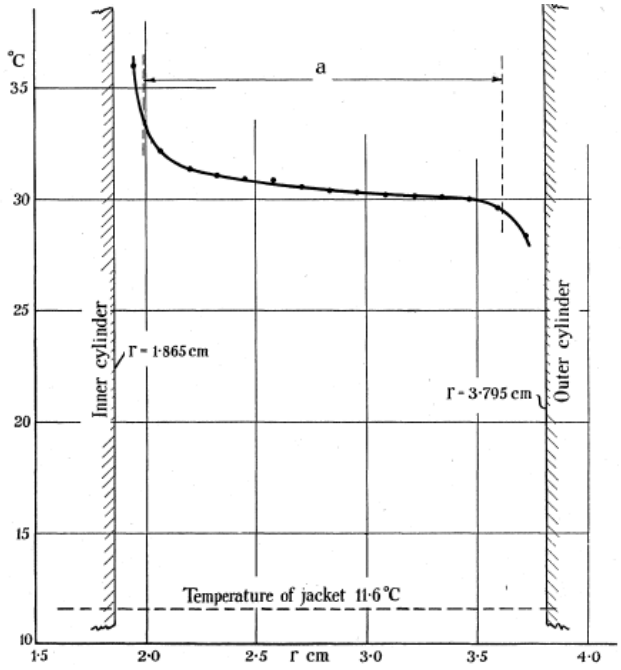

Figure 2.3 - Temperature distribution in the annulus of two rotating concentric cylinders [31]

The air gap thicknesses for the velocity profile and temperature profile experiments conducted by Taylor were 1.973 cm and 1.93 cm respectively. This is larger than the air gap thickness commonly seen in low voltage electric machines.

Further research into the heat transfer between two concentric rotating cylinders has been performed to understand the effects that certain parameters have on the heat transfer [32-41]. Ball et al expanded upon Taylor's results by conducted experiments using air as the medium in the annulus between the two concentric cylinders [42]. Correlations were given for the effective thermal conductivity of the air gap and the transition from buoyancy dominated flow to rotational driven flow was examined. The work is expanded from the research conducted by Walowit et al on the stability of Couette flow in the annulus of two concentric rotating cylinders [43]. Ball also conducted smoke visualization of the flow in the annulus of the cylinders as illustrated in Figure 2.4.

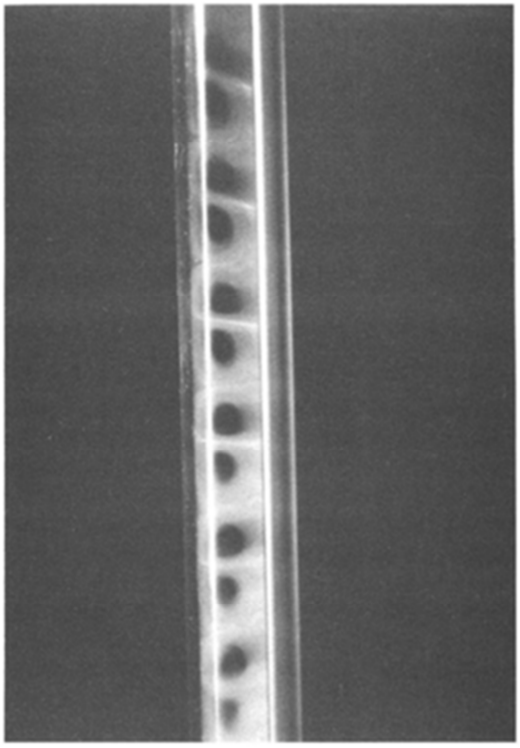

Figure 2.4 - Visualization of Taylor vortices in a vertical annuls [42]

Hayase et al extended the study of the convective heat transfer between rotating cylinders to include embedded cavities on the inner and outer cylinders as would be seen in electric machines [44]. The flow in the air gap can be broken into cavity flow and Taylor vortex flow as illustrated in Figure 2.5. The highest Nusselt number occurs at the trailing corner of the cavity and at supercritical Reynolds numbers, the Taylor vortex flows interact with the recirculating cavity flow to increase the overall heat transfer. It was concluded that at supercritical Reynolds numbers the heat transfer intensity was increase by a factor of 1.1 for the cylinder with outer cavities and by a factor of 1.2 for the cylinder with inner cavities.

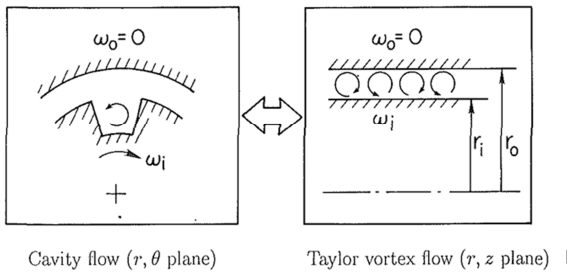

Figure 2.5. Separation of cavity flow and Taylor vortex flow in the air gap [44]

In many of the electric machine thermal analyses, such as the FEA performed on a water cooled induction machine by Cuiping et al, the heat transfer in the air gap is simplified by using an effective thermal conductivity [45].

The trend of the previously described research has been to study the heat transfer in air gaps with decreasing size. The size of the air gap commonly seen in electric machines is on the magnitude of hundreds of micrometers. Howey et al provides a review of heat transfer within the electric machines sized air gaps for three different flow regimes: laminar shear flow, laminar flow with vortices and turbulent flow [46]. The Nusselt

correlations for the air gap, Nu_{ag}, for the three different flow regimes described in (2.1)-(2.3) are used to calculate the convective heat transfer coefficient used in the thermal estimator.

$$Nu_{ag} = \frac{2\left[\left(R_{s,i} - R_{r,o}\right)/R_{r,o}\right]}{\ln\left[1+\left(R_{s,i} - R_{r,o}\right)/R_{r,o}\right]} \tag{2.1}$$

$$Nu_{ag} = 0.128\left(Ta^2 / F_g{}^2\right)^{0.367} \tag{2.2}$$

$$Nu_{ag} = 0.409\left(Ta^2 / F_g{}^2\right)^{0.241} \tag{2.3}$$

The ratio of the Taylor number, Ta, and the geometric factor, F_g, determine the flow regime in the air gap defined by the outer rotor surface, $R_{r,o}$, and the inner stator radius, $R_{s,i}$.

2.5 Ball bearing heat transfer

Sources of heat loss in bearings include elasticysteresis, differential sliding, spinning sliding, viscous traction, friction between ball and cage, and sliding friction between cage and surface. The sliding friction between the balls and the cage produce the largest percentage of heat in a ball bearing [47]. Wang et al also concluded that rotational speed and axial load have a greater effect on the internal heat generation of the bearing when compared to the radial load. The internal heat generation and heat transfer of ball bearings are difficult to define due to the large number of variable include bearing dimensions, bearing loading and material properties [48-51]. Nakajima et al provides useful thermal resistance values, $R_{t,b}$, for bearings under various axial and radial loads [52]. These thermal resistance values provide a starting point for the calculation of the effective thermal conductivity of the bearing, $k_{b,eff}$, as described in (2.4).

$$k_{b,eff} = \frac{\ln\left(R_{b,o} / R_{b,i}\right)}{2\pi \cdot W_b \cdot R_{t,b}} \tag{2.4}$$

The bearing is modeled as a hollow cylinder with an inner radius, $R_{b,i}$, an outer radius, $R_{b,o}$, and a width, W_b. The bearing effective thermal conductivity is used to model the bearings in the proposed thermal estimator.

2.6 Summary

The completed detailed literature survey has shown that there is much research in the areas of detailed design and heat transfer analysis of electric machines. However, there is a need for tool that can rapidly estimate the temperature distributions in induction and switched reluctance machines. This proposed tool is not meant to replace finite element analysis and computational fluid dynamics used for detailed analysis, but rather is to be used to select ideal design candidates for further analysis. A review of the heat transfer in the annulus of two concentric rotating cylinders has provided analytical equations for the determination of convective heat transfer coefficients to be used in the thermal estimator. A range of empirical thermal resistance values for ball bearings under various loads provides data needed to estimate the effective thermal conductivity of the bearings to be used in the thermal estimator.

CHAPTER 3

MESH GENERATION AND SEGMENTATION

3.1 Introduction

The purpose of this chapter is to address the unique challenge of thermal modeling design geometries typically encountered in standard rotor designs of either SRMs or IMs as illustrated in Figure 3.1. These geometries cannot be modeled using the simple radial and angular line of a polar mesh. New segmentation algorithms are required to address the key challenge of modeling rectangular (parallel-sided), circular and kite-shaped geometries found in standard SRM and IM rotors. Since the number of rotor teeth and stator teeth differ in a machine, the addition of the rotor in the model produces a new challenge of having two different sets of adiabatic boundary lines.

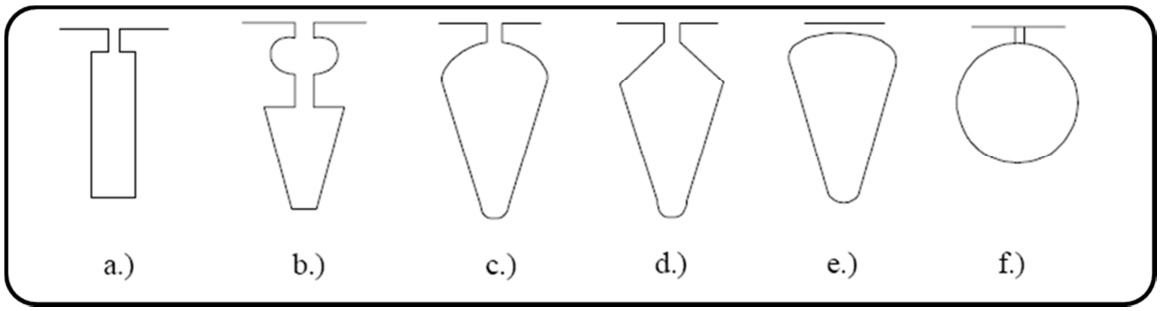

Figure 3.1 - Common rotor bar geometries for induction machines [53]

Whereas traditional thermal models for electric machines are solved in the R-Z plane, the proposed thermal model solves the temperature distribution in the R-θ plane. The use of the R-θ plane, the standard coordinate plane for electromagnetic analysis and simulation of electric machines, allows for the future integration of the proposed thermal model into a multi-physics machine model. The geometric features found in the R-Z plane of an electric machine can be meshed using generic rectangular nodes. Conversely,

rectangular and angular features become difficult to model in the polar coordinates used in the R-θ plane. The mesh generation and segmentation tool must be automated, parametric, self-segmenting. The correlation between the number/size of the nodes and accuracy of the mesh is also examined in this chapter. The center-node mesh generation tool must determine the size and number of nodes to accurately capture the component's area and geometric features while maintaining quick computational time.

3.2 Prior work

Mayor and Semidey pioneered the use of the half slot technique in thermal models, which uses adiabatic boundaries in the machine to greatly reduce the solution space needed in solving the temperature distribution in the R-θ plane [5, 27, 28]. The adiabatic lines of symmetry in a stator of a machine and the resulting half slot are illustrated in Figure 3.2. To further simplify the model, geometric fillets were ignored and the windings were modeled as a monolithic solid (i.e. high packing factor or potted windings) instead of a group of individual wires. The modeling of the rotor was not included in this previous work because it was specific to permanent magnet machines in which heat generated in the rotor can be assumed to have a negligible effect on the thermal response of the entire PM machine.

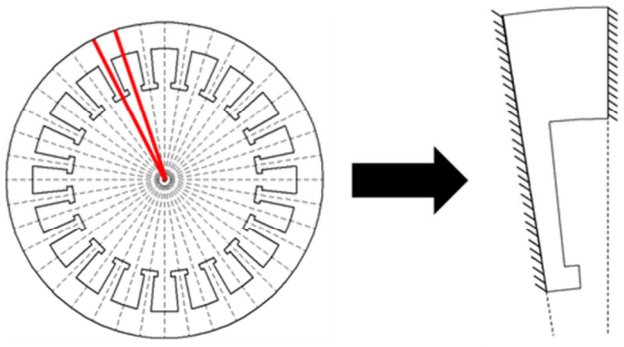

Figure 3.2 - Stator adiabatic lines of symmetry and resulting stator half slot [5]

The stator features were transformed into simple radial and angular dimensions that were simple to model in polar coordinates as illustrated in Figure 3.3.

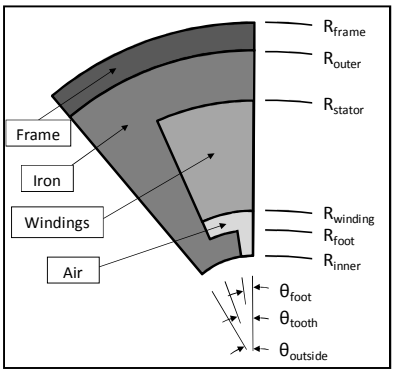

Figure 3.3 - Simplified segmentation of the stator of an electric machine [5]

The stator of an electric machine is similar in the three machine topologies of interested; permanent magnet, switched reluctance and induction. In permanent magnet machines the losses in the rotor are assumed to be negligible in comparison to those in the stator. Therefore the rotor was not included in the previous permanent magnet machine thermal modeling. Switched reluctance machines exhibit rotor core loss and thus warrants the addition of the rotor to the thermal model. The core loss in the rotor is a function of flux density and switching frequency; thus becomes large for very high speed machines. Induction machines exhibit rotor core loss and ohmic losses in the rotor bars. The rotor bars in an induction machine can very complex in shape to combat skin effects affecting the current distribution during start-up and acceleration of the machine under load. The complex geometries are difficult to model in polar coordinates as the features cannot be described by the radial and circumferential lines of a polar mesh. The segmentation of the rotor bars in the mesh required new algorithms to estimate their cross-sectional area.

3.3 Mesh generation and segmentation algorithm

The initial mesh generation module for the finite difference thermal model was created to examine the rotor separately from the stator. The stator and rotor models have their own mesh generation algorithms leading to a discrepancy in the size and number of nodes at the air gap interface. The stator and rotor solution spaces are greatly reduced by using the half slot method; however this results in challenges in connecting and linking the two separate sub models.

The mesh generation and segmentation algorithms can be adapted to include the rotor and stator in the same mesh. The dimensional values for the half slot of the rotor and stator are copied to encompass the entire circumferential span of the half machine. Although electric machines commonly have different number of stator and rotor teeth, the number of teeth is usually an even number and can be simplified by modeling a half machine.

The mesh generation algorithm starts with user defined geometric parameters and the desired radial step size of the nodes. The radial step size is set as a percentage of the air gap diameter. The mesh convergence study to determine the step size that balances model accuracy and computational time is discussed later. The number of radial nodes, N_r, is described using the difference between the outer radius of the frame, R_f, and the outer radius of the shaft, R_s, and the radial step value of dr as displayed in (3.1).

$$N_r = round\left(\frac{R_f - R_s}{dr}\right) \tag{3.1}$$

The angular step size, $d\theta$, is calculated in such a way that the resulting nodes in the middle of the mesh are square as displayed in (3.2).

$$d\theta = \frac{2dr}{R_f - R_s} \tag{3.2}$$

The number of nodes in the circumferential direction, N_c, is calculated using the angular span of the solution space, θ_s, and the circumferential step size as displayed in (3.3).

$$N_c = round\left(\frac{\theta_s}{d\theta}\right) \tag{3.3}$$

The total number of nodes in the mesh, N_t, is defined as the product of the number of nodes in the radial, N_r, and circumferential direction, N_c, as displayed in (3.4).

$$N_t = N_r \times N_c \tag{3.4}$$

The resulting initial mesh generation is illustrated in Figure 3.4.

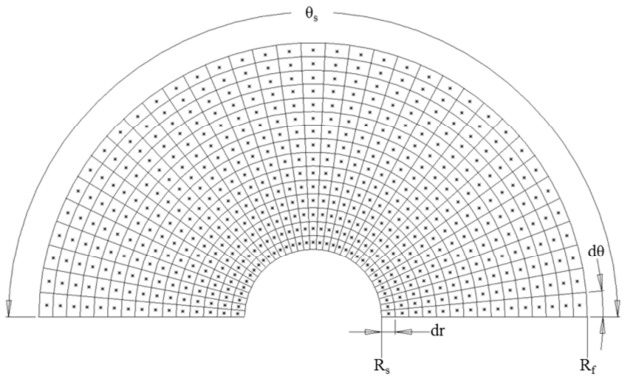

Figure 3.4 - Initial mesh generation for a section of the electric machine

The mesh is segmented in sections defined by feature boundaries. The number of radial nodes in each segment, $N_{r,i}$, is established using bounding radial dimensions of the segment, R_i, and the radial step size, as illustrated in (3.5). The step size, dr, for each segment must then be reevaluated to ensure uniform spacing within the segment as illustrated in (3.6). The radial dimensions for the center of the nodes are combined into a

radial vector, $\vec{R}_{seg,i}$, as illustrated in (3.7).The number of nodes, modified step size and angular location for the circumferential nodes are calculated using a similar approach as the radial nodes as illustrated in (3.8)- (3.10).

$$N_{r,i} = round\left(\frac{R_{i+1} - R_i}{dr}\right) \tag{3.5}$$

$$dr_i = \frac{R_{i+1} - R_i}{N_{r,i}} \tag{3.6}$$

$$\vec{R}_{seg,i} = \left[R_i + \frac{dr_i}{2} : dr_i : R_{i+1} - \frac{dr_i}{2}\right] \tag{3.7}$$

$$N_{\theta,i} = round\left(\frac{\theta_{i+1} - \theta_i}{d\theta}\right) \tag{3.8}$$

$$d\theta_i = \frac{\theta_{i+1} - \theta_i}{N_{\theta,i}} \tag{3.9}$$

$$\vec{\theta}_{seg,i} = \left[\theta_i + \frac{d\theta_i}{2} : d\theta_i : \theta_{i+1} - \frac{d\theta_i}{2}\right] \tag{3.10}$$

The individual radial and circumferential segments and their step values are concatenated into their respected radial or circumferential vectors displayed in (3.11)-(3.14).

$$\vec{R} = \left[\vec{R}_{seg,1}, \vec{R}_{seg,2}, \vec{R}_{seg,3}, ...\vec{R}_{seg,end}\right] \tag{3.11}$$

$$\vec{\theta} = \left[\vec{\theta}_{seg,1}, \vec{\theta}_{seg,2}, \vec{\theta}_{seg,3}, ..., \vec{\theta}_{seg,end}\right] \tag{3.12}$$

$$\overrightarrow{dr} = \left[dr_1, dr_2, dr_3, ...dr_{end}\right] \tag{3.13}$$

$$\overrightarrow{d\theta} = \left[d\theta_1, d\theta_2, d\theta_3, ...d\theta_{end}\right] \tag{3.14}$$

The system of nodes is converted from a matrix to a vector to reduce the computational time. Each node is assigned a unique numerical value that corresponds to its radial and circumferential location in the matrix as illustrated in Figure 3.5.

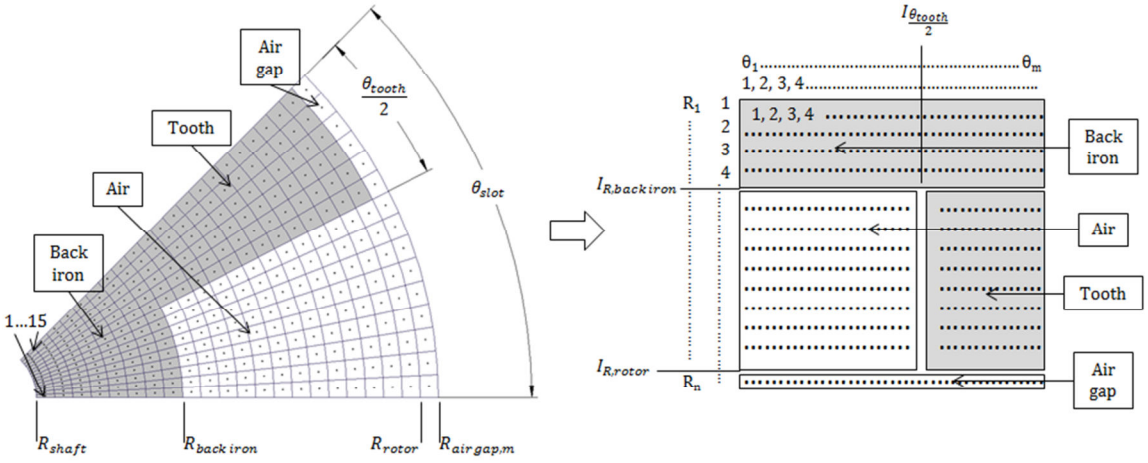

Figure 3.5 - Conversion of the rotor half slot nodes in polar coordinates to an indexed matrix of nodes

3.4 Meshing of Typical IM or SRM Rotor Features

The rotor geometries found in switched reluctance or induction machines that do not align with the radial and circumferential boundaries of the mesh become a challenge to segment. Many of these complex geometries can be modeled using a combination of primitive geometric features including wedge, kite-shaped, rectangular, and circular configurations illustrated in Figure 3.6. This section of work focuses on the creation of segmentation algorithms to capture the cross-sectional area of these features. These complex shapes are difficult to model in polar coordinates but are usually a combination of certain primitive geometric features described previously.

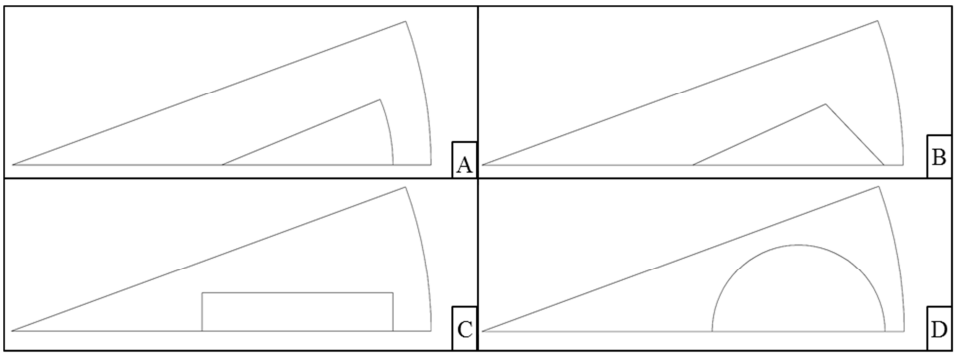

Figure 3.6 - Common rotor bar geometries found in SRM or IM

3.4.1 Wedge-type rotor geometry

Many of the common rotor bar geometries include angles that do not correspond with the angular lines of the overall machine. In polar coordinates, these angles must be estimated using a stair step approach. Figure 3.7 illustrates the dimensional parameters used to describe the wedge geometry.

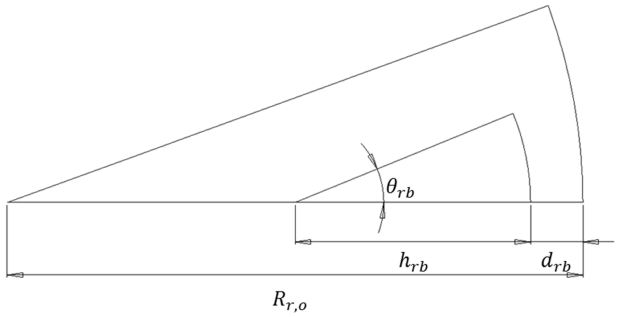

Figure 3.7 - Bounding descriptors for the wedge geometry

The inner and outer rotor bar radii, $R_{rb,i}$ and $R_{rb,o}$ respectively, are calculated given the depth and the height of the rotor bar, d_{rb} and h_{rb}, respectively, as illustrated in (3.15)-(3.16).

$$R_{rb,i} = R_{r,o} - d_{rb} - h_{rb} \tag{3.15}$$

$$R_{rb,o} = R_{r,o} - d_{rb} \tag{3.16}$$

The interpolation algorithm is bounded by the upper angle, θ_1, which is calculated using (3.17).

$$\frac{R_{rb,o}\sin(\theta_1)}{R_{rb,o}\cos(\theta_1) - R_{rb,i}} = \tan\theta_{rb} \tag{3.17}$$

The center locations of the nodes to be segmented as part of the wedge lie within the circumferential segment described by (3.18).

$$\vec{\theta}_{seg} = \frac{d\theta_1}{2} : d\theta_1 : \theta_1 - \frac{d\theta_1}{2} \tag{3.18}$$

The lower radial values for each circumferential segment, R_{step}, are used to create the jagged boundary between the wedge feature and the rest of the rotor. This radial step value for the i^{th} circumferential segment is given by (3.19)

$$R_{step,i} = \frac{x_{1,i} + R_{rb,i}}{\cos\left(\vec{\theta}_{seg,i}\right)} \tag{3.19}$$

where

$$x_{1,i} = \frac{R_{rb,i} \tan\left(\vec{\theta}_{seg,i}\right)}{\tan\left(\theta_{rb}\right) - \tan\left(\vec{\theta}_{seg,i}\right)}. \tag{3.20}$$

The results from the radial step calculations are exact radial dimensions. The node closest to the wedge boundary for each angle is found using (3.21)-(3.22).

$$\vec{r}_{diff,i} = \vec{r}_{seg} - R_{step,i} \tag{3.21}$$

$$I_i = \min\left(\vec{r}_{diff,i} \geq 0\right) \tag{3.22}$$

For each angular step, the nodes from r_{seg,I_i} to $R_{rb,o}$, and from 0 to $\theta_{seg,i}$, are segmented as part of the wedge. The algorithm created to segment the nodes of the wedge is illustrated in Figure 3.8.

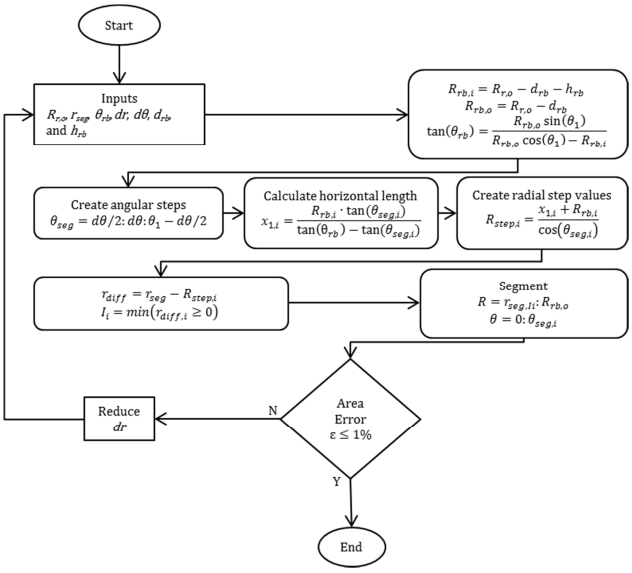

Figure 3.8 - Segmentation algorithm for the wedge geometry

A result of the segmentation using the described algorithm is illustrated in Figure 3.9. The dimensions for this particular case are an outer rotor radius of 100 mm, a feature depth of 5 mm, a feature height of 45 mm and an angle of 45°.

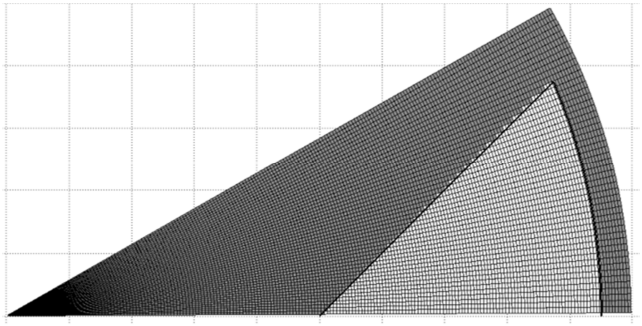

Figure 3.9 - Mesh generation and segmentation results for the wedge geometry

This case was meshed using a radial step size of 0.5% of the outer rotor radius and produced an area error of 0.0814%. A study investigating a variety of radial step sizes was conducted using the dimensions discussed previously. The error is calculated using the actual area of the feature compared with the combined area of nodes segmented in the

algorithm. The area percentage error for the radial step sizes for the wedge geometry is illustrated in Figure 3.10.

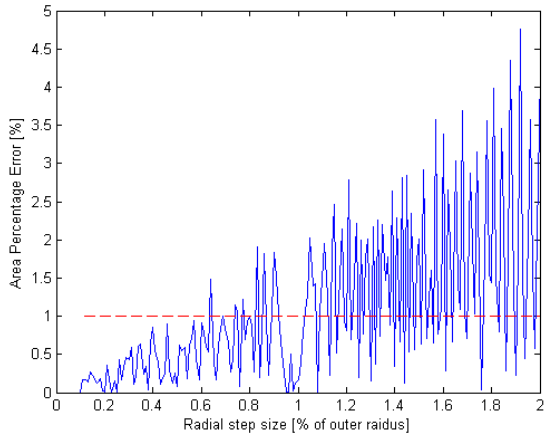

Figure 3.10 - Area percentage error of the wedge feature with varying radial step sizes

The area percentage error increases with larger radial step size as is expected. An error of less than 1% was found for radial step sizes less than about 1.0% of the outer rotor radius. A balance between model accuracy and computational time is desired. The computational times for each radial step size are illustrated in Figure 3.11.

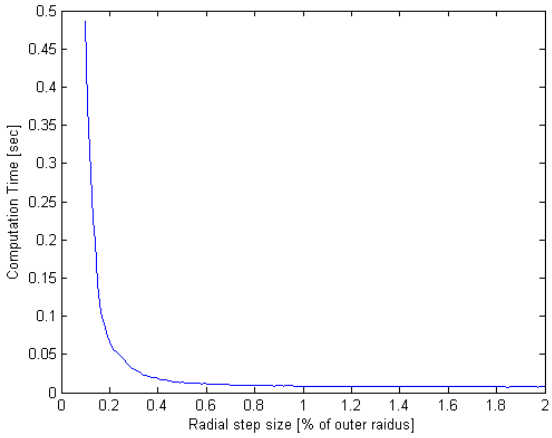

Figure 3.11 - Computational time for the wedge feature with varying radial step sizes

As expected, the error decreases and computational time increases as the size of the radial step decreases. The computational time reaches a lower asymptote at about 0.6% of the outer rotor radius. Further investigation was conducted to determine the effects the angle of the wedge have on the area error percentage. The results for angles between 2° and 55° are illustrated in Figure 3.12.

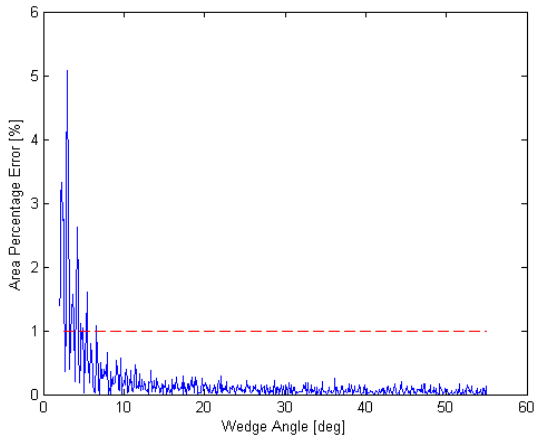

Figure 3.12 - Area percentage error for the wedge feature with varying wedge angles

The model produced relatively large errors for small angles (<10°). The segmentation algorithm is unable to accurately capture the small angles because the angle approaches the size of the circumferential step value. This error can be remedied by reducing the radial step size and thus reducing the circumferential step size.

3.4.2 Kite-shaped feature

The kite-shaped rotor bar geometries have similar primitive descriptors as the wedge-feature rotor bar geometries as illustrated in Figure 3.13. The addition of another wedge feature requires a slight modification of the segmentation algorithm.

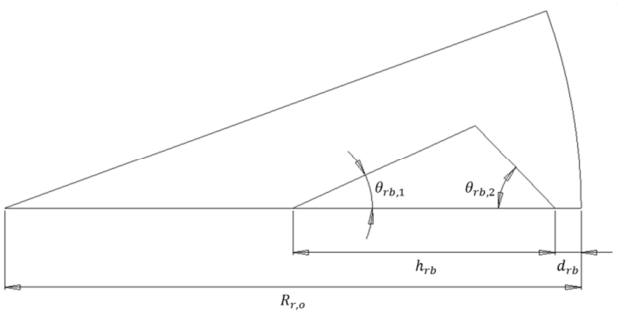

Figure 3.13 - Bounding descriptors for the kite-shaped geometry

The outer boundary for the inner wedge, $R_{rb,m}$, and the bounding upper angle, θ_{l_i}, are determined using (3.23)-(3.29).

$$\theta_t = \pi - \theta_{rb,1} - \theta_{rb,2} \tag{3.23}$$

$$R_{rb,s,i} = \frac{h_{rb}\sin(\theta_{rb,2})}{\sin(\theta_t)} \tag{3.24}$$

$$R_{rb,s,o} = \frac{h_{rb}\sin(\theta_{rb,1})}{\sin(\theta_t)} \tag{3.25}$$

$$x = R_{rb,s,i}\cos(\theta_{rb,1}) + R_{rb,i} \tag{3.26}$$

$$y = R_{rb,s,o}\sin(\theta_{rb,1}) \tag{3.27}$$

$$R_{rb,m} = \sqrt{x^2 + y^2} \tag{3.28}$$

$$\theta_1 = \tan^{-1}\left(\frac{y}{x}\right) \tag{3.29}$$

The circumferential segments and the segmentation of the inner wedge are accomplished using the same approach as discussed in the wedge algorithm. The outer wedge is segmented using (3.30)-(3.32).

$$x_2 = R_{rb,s,o}\cos\left(\theta_{rb,2}\right) \tag{3.30}$$

$$x_{3,i} = \frac{x_2\tan\left(\theta_{rb,2}\right) - x\tan\left(\bar{\theta}_{seg,i}\right)}{\tan\left(\bar{\theta}_{seg,i}\right) + \tan\left(\theta_{rb,2}\right)} \tag{3.31}$$

$$R_{step,2,i} = \frac{x + x_{3,i}}{\cos\left(\bar{\theta}_{seg,i}\right)} \tag{3.32}$$

The identification of the closest node for the resulting radial step value is performed using a modified version of (3.21) and (3.22). Similar to the inner wedge, the nodes from $R_{rb,m}$ to $r_{seg,I_{upper}}$ for each circumferential step are segmented as part of the outer wedge. The algorithm for the kite-shaped feature, illustrated in Figure 3.14, separates the rotor bar into two wedges for separate segmentation. The segmentation of the inner wedge is similar to that of the wedge described in the previous section with the exception of the outer defining radius of the wedge.

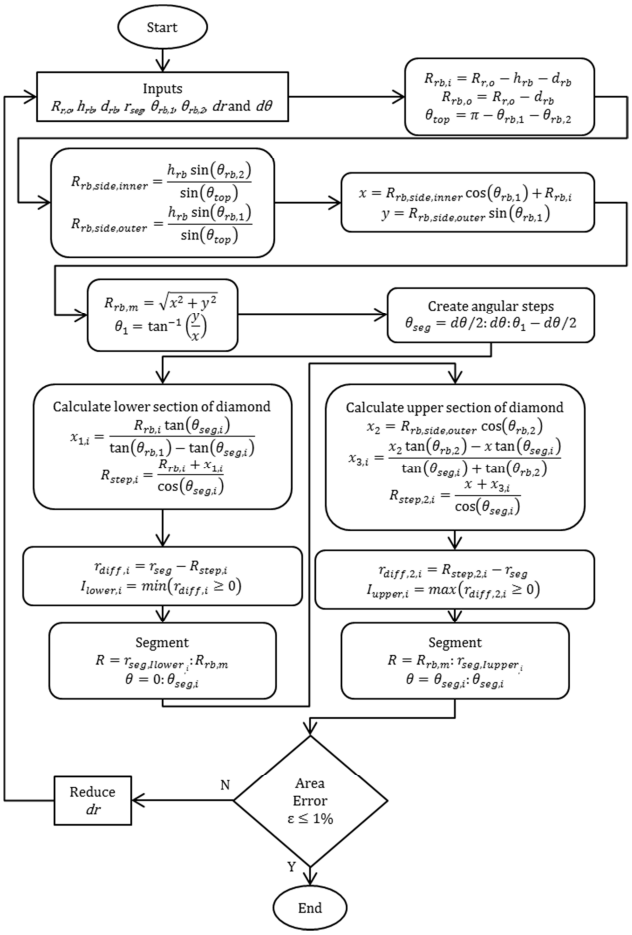

Figure 3.14 - Segmentation algorithm for the kite-shaped geometry

A result from the segmentation of a kite-shaped feature is illustrated in Figure 3.15. The dimensions for this particular case are an outer rotor radius of 100 mm, a feature depth of 5 mm, a feature height of 50 mm, an inner angle of 30°, and an outer angle of 45°.

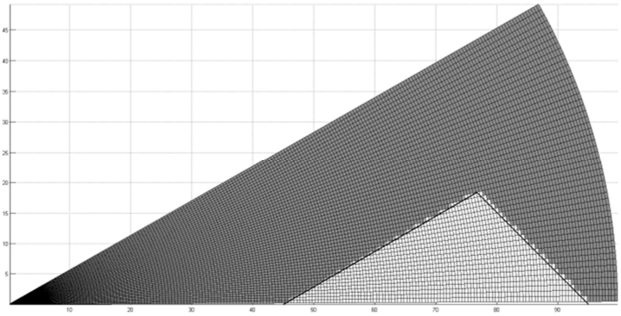

Figure 3.15 - Mesh generation and segmentation results for the kite-shaped geometry

This case was meshed using a radial step size of 0.5% of the outer rotor radius and produced an area error of 0.0277%. This error is less than that of the wedge example. This is not expected due to the estimation of two boundaries instead of one as in the wedge feature example. The area percentage error from the variety of radial step sizes, illustrated in Figure 3.16, is noisy. This noise may contribute to difference in errors when comparing to individual cases.

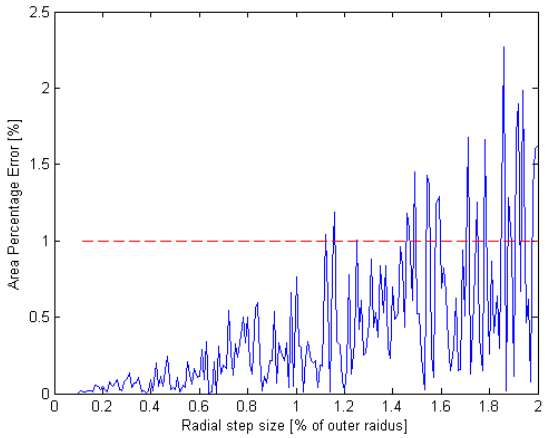

Figure 3.16 - Area percentage error of the kite-shaped feature with varying radial step sizes

An error of less than 1% was found for radial step sizes less than about 2.0% of the outer rotor radius. The corresponding computational times for each of the radial step size is illustrated in Figure 3.17.

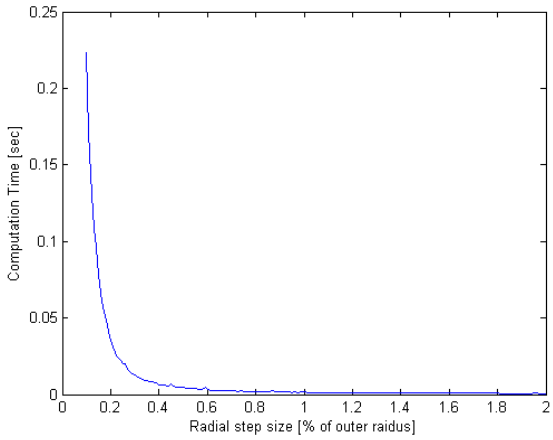

Figure 3.17 - Computational time for the kite-shaped feature with varying radial step sizes

The computational time reaches a lower asymptote at about 0.6% of the outer rotor radius as seen in the wedge feature. The solution times for the kite-shaped feature are lower overall than the wedge feature which is not expected. The kite-shaped feature algorithm must estimate the inner and outer boundaries of the feature whilst the wedge feature algorithm only has to estimate one boundary. The number of estimations the algorithm must perform depends on the size of the feature and the number of circumferential nodes it encompasses. The difference in size between the kite-shaped feature and the wedge feature may be a cause to the solution time discrepancy. Further investigation was conducted to determine the effects the outer angle of the kite-shaped feature have on the area error percentage. The results for angles between 2° and 75° are illustrated in Figure 3.18.

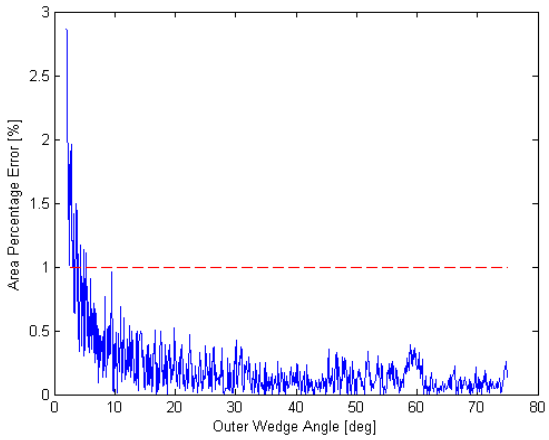

Figure 3.18 - Area percentage error for the kite-shaped feature with varying outer wedge angles

The model produced similar errors for small angles as seen in the wedge feature. This is due to the feature angles approaching the circumferential step size of the mesh.

3.4.3 Rectangular feature

The rectangular feature can be used to model rectangular rotor bars as well as parallel side teeth found in the stator and rotor of many electric machines. The dimensions defining the rectangular geometries are illustrated in Figure 3.19.

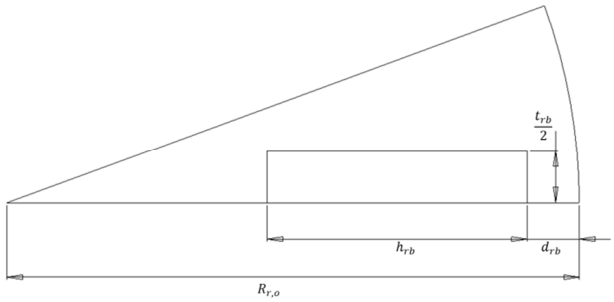

Figure 3.19 - Bounding descriptors for the rectangular geometry

The approximation of the upper side of the rectangular feature is bounded by θ_1 and θ_2 calculated in (3.33)-(3.34).

$$\theta_1 = \tan^{-1}\left(\frac{t_{rb}/2}{R_{rb,o}}\right) \tag{3.33}$$

$$\theta_2 = \tan^{-1}\left(\frac{t_{rb}/2}{R_{rb,i}}\right) \tag{3.34}$$

The radial step value for each circumferential node between θ_1 and θ_2 is calculated in (3.35).

$$R_{step,i} = \frac{R_{rb,i}\tan(\theta_2)}{\sin(\vec{\theta}_{seg,i})} \tag{3.35}$$

The identification of the closest node for the resulting radial step value is performed using a modified version of (3.21) and (3.22). The nodes from $R_{rb,i}$ to r_{seg,I_i} and from 0 to $\theta_{seg,i}$ for each angular step are segmented as part of the rectangular feature. The segmentation of the rectangular geometry is accomplished using the algorithm illustrated in Figure 3.20.

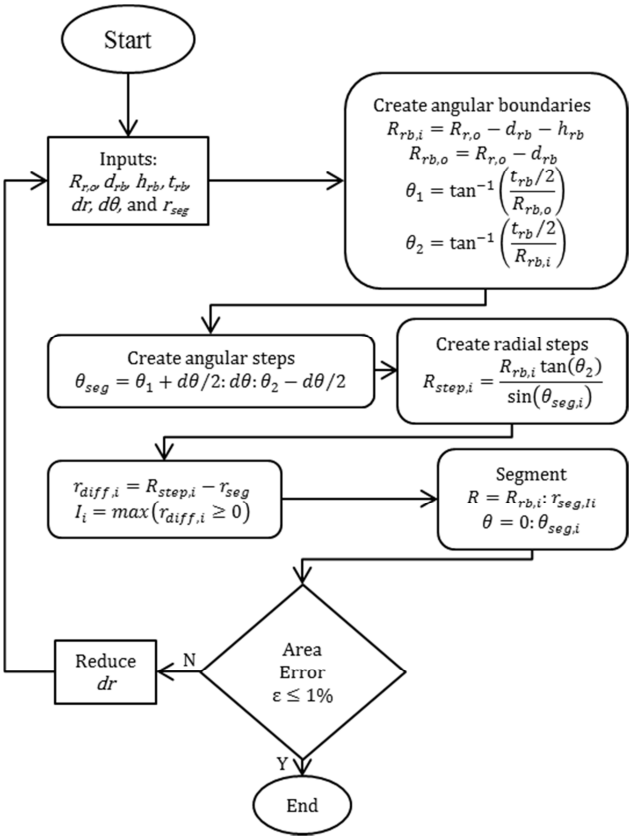

Figure 3.20 - Segmentation algorithm for the rectangular geometry

A result from the segmentation of a rectangular feature is illustrated in Figure 3.21. The dimensions for this particular case are an outer rotor radius of 100 mm, a feature depth of 10 mm, a feature height of 45 mm, and a thickness of 20 mm.

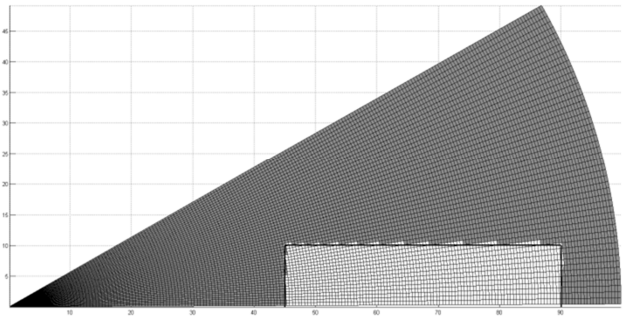

Figure 3.21 - Mesh generation and segmentation results for the rectangular geometry

This case was meshed using a radial step size of 0.5% of the outer rotor radius and produced an area error of 0.0053%. This very low error is on the lower bound of the error for this feature. The error fluctuates significantly with slight variation of the feature dimensions. The area percentage error from the variety of radial step sizes is illustrated in Figure 3.22.

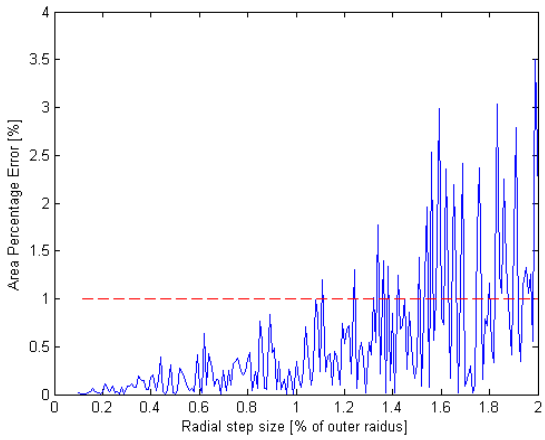

Figure 3.22 - Area percentage error of the rectangular feature with varying radial step sizes

An error of less than 1% was found for radial step sizes less than about 1.8% of the outer rotor radius. The corresponding computational times for each of the radial step size is illustrated in Figure 3.23.

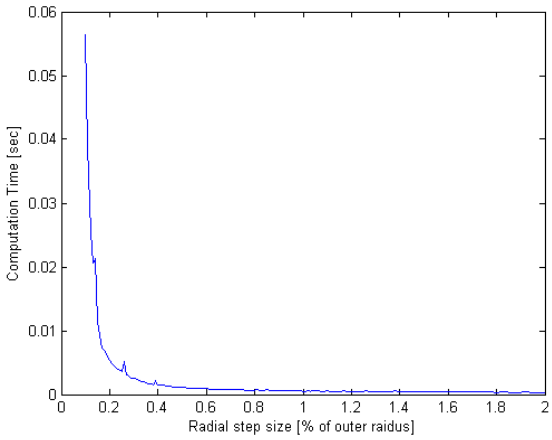

Figure 3.23 - Computational time for the rectangular feature with varying radial step sizes

The computational time reaches a lower asymptote at about 0.6% of the outer rotor radius as seen previously. The solution times and trend for the rectangular feature are similar to those of the wedge and kite-shaped feature. Investigation was conducted to determine the effects the thickness of the rectangular feature have on the area error percentage. The results for thicknesses between 2 and 40 mm are illustrated in Figure 3.24.

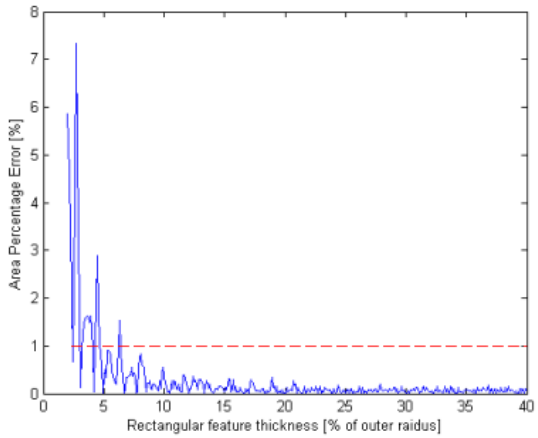

Figure 3.24 - Area percentage error for the rectangular feature with varying feature thicknesses

The model produced high error at small thicknesses. This is due to the similarity between the feature size and the circumferential step size. The segmentation algorithm adjusts the node sizing to better capture these small features but results in longer solution times. Care must be taken when attempting to model these smaller features.

3.4.4 Circular

The circular feature segmentation can be used to model circular rotor bars and fillets. The input dimensions for the circular geometry are illustrated in Figure 3.25.

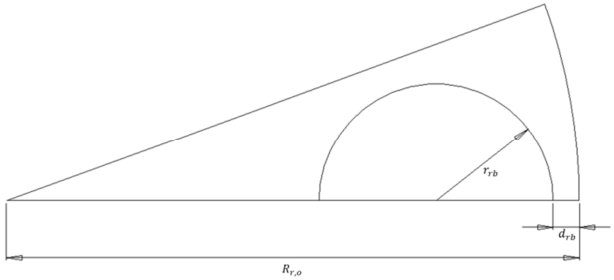

Figure 3.25 - Bounding descriptors for the circular geometry

The segmentation of the circular feature is divided into two separate sections. The bounding upper angle, θ_{1_i}, and the outer boundary for the inner feature, $R_{rb,t}$, are determined using (3.36)-(3.37).

$$\tan(\theta_1) = \frac{r_{rb}\cos\left[\sin^{-1}\left(r_{rb}/R_{rb,m}\right)\right]}{R_{rb,m} - \left(r_{rb}{}^2/R_{rb,m}\right)} \tag{3.36}$$

$$R_{rb,t} = \frac{r_{rb}\sin(\theta_b)}{\sin(\theta_1)} \tag{3.37}$$

The radial step values for the inner and outer sections are calculated using (3.38)-(3.39).

$$R_{step,i} = \frac{r_{rb}\sin\left(\theta_{inner,right,i}\right)}{\sin\left(\theta_{seg,i}\right)} \tag{3.38}$$

$$R_{step,2,i} = \frac{r_{rb}\sin\left(\theta_{outer,right,i}\right)}{\sin\left(\theta_{seg,i}\right)} \tag{3.39}$$

The nodes for the inner section from $r_{seg,I_{lower}}$ to $R_{rb,t}$ and for the outer section from $R_{rb,t}$ to $r_{seg,I_{luppr}}$ for each angular step are segmented as part of the rectangular feature. The algorithm used to segment the circular feature is illustrated in Figure 3.26.

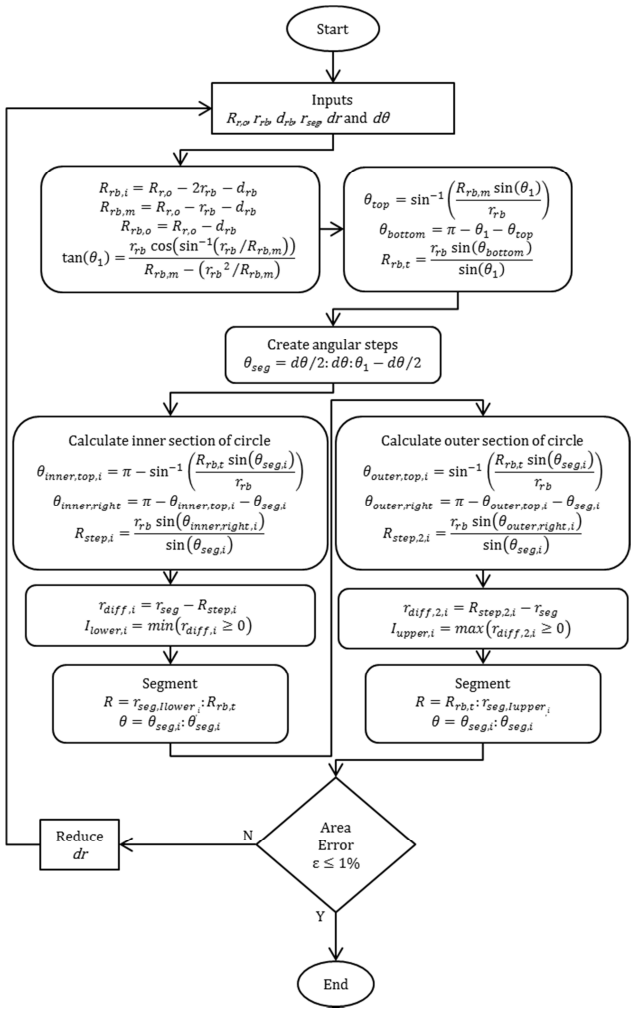

Figure 3.26 - Segmentation algorithm for the circular geometry

A result from the segmentation of a circular feature is illustrated in Figure 3.27. The dimensions for this particular case are an outer rotor radius of 100 mm, a feature center at 75 mm, and a feature radius of 20 mm.

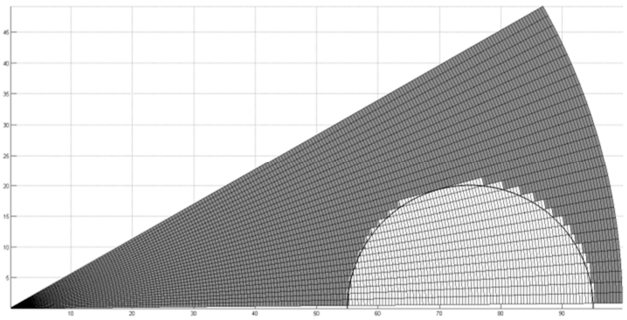

Figure 3.27 - Mesh generation and segmentation results for the circular geometry

This case was meshed using a radial step size of 0.5% of the outer rotor radius and produced an area error of 0.2417%. This error is relatively large compared to the other example case but is still well under the 1% expectation. The error fluctuates with slight variations to the feature dimensions as discussed previously. The area percentage error from the variety of radial step sizes is illustrated in Figure 3.28.

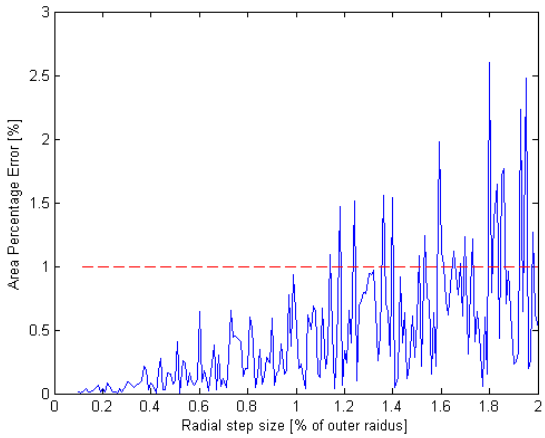

Figure 3.28 - Area percentage error of the circular feature with varying radial step sizes

An error of less than 1% was found for radial step sizes less than 1.8% of the outer rotor radius. The corresponding computational times for each of the radial step size is illustrated in Figure 3.29.

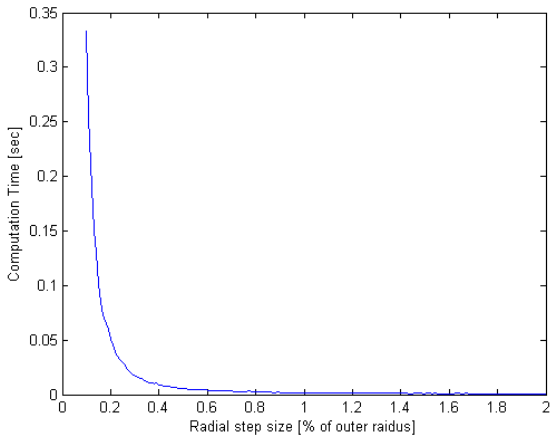

Figure 3.29 - Computational time for the circular feature with varying radial step sizes

The computational time reaches a lower asymptote at about 0.6% of the outer rotor radius as seen previously. Investigation was conducted to determine the effects the radius of the circular feature have on the area error percentage. The results for thicknesses between 1 and 24 mm are illustrated in Figure 3.30.

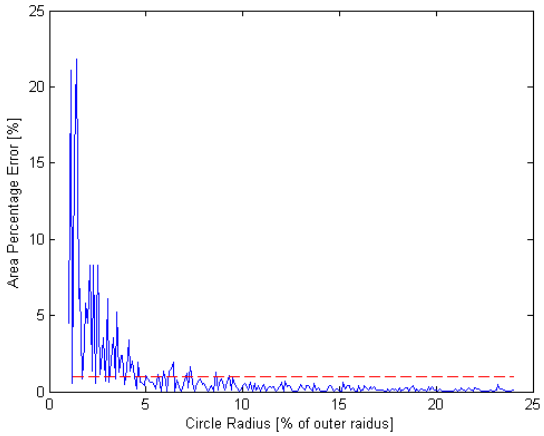

Figure 3.30 - Area percentage error for the circular feature with varying feature radii

The model produced high error at small radii. The circular feature boundary becomes very difficult to estimate with fewer nodes. The error increases as the ratio of feature to node size decreases.

3.5 Switched Reluctance Machine Tooth Geometries

The mesh generation and segmentation algorithms can be used to describe the geometries found with switched reluctance machines. The full SRM is simplified to two dimensions by using the R-θ plane at the axial midpoint of the machine as illustrated in Figure 3.31. The solution space can be further reduced to a half machine area if the numbers of stator and rotor teeth are both even. The algorithms did not include rotor pole shoes, shaft keyways, or fillets.

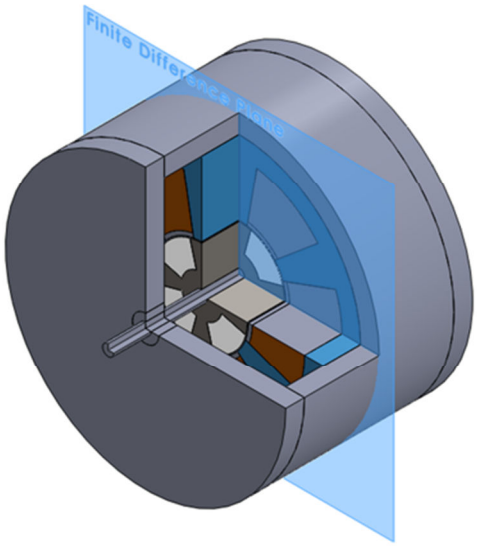

Figure 3.31 - Three dimensional CAD model of a switched reluctance machine displaying the R-θ finite difference solution plane

Three rotor geometries for switched reluctance machines were proposed to capture a majority of the designs in existence: radial tooth, high speed tooth, and parallel tooth. The radial tooth geometry exhibits features that can be described with simple radial lines and circumferential arcs, and therefore is easily meshed in polar coordinates. The radial tooth

rotor with its adiabatic lines of symmetry and resulting half slot is illustrated in Figure 3.32.

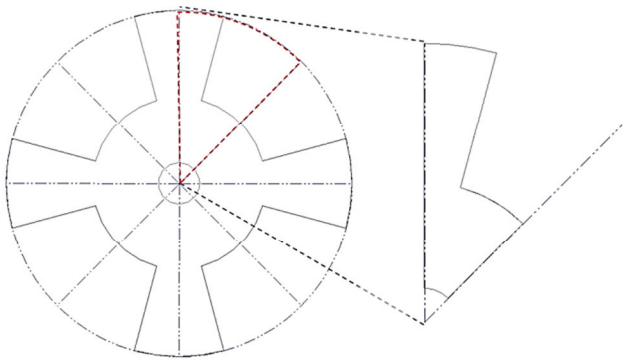

Figure 3.32 - Adiabatic lines of symmetry and resulting half slot geometry for a radial tooth SRM rotor

In the case of the radial tooth geometry, three radial and two circumferential segments were created: rotor back iron, rotor tooth and rotor cavity of air or a potting material. The angles describing the rotor and stator half slot geometries are identified using mesh and segmentation algorithms. The angles pertaining to the adjacent half slots are defined using (3.40)-(3.41).

$$\theta_i : 2\theta_{hs} : \theta_s \tag{3.40}$$

$$2\theta_{hs} - \theta_i : 2\theta_{hs} : \theta_s \tag{3.41}$$

The original angular descriptor, θ_i, is shifted to be twice the angular span of the half slot, θ_{hs}, to describe the adjacent tooth geometry. This is repeated for the entire span of the solution space, θ_s. The mirrored side of the tooth geometry is set by twice the angular span of the half slot minus the original angular descriptor. The resulting mesh generation and segmentation of the described rotor, along with common stator geometry, is displayed in Figure 3.33.

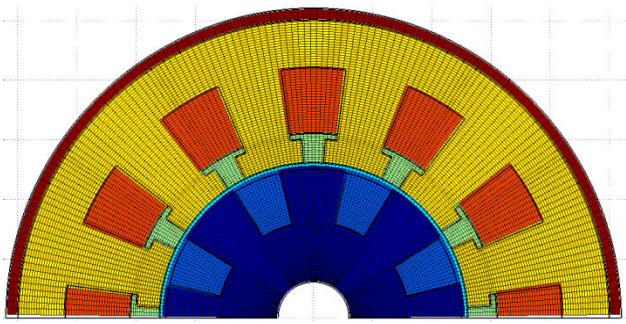

Figure 3.33 - Mesh generation and segmentation result for a radial tooth SRM half machine

The high speed rotor geometry is similar to the radial tooth geometry but features a tooth that varies the air gap dimension over its span. The adiabatic lines of symmetry and resulting full pitch slot for this geometry is illustrated in Figure 3.34.

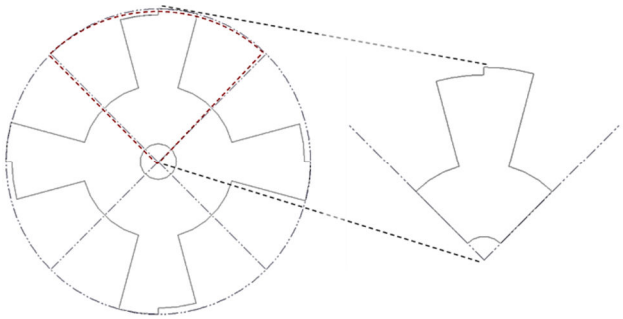

Figure 3.34 - Adiabatic lines of symmetry and resulting half slot geometry for a high speed tooth SRM rotor

The segmentation for the high speed tooth is similar to that of the radial tooth but divides the tooth segment to capture the radial step at the tooth tip. The mesh generation and segmentation for the high speed rotor and stator are displayed in Figure 3.35.

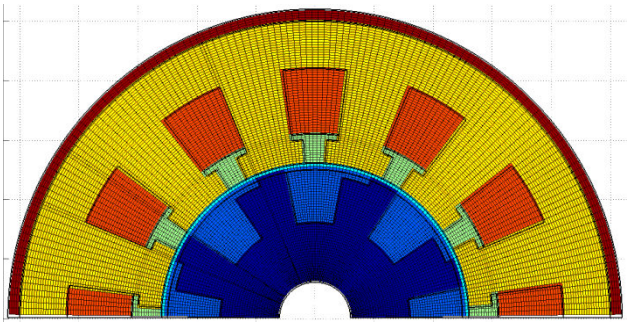

Figure 3.35 - Mesh generation and segmentation result for a high speed tooth SRM half machine

The parallel tooth geometry presents a new challenge as the parallel sides cannot be defined with a simple radial line. This geometry still exhibit adiabatic lines of symmetry and can be simplified to a half slot as is illustrated in Figure 3.36.

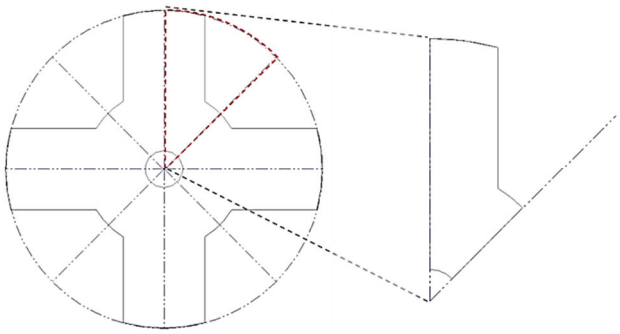

Figure 3.36 - Adiabatic lines of symmetry and resulting half slot geometry for a parallel tooth SRM rotor

The stair step approach described previously to model rectangular features is used to approximate the straight edge of the rotor tooth. The mesh generation and segmentation for the parallel tooth rotor and stator is displayed in Figure 3.37. As the number of nodes in the mesh increase, the tooth approaches a smooth horizontal edge.

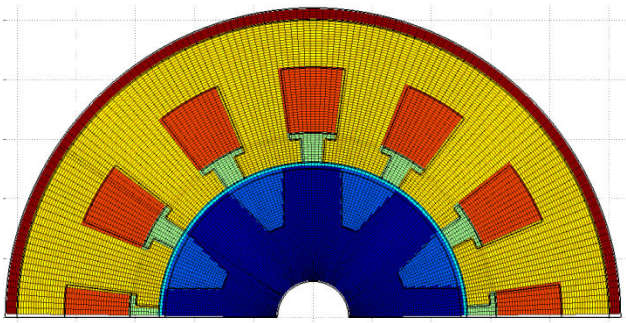

Figure 3.37 - Mesh generation and segmentation result for a parallel tooth SRM half machine

3.6 Induction Machine Rotor Bar Geometries

Although the rotor of an induction machine is different than that of a PM or SRM, the stator design remains very similar. The mesh generation and segmentation for the IM uses a similar R-θ finite difference solution plane as the SRM model as illustrated in Figure 3.38.

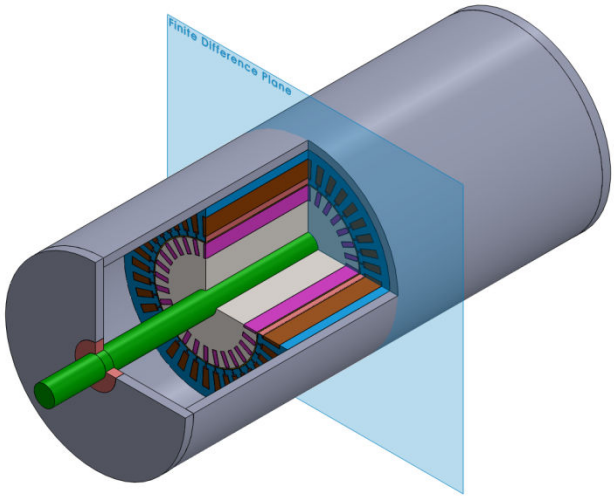

Figure 3.38 - Three dimensional CAD model of an induction machine displaying the R-θ finite difference solution plane

Much research has been performed to optimize the shape, size and number of rotor bars in induction machines. During the startup phase of a machine, the rotor can see very high induced current. During this initial phase, the slip starts at 100% and eventual goes

to the rated slip depending on load. The shape of the rotor bar is optimized to deal with edge effects during start up and uniform current densities found during steady state operation.

3.6.1 Common induction machine rotor bar geometries

The geometric feature algorithms are used to model the common induction rotor bar geometries identified by Harley in Figure 3.1 [53]. The stator mesh generation and segmentation is adapted from the previous work of Semidey [5]. This work advances the mesh and segmentation to include the rotor and its features. The defining descriptors for each of the rotor bar geometries are illustrated in Figure 3.39.

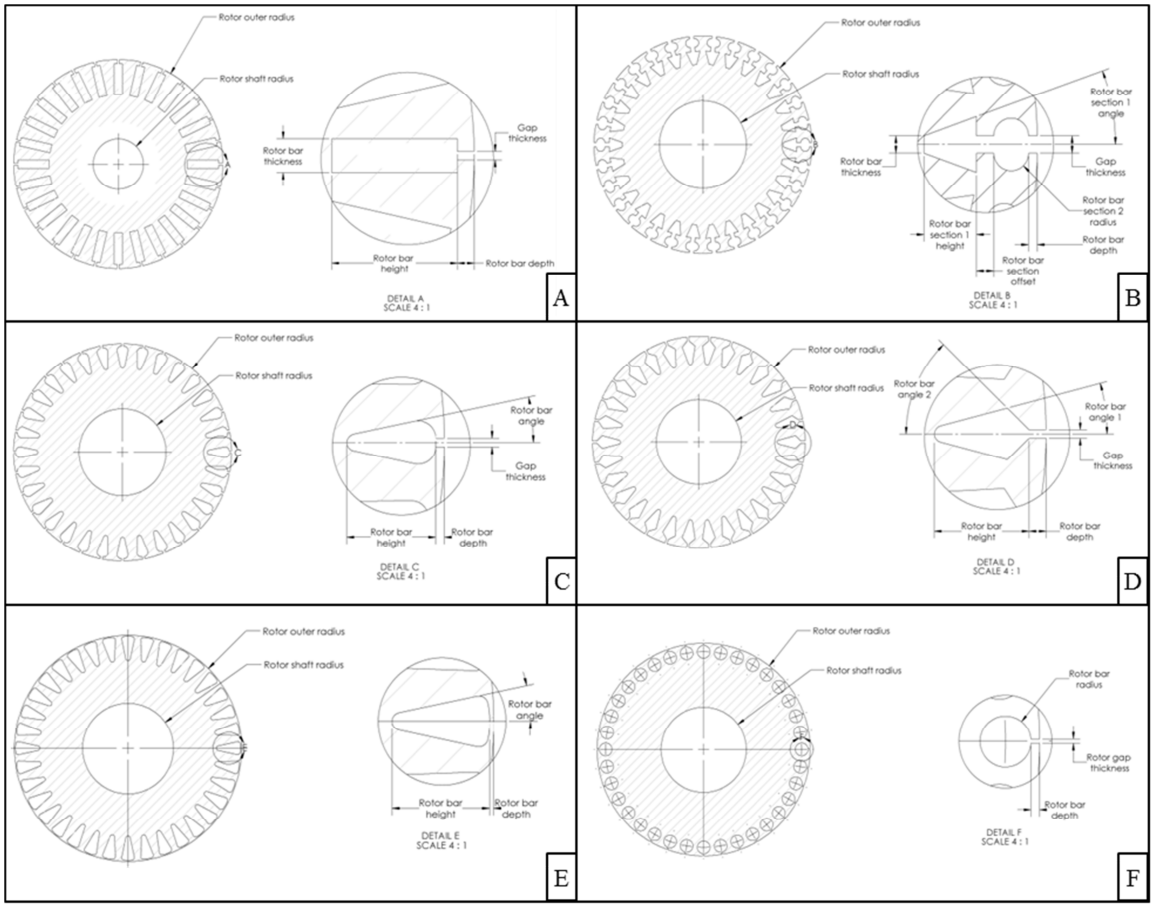

Figure 3.39 - Rotor bar geometries with feature descriptors

The geometry of rotor bar A is approximated using the rectangular feature described earlier. It has a similar approach to the parallel sided tooth of the SRM described previously. The results from the mesh generation and segmentation for an IM with rotor bar A geometry are illustrated in Figure 3.40.

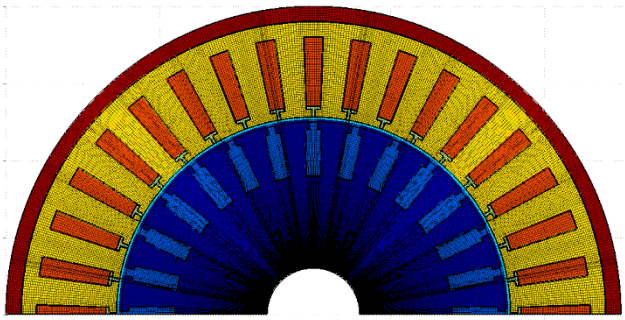

Figure 3.40 - Mesh generation and segmentation result for an IM half machine with rotor bar A

Rotor bar B has the most complicated geometry to model. The circular feature at the outer radius is incorporated to help with edge effects during startup and acceleration of the machine. The lower section of the rotor, with an off angle feature, is designed for steady state operation when the current density is uniform. The resulting mesh generation and segmentation for this rotor geometry is illustrated in Figure 3.41.

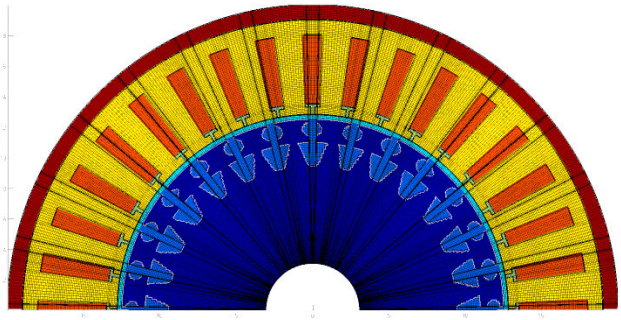

Figure 3.41 - Mesh generation and segmentation result for an IM half machine with rotor bar B

The rotor bar with geometry C uses the wedge and circular algorithms discussed previously. The depth of the rotor bar is exaggerated to show the segmentation of the gap between adjacent rotor teeth. The result from the mesh generation and segmentation is illustrated in Figure 3.42.

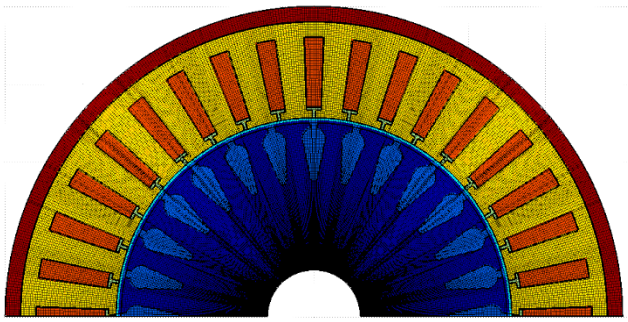

Figure 3.42 - Mesh generation and segmentation result for an IM half machine with rotor bar C

The mesh generation and segmentation result for rotor bar D is illustrated in Figure 3.43. This geometry use the kite-shaped modeling approach discussed previously.

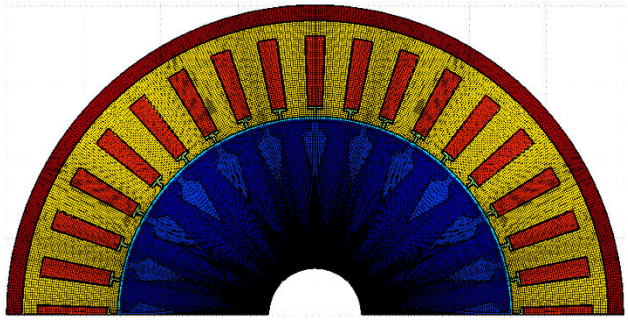

Figure 3.43 - Mesh generation and segmentation result for an IM half machine with rotor bar D

The mesh generation and segmentation for rotor bar E, illustrated in Figure 3.44, is very similar to that of rotor bar C. The only difference is the absence of the gap between adjacent rotor teeth. The rotor bar is total encompassed by the back iron of the rotor.

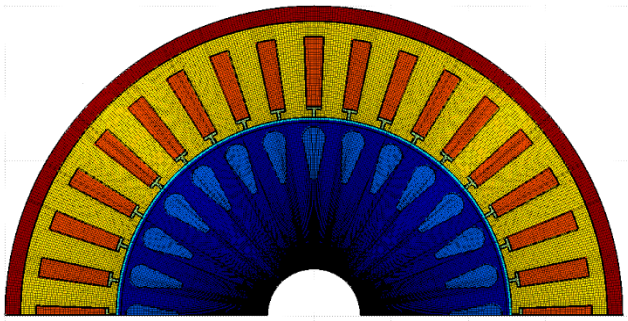

Figure 3.44 - Mesh generation and segmentation result for an IM half machine with rotor bar E

The final geometry, rotor bar F, uses the circular mesh generation and segmentation algorithm and the result is illustrated in Figure 3.45.

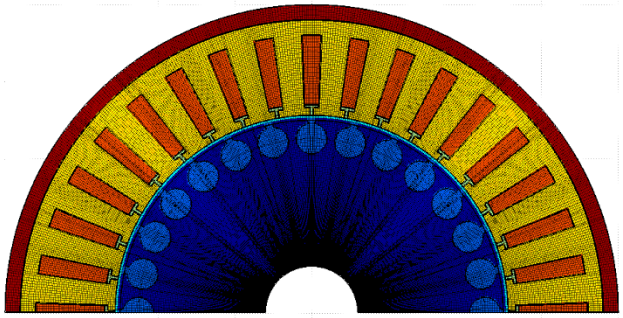

Figure 3.45 -Mesh generation and segmentation result for an IM half machine with rotor bar F

The discussed rotor bar geometries are just a few of the common geometries identified by Harley. As seen with rotor bar B, complex geometries can be modeled by using a combination of different segmentation algorithm described in the previous section.

3.7 Discussion

The work results in segmentation of common geometries found in electric machines. The single or combined use of the segmentation algorithms was shown to capture all the example rotor geometries. The segmentation of the features results in boundaries with

stair-stepping effects. The stair-step effect had little effect on area error of the features. The effects of these stair-steps on the temperature distribution will be further examined in the following chapters. The stair-stepping effect and thus the area percentage error can be reduced by using a smaller radial step size; however, this results in longer solution times. An acceptable area error of 1% was chosen and will be verified using the thermal models in the following chapters. A starting radial step size of 0.5% of the air gap radius was suggested to maintain a balance between model accuracy and computational speed. Some features such as small angle, small thicknesses, and small radius values, may need reduced radial step sizes to accurately capture cross sectional area of the feature. This modification is captured by an error check at the end of each segmentation algorithm.

3.8 Summary

Initial results demonstrate that non-polar geometries can be modeled in polar coordinates with small percentage error in area. The model is able to suggest the appropriate radial step size of 0.5% of the air gap radius for the nodal mesh elements. This step size balances area accuracy to with 1% whilst maintaining computational speed. The results for area error in each of the features show a trend of decreasing error as the size of the node decreases. The decrease in node size comes at a cost of computational time. A balance between area error and computational time was found and provides a starting node size for the meshing and segmentation algorithms. The nodes size can be adjusted if the resulting error is over the acceptable limit of 1%. Small angles and small feature sizes require smaller node sizing due to the feature size approaching the circumferential step size of the node. Very complex rotor bar geometries were shown to be modeled using a combination of the different features.

CHAPTER 4

SWITCHED RELUCTANCE THERMAL MODEL

4.1 Introduction

This chapter focuses on the creation of thermal model used for the estimation of the temperature distribution within ideal switched reluctance machine design candidates. The thermal estimation model will help search for optimal machine candidates while reducing the need for tabulated values and heuristics. The estimation is performed using a hybrid finite difference and thermal circuit approach. The proposed combination of these approaches results in a temperature estimation model for machine sizing purposes that sacrifices model complexity for computational speed. Finite difference was chosen as an ideal approach due to its relative accuracy and lower computational power requirement when compared to FEA. The thermal module predicts temperature gradients and hot spot locations that can lead to winding insulation failure, magnetic property degradation, and thermo-mechanical stresses. Prolonged exposure to high temperatures can degrade the insulation coating on the winding wires and can eventually lead to a catastrophic short circuit.

The finite difference solution space is defined as half of the R-θ section plane at the axial midpoint of the machine. This simplification for full 3D machine to R-θ plane to half machine plane is illustrated in Figure 4.1. Convection in the air gap captures the thermal transport between the rotor and stator. Separate frame and shaft thermal transport models using thermal circuits define the boundary conditions of the finite difference. The hybrid thermal estimator must accurately capture the temperature distribution within

switched reluctance machines to within half of the range between winding insulation classes while maintaining computational speed.

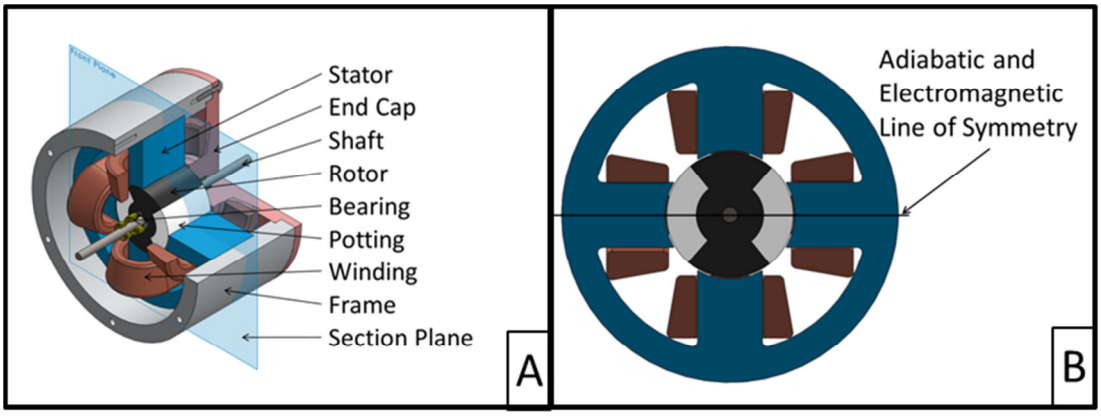

Figure 4.1 - Finite difference solution space simplification from a full three dimensional machine (A) to R-θ plane at the axial midpoint of the machine (B)

4.2 Finite Difference Approach

The finite difference approach uses a step by step algorithm to solve the temperature of each node by understanding the thermal resistance between neighboring nodes, the heat generation within the nodal control volume and boundary conditions. The temperature of each node is solved at a discrete point in the center of the node. A mesh with center node distribution is illustrated in Figure 4.2.

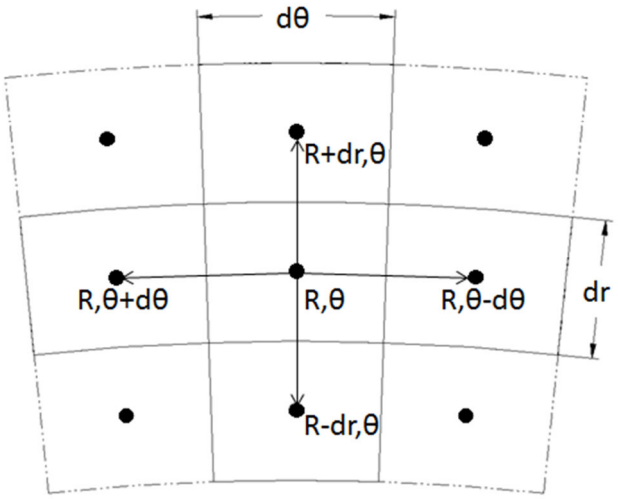

Figure 4.2 - Nodal network with center node distribution

For the steady state condition, each node must satisfy the energy balance defined in (4.1).

$$\sum \dot{E}_{in} + \sum \dot{E}_{generated} = 0 \tag{4.1}$$

The energy into the node is defined as the temperature difference divided by the thermal resistance between the adjacent node and the solution node. The energy generated in the control volume of the node is the internal heat generation, $\dot{q}_{R,\theta}$, multiplied by the volume of the node, $V_{R,\theta}$. The expanded energy balance equation is illustrated in (4.2).

$$\frac{T_{R,\theta+d\theta} - T_{R,\theta}}{R_{tot|R,\theta+d\theta}} + \frac{T_{R,\theta-d\theta} - T_{R,\theta}}{R_{tot|R,\theta-d\theta}} + \frac{T_{R+dr,\theta} - T_{R,\theta}}{R_{tot|R+dr,\theta}} + \frac{T_{R-dr,\theta} - T_{R,\theta}}{R_{tot|R-dr,\theta}} = -\dot{q}_{R,\theta} V_{R,\theta} \tag{4.2}$$

The total thermal resistance values between the adjacent internal nodes and the solution node are described in (4.3)-(4.5).

$$R_{tot|R,\theta\pm d\theta} = \frac{R \cdot d\theta}{k \cdot dr} \tag{4.3}$$

$$R_{tot|R+dr,\theta} = \frac{\ln(\frac{R+dr}{R})}{k \cdot d\theta \cdot \left(R + \frac{dr}{2}\right)} \tag{4.4}$$

$$R_{tot|R-dr,\theta} = \frac{\ln(\frac{R}{R-dr})}{k \cdot d\theta \cdot \left(R - \frac{dr}{2}\right)} \tag{4.5}$$

For nodes to the left or right of the solution node, the conduction length is described as arc length at the node radius with a circumferential step size span. The cross sectional area is described as the product of the radial step size and a unit length in the axial direction. For nodes above and below the solution node, the conduction length is described as the natural log of the outer radius divided by the inner radius. The cross sectional area is the arc length at the radius between the two nodes with a circumferential step size span. These resistance values assume the step sizes and thermal conductivity for adjacent nodes are similar. Adjacent nodes with dissimilar step sizes or thermal conductivities must be divided into two separate resistance values summed in series. The resistance values for the boundary nodes and the nodes within the air gap are more complicated and are discussed in detail in later sections.

The finite difference solution algorithm illustrated in Figure 4.3 is an overview of the model. The mesh generation and segmentation algorithms discussed in the previous chapter are used to differentiate the components of the SRM. The mesh is generated using the user defined geometric input parameters. The frame, stator iron, windings, air under the windings, air gap, rotor iron and rotor potting material are parametric defined and segmented. The error of the segmented area is checked and if it is not within 1% of

the actual area, the mesh generation and segmentation is redone with a smaller radial step size. The material properties, such as thermal conductivity, are assigned to their corresponded segments. The internal heat generation values due to copper and core losses, described in detail later, are assigned to the windings and stator and rotor iron respectively. The heat generated within the finite difference solution plane is dissipated through three dimensional heat paths through the shaft and frame. The three dimensional effects of the shaft and frame are accounted for using a thermal circuits approach discussed later. The thermal resistances are assigned as boundary conditions in the model. The calculations of the boundary conditions in the thermal networks require initial guess temperatures for material properties of the surrounding air. The coefficients for the unknown nodal temperatures are used to create a tri-diagonal matrix, *K*. The matrix has five diagonal values corresponding to the node and neighboring nodes coefficients. The constant temperature boundary and heat generation values are captured in the constant vector, *C*. The temperature for each node is solved using the direct matrix inversion method. The guess temperatures for the boundary conditions are compared to the solution temperatures. The guess temperatures are modified until the absolute value of the difference between the guess temperature and the solution temperature is 1 °C.

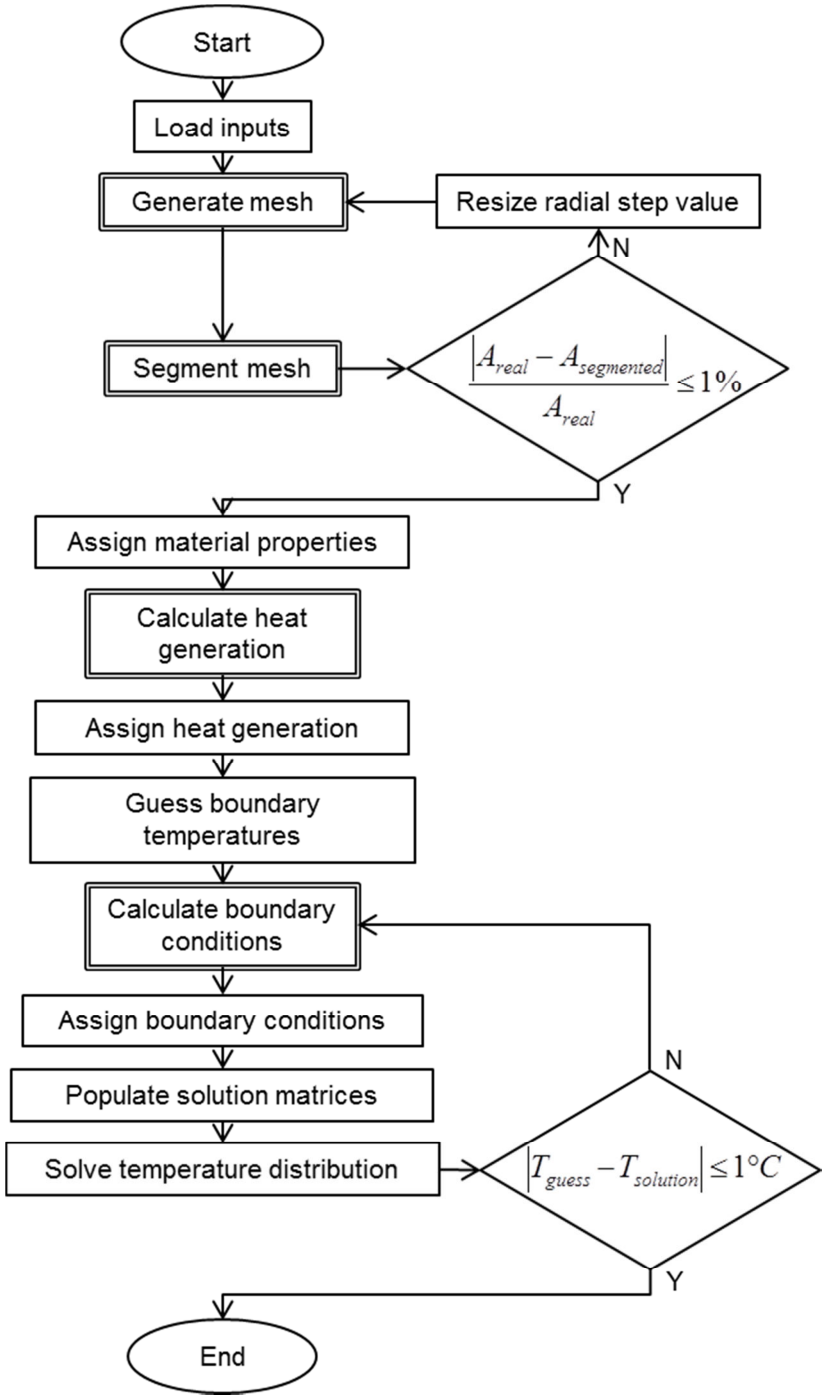

Figure 4.3 - Finite difference solution algorithm

4.3 Loss Calculations

The thermal model for the switched reluctance machine includes three sources of internal heat generation: stator copper loss, stator core loss and rotor core loss. The

windings produce a significant amount of heat due to ohmic losses. The calculation algorithm of the internal heat generation to be implemented into the model is illustrated in Figure 4.4.

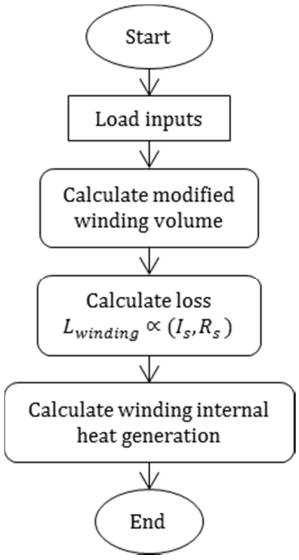

Figure 4.4 - Stator copper loss calculation algorithm

The modified volume of the windings, V_w, is calculated using the cross sectional area, A_w, the axial length of the stator, L_{axial}, and a factor to account for the end windings, f_{end}. The copper loss, $L_{winding}$, is defined using the current per phase, I_s, the resistance per phase, R_s, and the number of phases. The internal heat generation, $\dot{q}_{winding}$, is calculated from the resulting copper loss and winding volume.

The stator and rotor iron also produce heat due to core losses such as hysteresis and eddy currents. The eddy current losses are mitigated by using thin electric steel laminations. The hysteresis loss is a function of electrical frequency, f, and magnetic flux density, B. The calculation algorithm of the internal heat generation due to core loss is illustrated in Figure 4.5.

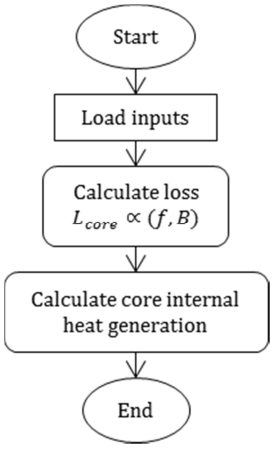

Figure 4.5 - Core loss calculation algorithm

The core loss, L_{core}, is determined using data from the electric steel manufacturer such as the chart illustrated in Figure 4.6 or from electromagnetic simulation.

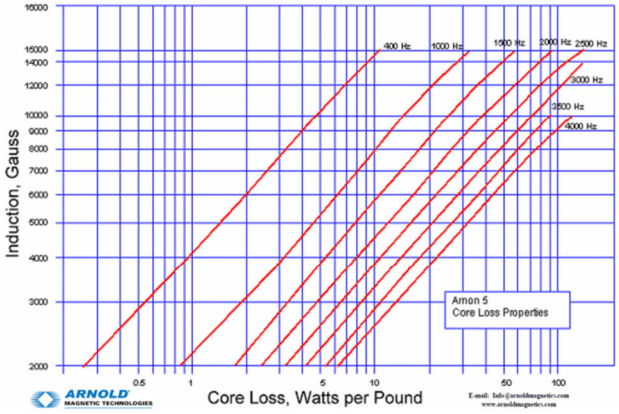

Figure 4.6 - Core loss data for Arnold Arnon 5 electric steel

Mechanical losses due to friction and windage inside the machine are assumed to be negligible. Internal heat generation in the bearings is also assumed to be small and not modeled in this estimator. This assumption is likely to break down at high load and high speed operating conditions. This additional heat source would affect the frame and shaft thermal transport model applied as boundary conditions to the finite difference model.

4.4 Frame Thermal Transport Model

Whilst the finite difference model solution encompasses the thermal distribution in the R-θ plane, heat transfer in the axial direction must be captured using a different approach. Thermal circuit analysis was chosen as ideal approach due to its computational efficiency and ability to accurately capture heat transfer paths with relatively linear temperature gradients. The thermal resistance for the frame boundary, which includes convection on the surface of the frame and end caps, was adapted from the work of Semidey and Mayor [5]. The amount of heat able to be rejected depends on the difference of the surface and ambient temperature and the thermal resistance, $R_{convection}$, described in (4.6).

$$R_{convection} = \frac{1}{h \cdot A} \tag{4.6}$$

Fins are commonly implemented into the design to increase the convection surface area, A. Internal or external fan can be used to create forced convection which result in higher convection coefficients, h. The work of Semidey and Mayor includes a variety of boundaries conditions: smooth natural horizontal, smooth natural vertical, smooth forced, finned natural horizontal, finned natural vertical, and finned forced. The work provides Nusselt correlations for these different conditions. An addition boundary condition for annular fins was used to describe the heat transfer from the frame of the experimental machine. Jones and Nwizu developed the Nusselt correlation used to describe the annular fin heat transfer as described in (4.7) [54].

$$Nu_{af} = 0.116\left(Ra\right)^{0.53}\left[1-\exp\left(\frac{-155}{Ra}\right)\right]^{0.26} \tag{4.7}$$

$$Ra = \frac{g \cdot \beta \cdot \Delta T \cdot b^4}{\nu \cdot \alpha \cdot D} \tag{4.8}$$

The Rayleigh number, Ra, is calculated using gravitational acceleration, g, the volumetric coefficient of thermal expansion, β, the temperature difference between the surface and ambient temperature, ΔT, the spacing between fins, b, the kinematic viscosity of the ambient air, ν, the thermal diffusivity of air, α, and the outer fin diameter, D.The thermal circuit consists of three separate thermal resistances. Radial conduction from the center of the outermost nodes to the outer radius of the frame is the first resistance. The convection heat transfer from the frame and from the end caps are modeled with a parallel circuit. The frame convection uses (4.6) whilst the end caps are treated as an effective fin. The fin efficiency, η_f, and overall surface efficiency, η_o, for the annular fins are described in (4.9)-(4.15) where I_i and K_i are modified i^{th} order Bessel functions of the first and second order respectively [55].

$$\eta_f = C_2 \frac{K_1(m \cdot R_{fr}) I_1(m \cdot r_{2c}) - I_1(m \cdot R_{fr}) K_1(m \cdot r_{2c})}{I_0(m \cdot R_{fr}) K_1(m \cdot r_{2c}) - K_0(m \cdot R_{fr}) I_1(m \cdot r_{2c})} \tag{4.9}$$

$$C_2 = \frac{(2R_{fr}/m)}{(r_{2c}^2 - R_{fr}^2)} \tag{4.10}$$

$$m = \sqrt{2h_{af} / k_{af} t_{af}} \tag{4.11}$$

$$A_{f,af} = 2\pi \cdot (r_{2c}^2 - R_{fr}^2) \tag{4.12}$$

$$r_{2c} = R_{fr} + (t_{af} / 2) \tag{4.13}$$

$$A_t = NA_f + A_b \tag{4.14}$$

$$\eta_o = 1 - \frac{NA_f}{A_t}(1 - \eta_f) \tag{4.15}$$

The work treats the inner radius boundary of the stator as adiabatic or assigns it a local heat transfer coefficient and ambient temperature. This inner boundary condition changes with the addition of the rotor in the finite difference model.

4.5 Shaft Thermal Transport Model

The three dimensional heat paths from the innermost nodes of the finite difference to ambient are modeled by series of thermal resistances. The thermal resistance for the shaft is distributed between two parallel paths: heat transfer through the shaft extension and convection on the surface of the end caps. A diagram of the thermal resistances applied to each boundary node is illustrated in Figure 4.7.

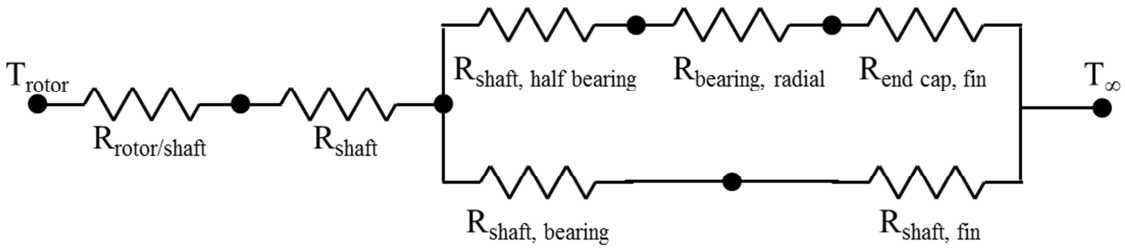

Figure 4.7 - Thermal circuit representation for the shaft thermal transport

The thermal circuit consists of three general types of resistances: cylindrical radial conduction, axial conduction, and heat transfer from extended surfaces. The radial conduction resistance $R_{cond,rad}$ for a hollow cylinder is given by (4.16).

$$R_{cond,rad} = \frac{\ln(r_2 / r_1)}{2\pi kL} \tag{4.16}$$

The outer and inner radii, r_2 and r_1 respectively, the thermal conductivity of the material, k, and the axial length, L, are the dimension and properties for this equation. This resistance value is used to describe the conduction path of the boundary node in the finite difference model to the interface with the shaft. It is also used to describe the radial conduction through the bearings. Axial conduction resistance, $R_{cond,axial}$, is described in (4.17).

$$R_{cond,axial} = \frac{L}{kA} \tag{4.17}$$

The cross section area, A, is described as the area normal to the heat flux. This equation is used to describe the axial heat transfer in the shaft. The thermal resistance value for an extended surface, R_{fin}, is defined by (4.18). The shaft extension and the end cap are modeled as fins and are discussed later.

$$R_{fin} = \frac{1}{h \cdot A_f \cdot \eta_f} \tag{4.18}$$

In (4.18), h is the convection coefficient, A_f is the fin area, and η_f is the fin efficiency. These three equations describe the general form of the resistance.

The resistance values used in the model differs slightly from the general forms. The resistance value applied to each of the shaft boundary nodes varies slightly due to different circumferential step values. This results in a modified radial conduction resistance for the rotor/shaft interface, $R_{rotor/shaft}$, illustrated in (4.19).

$$R_{rotor/shaft} = \frac{\ln\left(\frac{R_{shaft} + \frac{dr_1}{2}}{R_{shaft}}\right)}{k_{rotor} \cdot d\theta_i} \tag{4.19}$$

In (4.19), dr_1 is the radial step size of the innermost nodes and $d\theta_i$ is the circumferential step size for each node. The axial resistance, R_{shaft}, is used to describe the shaft thermal transport from the mid-plane of the machine to the bearing/shaft interface. The shaft was considered to have an adiabatic boundary condition while inside the frame, thus discounting any heat transfer through convection to the end well air.

$$R_{shaft} = \frac{\left(L_{frame}/2\right) - \left(L_{axial}/4\right)}{k_{shaft} \cdot {R_{shaft}}^2 \cdot \frac{d\theta_i}{2}} \tag{4.20}$$

In (4.20), the conduction length is modified to better capture its true resistance value. The conduction length is given as the average distance between the machine mid-plane and edge of the rotor. The thermal circuit now splits into two parallel paths to ambient. One path goes through the shaft to the axial midpoint of the bearing, radially through the

bearing, and then to the end cap treated as a fin. The conduction resistance in the shaft for an axial length of half of the bearing width is given by (4.21).

$$R_{shaft,half\ bearing} = \frac{L_{bearing}/2}{k_{shaft} \cdot R_{shaft}^{\ 2} \cdot \frac{d\theta_i}{2}} \tag{4.21}$$

The radial conduction resistance, described in (4.22), uses an effective bearing thermal conductivity. The conductivity value was estimated using the results from experimental resistance values collected by Nakajima [52].

$$R_{bearing,radial} = \frac{\ln(\frac{R_{bearing}}{R_{shaft}})}{k_{bearing} \cdot d\theta_i} \tag{4.22}$$

The resistance for the end cap was calculated by treating it as an annular fin. The convection from inner surface of the end cap to the end well air was assumed to be negligible. This adiabatic assumption is similar to the one used for the shaft and end well heat transfer.

$$R_{end\ cap,fin} = \frac{1}{h_{end\ cap} \cdot \left(A_{f,end\ cap}/2\right) \cdot \eta_{f,end\ cap} \cdot \frac{d\theta_i}{2\pi}} \tag{4.23}$$

The surface area of the end cap, $A_{f,end\ cap}$, is calculated using (4.24)- (4.25) where $R_{bearing}$ is the outer radius of the bearing, $R_{end\ cap}$ is the outer radius of the end cap and $t_{end\ cap}$ is the thickness of the end cap. Only half of the surface area was used to calculate the resistance due to one side being treated as adiabatic.

$$A_{f,end\ cap} = 2\pi \cdot \left({r_{2c}}^2 - {R_{bearing}}^2 \right) \tag{4.24}$$

$$r_{2c} = R_{end\ cap} + \left(t_{end\ cap} / 2 \right) \tag{4.25}$$

The fin efficiency of the end cap fin is calculated using (4.26)- (4.28) where I_i and K_i are modified i^{th} order Bessel functions of the first and second order respectively.

$$\eta_{f,end\ cap} = C_2 \frac{K_1\left(m \cdot R_{bearing}\right) I_1\left(m \cdot r_{2c}\right) - I_1\left(m \cdot R_{bearing}\right) K_1\left(m \cdot r_{2c}\right)}{I_0\left(m \cdot R_{bearing}\right) K_1\left(m \cdot r_{2c}\right) - K_0\left(m \cdot R_{bearing}\right) I_1\left(m \cdot r_{2c}\right)} \tag{4.26}$$

$$C_2 = \frac{\left(2R_{bearing}/m\right)}{\left({r_{2c}}^2 - {R_{bearing}}^2\right)} \tag{4.27}$$

$$m = \sqrt{2h_{end\ cap} / k_{end\ cap} t_{end\ cap}} \tag{4.28}$$

The second parallel path for thermal transport continues in the shaft though the length of the bear to a shaft extension treated as a pin fin. The conduction through the shaft for the axial length of the bearing is calculated using (4.29).

$$R_{shaft,bearing} = \frac{L_{bearing}}{k_{shaft} \cdot {R_{shaft}}^2 \cdot \frac{d\theta_i}{2}} \tag{4.29}$$

The shaft extension past the end caps is used to transmit mechanical power out of the machine or used as a mounting location for an encoder or fan. The thermal resistance, $R_{shaft,fin}$, associated with the shaft extension is described in (4.30).

$$R_{shaft,fin} = \frac{1}{h_{shaft} \cdot A_{f,shaft} \cdot \eta_{f,shaft} \cdot \frac{d\theta_i}{2\pi}} \tag{4.30}$$

The surface area of the fin, $A_{f,shaft}$, and fin efficiency for the shaft extension, $\eta_{f,shaft}$, are defined in (4.31)- (4.34) where P is the perimeter of the fin and A_c is its cross sectional area.

$$A_{f,shaft} = \pi \cdot D_{shaft} \cdot L_c \tag{4.31}$$

$$L_c = L_{extentsion} + \left(D_{shaft} / 4\right) \tag{4.32}$$

$$\eta_{f,shaft} = \frac{\tanh\left(mL_c\right)}{mL_c} \tag{4.33}$$

$$m = \sqrt{h_{shaft} P / k_{shaft} A_c} \tag{4.34}$$

The convection coefficient for the shaft extension, h_{shaft}, is found using the Nusselt number correlation for rotating cylinders from Kendoush [36].

$$h_{shaft} = \frac{Nu_{shaft} \cdot k_{shaft}}{D_{shaft}} \tag{4.35}$$

$$Nu_{shaft} = 0.6366\left(\mathrm{Re}\,\mathrm{Pr}\right)^{0.5} \tag{4.36}$$

$$\mathrm{Re} = \frac{U \cdot D_{shaft}}{\nu} \tag{4.37}$$

In (4.36), Re is the dimensionless Reynolds number and Pr is the Prandtl number for air. The Reynolds number is defined using the surface speed of the shaft, U, the shaft diameter and the kinematic viscosity of the ambient air, ν.

The heat transfer on the surface of the end caps was calculated using the correlation for natural convection over a vertical flat plate. The Nusselt correlation for natural convection on the surface of a vertical plate is described in (3.38)-(3.40).

$$Nu_{ec} = 0.68 + \frac{0.670 \cdot Ra_L^{1/4}}{\left[1 + \left(0.492/\Pr\right)^{9/16}\right]^{4/9}} \tag{4.38}$$

$$Ra_L = \frac{g \cdot \beta \cdot \Delta T \cdot L^3}{\nu \cdot \alpha} \tag{4.39}$$

$$L = R_{ec}\sqrt{\pi} \tag{4.40}$$

The total shaft thermal transport resistance to be applied to the innermost nodes of the finite difference is calculated using (4.41).

$$R_{shaft,tot} = R_{rotor/shaft} + R_{shaft} + \left[\left(\frac{1}{R_{shaft,half\,bearing} + R_{bearing radial} + R_{end cap,fin}}\right) + \left(\frac{1}{R_{shaft,bearing} + R_{shaft,fin}}\right)\right]^{-1} \tag{4.41}$$

4.5.1 Shaft Thermal Transport Validation

The validation of replacing the three dimensional shaft heat transfer with a thermal circuit network was conducting by comparing the finite difference results to finite element analysis results. Internal heat generation was applied the rotor back iron of a radial tooth switched reluctance rotor. The outer radius of the rotor was considered adiabatic; therefore all the heat left through the shaft. The properties used for the simulated cases are displayed in Table 4.1.

Table 4.1 - Properties used for the shaft thermal transport validation study

Property	Value	Unit
L_{active}	100	mm
L_{frame}	200	mm
$t_{end\ cap}$	10	mm
$L_{shaft\ extension}$	25	mm
D_{shaft}	30	mm
$D_{end\ cap}$	200	mm
$D_{bearing}$	50	mm
D_{rotor}	100	mm
k_{iron}	28	W/m K
$k_{potting}$	1	W/m K
k_{shaft}	60.5	W/m K
$k_{end\ cap}$	177	W/m K
$k_{bearing}$	0.24	W/m K

Table 4.2 shows the internal heat generation for each case. For this machine, the switching frequency of 400 Hz relates to a mechanical speed of 8,000 rpm. Common electric steels can achieve peak flux densities of around 2 T before saturation. The flux densities chosen for the test case are based on expected average flux density for the entire rotor volume.

Table 4.2 – Load cases simulated in the shaft thermal transport validation study

Case	Switching Frequency [Hz]	Average Flux Density [T]	Rotor Iron Core Loss [W/lb.]
1	400	1.0	4.8
2	400	0.7	2.6
3	400	0.4	0.92

The resulting convection coefficients for the shaft and end cap are displayed in Table 4.3. As discussed previously, the shaft extension is treated a rotating cylindrical fin and the end cap is treated as a vertical plate with natural convection.

Table 4.3 - Resulting convection heat transfer coefficients for each load case in the shaft thermal transport validation study

Case	h_{shaft} [W/m^{2}K]	$h_{end\ cap}$ [W/m^{2}K]
1	56.53	4.27
2	56.71	3.81
3	57.02	3.15

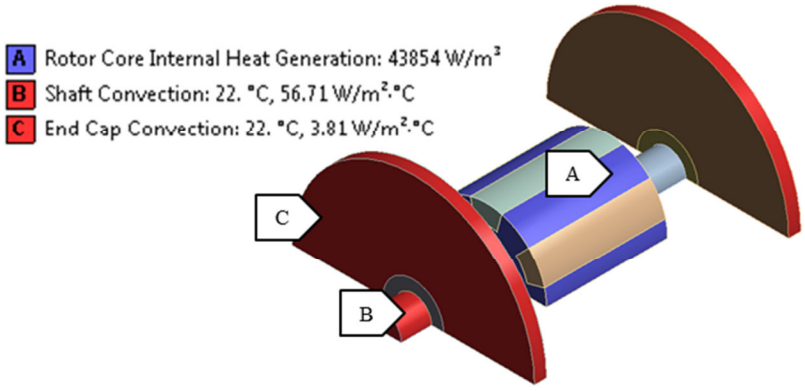

Figure 4.8 - FEA internal heat generation and boundary conditions

The initial shaft transport thermal circuit only included a heat transfer path from the inner surface of the rotor into and through the shaft out to ambient. The shaft thermal circuit methodology was validated using 3D FEA illustrated in Figure 4.8. The thermal circuit was improved to include an addition heat path through the bearings and end caps to ambient. Table 4.4 shows the results from FEA and FD for each case. The percentage error between the FEA and FD results shows larger error in shaft only model when compared to the shaft and end cap results. The initial results from the shaft thermal transport validation were a maximum temperature error of 23.46 °C and 14.02%. The improved shaft thermal circuit methodology overestimates the maximum temperature in the rotor by 6.86 °C and 4.10%. The error increases with increased internal heat

generation as shown by a maximum temperature difference of 14.02% in case 1. The temperature of the combined shaft and end cap transport models is lower than that of the individual model. This was to be expected as two thermal resistance values in parallel produce a lower equivalent resistance. The FEA and FD results for case 2 are illustrated in Figure 4.9.

Table 4.4 - Results for shaft thermal transport validation study

Case	FEA Max Temp [°C]	FD Max Temp [°C]	Temperature Difference [°C]	Percentage Error [%]
Shaft only				
1	167.38	190.84	23.46	14.02
2	100.77	113.27	12.50	12.40
3	49.87	54.16	4.29	8.61
Shaft & End Cap				
1	167.38	174.24	6.86	4.10
2	100.77	104.49	3.72	3.69
3	49.87	51.19	1.32	2.65

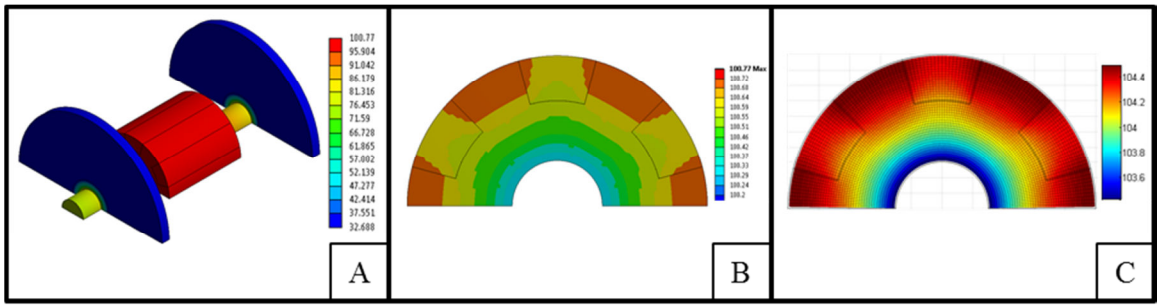

Figure 4.9 - Temperature distribution for shaft and end cap case 2 from FEA (A) and (B) and finite difference (C)

4.6 Air Gap Heat Transfer

The stator model including frame thermal transport and the rotor model including shaft thermal transport must be linked to create the half machine model. Air gap convection is the link that captures the heat transfer between the stator and rotor. The

calculation of the convective heat transfer coefficient depends on understanding the air flow in the air gap. Air flow in the axial direction is driven by pressure difference in end wells. The machines modeled are symmetric about the machine mid-plane, therefore the temperature difference (i.e. pressure difference) between the two end wells is assumed to be negligible. The air flow in the circumferential direction is driven by viscous drag on the surface of the rotor. Axial air flow is assumed to be negligible when compared to the air flow in the circumferential direction.

The air flow in the air gap was considered to fall into one of the three flow regimes: laminar shear flow (Couette flow), laminar flow with vortices (Taylor flow), and turbulent flow. The convection coefficient for each of the flow regimes is found using Nusselt correlations from Howey [46]. Laminar shear flow, laminar flow with vortices, and turbulent flow are described respectively in correlations (4.42)-(4.44).

$$Nu_{ag} = \frac{2\left[\left(R_{s,i} - R_{r,o}\right)/R_{r,o}\right]}{\ln\left[1 + \left(R_{s,i} - R_{r,o}\right)/R_{r,o}\right]} \tag{4.42}$$

$$Nu_{ag} = 0.128\left(Ta^2 / F_g{}^2\right)^{0.367} \tag{4.43}$$

$$Nu_{ag} = 0.409\left(Ta^2 / F_g{}^2\right)^{0.241} \tag{4.44}$$

$$Ta = \frac{\Omega \cdot R_{ag}{}^{0.5}\left(R_{s,i} - R_{r,o}\right)^{1.5}}{\nu} \tag{4.45}$$

$$F_g = \frac{\pi^2}{41.19\sqrt{S}}\left(1 - \frac{R_{s,i} - R_{r,o}}{2R_{ag}}\right)^{-1} \tag{4.46}$$

$$S = 0.057\left(1 - 0.652\frac{\left(R_{s,i} - R_{r,o}\right)/R_{ag}}{1 - \left(R_{s,i} - R_{r,o}\right)/2R_{ag}}\right) + 0.00056\left(1 - 0.652\frac{\left(R_{s,i} - R_{r,o}\right)/R_{ag}}{1 - 0.652\left(R_{s,i} - R_{r,o}\right)/2R_{ag}}\right)^{-1} \tag{4.47}$$

In (4.45)-(4.47), Ta is the Taylor number, Ω is the rotational speed of the rotor, R_{ag} is the air gap radius, $R_{s,i}$ is the inner stator radius, $R_{r,o}$ is the outer rotor radius and F_g is a geometric factor. The algorithm summarizing the process for determining the convection heat transfer coefficient is illustrated in Figure 4.10.

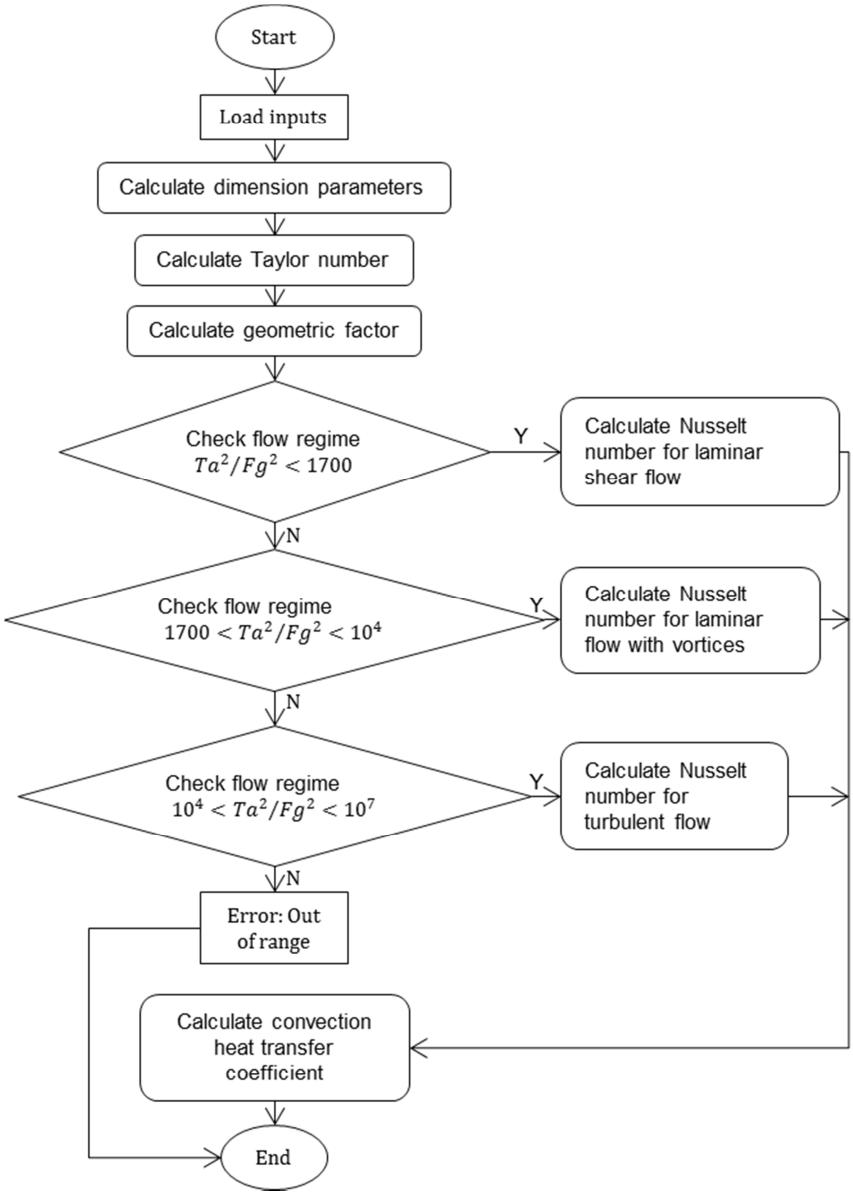

Figure 4.10 - Air gap convection heat transfer coefficient algorithm

The air gap is meshed to create a single node in the radial direction. This allows the air gap node to be linked to both the inner stator and outer rotor nodes. The temperature of the air gap is solved *in situ* using convection thermal resistance values. The air gap temperature is used to perform iterations to capture changes in properties of the air.

4.7 Finite Element Analysis Study

Verification of the complete thermal model is examined to identify the accuracy of the model. The finite element analysis software package, ANSYS, is used to examine the temperature distribution of the three dimension model of the half machine. The three dimensional model is sectioned at the axial midpoint for comparison to the finite difference model. The properties used in the thermal model verification are illustrated in Table 4.5.

Table 4.5 - Properties used in the thermal model validation study

Property	Value	Unit
L_{axial}	20	mm
L_{frame}	40	mm
$D_{air\ gap}$	24.7	mm
Air gap thickness	0.3	mm
k_{iron}	28.00	W/m K
$k_{potting}$	1.00	W/m K
k_{shaft}	60.50	W/m K
$k_{winding}$	1.00	W/m K
k_{frame}	177.00	W/m K
k_{air}	0.03	W/m K
$k_{bearing}$	0.40	W/m K

The test cases tested high and low values for both the ohmic loss in the windings and the core loss in the electric steel of the stator and rotor. The stator has a larger volume than the rotor resulting in more total loss in the stator. This validation uses an average flux density, therefore a uniform internal heat generation distribution. The actual spatial flux density and resulting heat generation from core loss could be solved with an electromagnetic simulation for improved results. The loss values for each case in the validation are displayed in Table 4.6.

Table 4.6 - Input parameter used in the thermal model validation study

Case	$Loss_{winding}$ [W]	Switching Frequency [Hz]	Flux Density [T]	Rotor Iron Core Loss [W/lb.]	$Loss_{stator\ iron}$ [W]	$Loss_{rotor\ iron}$ [W]
1	10	400	1.0	4.8	2.54	0.30
2	5	400	1.0	4.8	2.54	0.30
3	10	400	0.5	1.5	0.79	0.09
4	5	400	0.5	1.5	0.79	0.09

The resulting convection coefficients for each simulated case are illustrated Table 4.7. The temperatures of the frame and air gap vary from case to case resulting in the variety of convection coefficients. Meanwhile the temperature of the shaft extension past the end cap and rotation speed remain uniform resulting in no change in the shaft convection coefficient.

Table 4.7 - Resulting convection heat transfer coefficients for each load case in the FEA validation study

Case	h_{frame} [$W/m^2 K$]	h_{shaft} [$W/m^2 K$]	$h_{air\ gap}$ [$W/m^2 K$]
1	6.77	62.76	100.89
2	6.14	62.76	96.16
3	6.57	62.76	99.00
4	5.82	62.76	94.27

The calculated internal heat generation and boundary conditions for each case was loaded into FEA as inputs as illustrated in Figure 4.11.

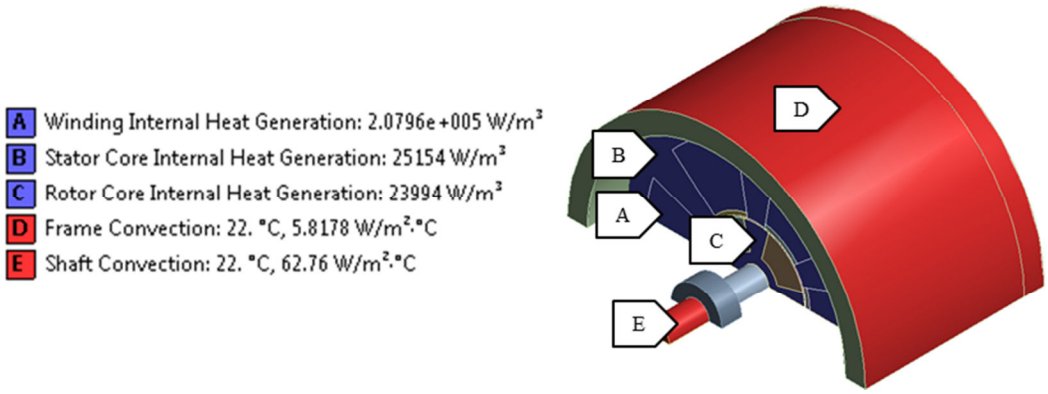

Figure 4.11 - Boundary conditions and internal heat generation location identification for the SRM FEA validation

The maximum temperature results from the FEA and FD for each case is illustrated in Table 4.8. The percentage differences between the FEA and FD results become larger as the total thermal input is increased. Figure 4.12 shows the three dimensional and mid-plane FEA and FD temperature distributions.

Table 4.8 - FEA and FD maximum temperature results for the thermal model validation study

Case	FEA Max Temp [°C]	FD Max Temp [°C]	Temperature Difference [°C]	Percentage Error [%]
1	110.93	114.71	3.78	3.41%
2	79.65	81.93	2.28	2.86%
3	100.51	104.31	3.80	3.78%
4	68.20	70.49	2.29	3.36%

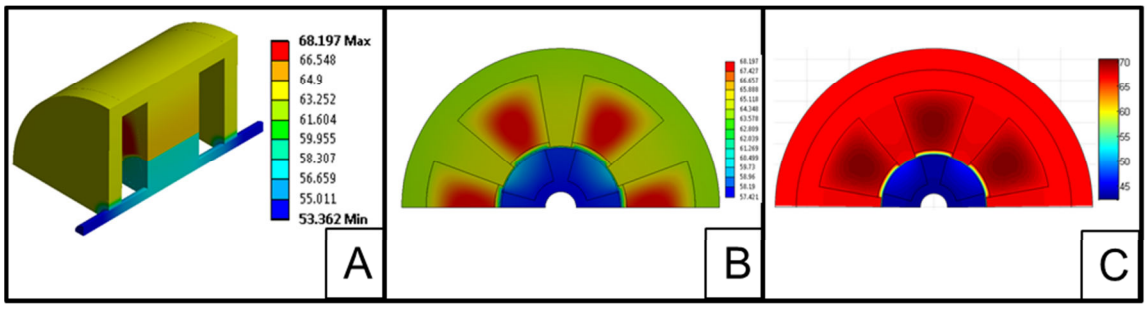

Figure 4.12 - Temperature distribution for the thermal estimator validation from FEA (A) and (B) and FD (C)

The finite difference thermal model slightly overestimated the maximum temperature values for a variety of different load cases. The largest maximum temperature difference and maximum percentage error were 3.8 °C and 3.78% respectively. The FD temperature distribution in the stator and frame of the machine agree well with the FEA results. The rotor temperature distribution in the rotor of the finite difference model is much cooler than that in the FEA model. This is thought to be caused by heat being transferred from the stator to the rotor not only though the air gap but through the end caps, through the bearing and back into the shaft. The frame heat transport in the FD model only captures the heat transfer from the stator to the surface of the frame and end caps. Linking the two individual heat transport model is proposed to alleviate the temperature error in the rotor.

4.8 Experimental Validation

Although the FEA analysis is assumed to produce relatively accurate results, empirical data is needed to verify the model to greater degree of certainty. A switched reluctance machine was designed to run at 50,000 rpm. The experimental validation was conducted on this 4/2 switched reluctance machine.

4.8.1 Switch Reluctance Machine Build

The material chosen for the experimental laminates was a non-grain oriented electric steel from Arnold Magnetic Technologies [56]. The nominal lamination thickness of the Arnon 5 material was 0.005” (0.127 mm). The stator laminates were produced using an OMAX 2626 abrasive water jet machine. The OMAX machine has an optimal cutting tolerance of ±0.003” (±0.08 mm) [57]. This time saving process can achieve high levels of dimensional accuracy but results in burr formation and rusting of the electric steel. Manual deburring was required to ensure proper laminate stacking. The stack of

laminates was held together using a jig while the outer diameter was turned to its final dimension. The frame was turned with circumferential fins to enhance the heat transfer from the machine to the ambient. The stator laminates were located within the frame using a shrink fit and further held in place using two press fit ring on either end. The inner diameter of the stator was turned to its final dimension ensure concentricity with the frame. Copper magnet wire was wound into coils to be placed around each stator tooth. A winding counter was used to ensure the proper number of turns was achieved for each coil. High thermal conductivity epoxy was used to hold the coil together when removed from the winding jig. A paper liner was used to separate the epoxy from the winding jig as well as protect the insulation on the windings when placed on the stator tooth. The rotor laminates were manufactured using a similar approach. The rotor was positioned on the shaft using a shrink fit. A radial ball bearing was fit into each end to support the shaft and rotor.

4.8.2 Experimental Setup

The experimental schematic for the SRM steady state thermal testing is displayed Figure 4.13. The SRM was internally instrumented with thermocouples (Omega 5TC-GG-T-20-36) to measure temperatures at winding tooth interface and end windings. The location of each thermocouple is described in Table 4.9. The thermocouples were connected to a 16 channel data acquisition (DAQ) system composed of a thermocouple input module (National Instruments NI 9213) and USB carrier (National Instruments NI USB-9162). The DAQ system was connected to a PC running LabVIEW SignalExpress software to record the data. The input voltage and current for each phase were measured

using voltage probes (Tektronix TDS 5054) and current probes (Tektronix TCP303) connected to a digital oscilloscope (Tektronix TDS 5054).

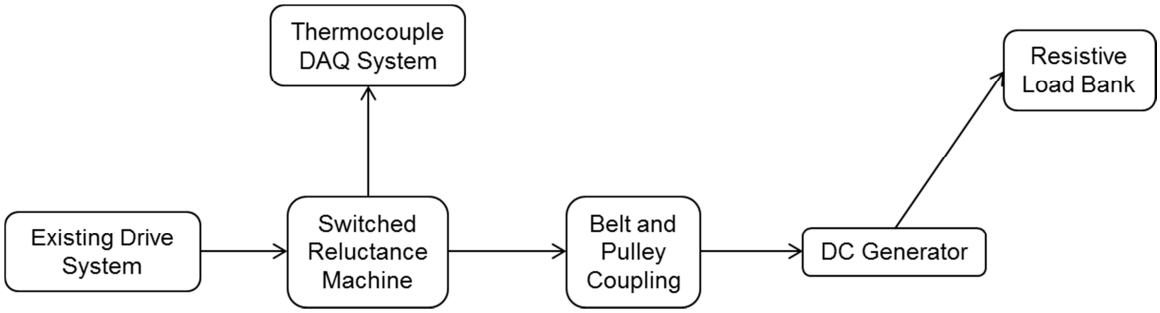

Figure 4.13 - Experimental schematic for the induction machine testing

Table 4.9 – Switched reluctance machine thermocouple locations

TC	Location
0	Ambient
1	End winding
2	End winding
3	Tooth - inner
4	Tooth - middle
5	Tooth - middle
6	Tooth - middle
7	DC generator frame

The winding resistance for each phase was measured using a digital multimeter (Fluke 187). Load was applied to the shaft using a belt and pulley system connected to a DC generator (Faulhaber 2657W024CR) as illustrated in Figure 4.14. The uncertainty values for each of the instruments used during the experimentation are displayed in Table 4.10.

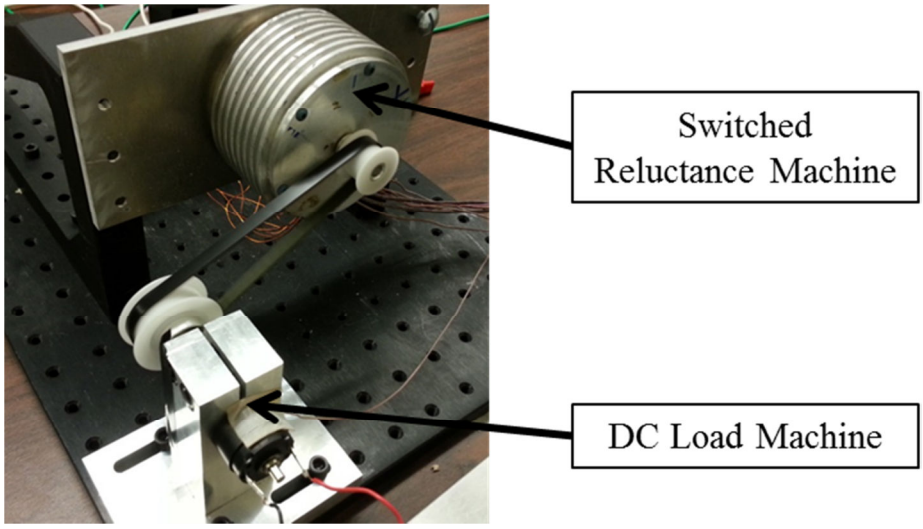

Figure 4.14 - Experimental setup for the switched reluctance machine testing

Table 4.10 - Uncertainties for the instruments used for the switched reluctance machine testing

Instrument	Manufacturer	Model Number	Uncertainty
T-Type Insulated Thermocouple	Omega	5TC-GG-T-20-36	± 0.5 °C
High Voltage Differential Probe	Tektronix	P5205	±3% of reading
Tekprobe Interface Cable	Tektronic	012-1605-01	
True RMS Multimeter	Fluke	187	DC Voltage 0.025% of reading Resistance 0.15% of reading
Non-Contact Tachometer	Extech	461700	±0.1% of reading
Current Probe	Tektronic	TCP303	±3% of reading
AC/DC Current Probe Amplifier	Tektronic	TCPA300	-
Digital Oscilloscope	Tektronic	TDS 5054	-
3-Phase Variable Transformer	Staco Energy	5011E-3Y	-
16-Channel Thermocouple Input Module	National Instruments	NI 9213	-
Hi-Speed USB Carrier	National Instruments	NI USB-9162	-

The internally built power electronics controlled the machine using an open loop methodology with no current control and no encoder.

4.8.3 Experimental Results

Six experiments of varying speeds and load conditions were conducted to validate the thermal model. Three different rotational speeds of 5,000, 7,500, and 10,000 rpm were tested to vary the air gap heat transfer as well as the core loss, which is a function of signal switching frequency. The operating condition and loading for each test is displayed in Table 4.11. The machine was mechanical designed to run at 50,000 rpm but difficulties with the power electronics limited the machine to stable speed of 10,000 rpm. At each rotational speed, the machine was run under no external load and external load provided by the couple DC generator.

Table 4.11. – Operating conditions and loads for each case in the switched reluctance machine experimental testing

Test Number	Rotational Speed [rpm]	Load	Average Input Current [A]	Stator Copper Loss [W]	Stator Core Loss [W]	Rotor Core Loss [W]
1	5,000	No	1.76	7.57	3.99	0.54
2	7,500	No	1.78	7.56	5.67	0.77
3	10,000	No	1.80	7.72	7.81	1.07
4	5,000	Yes	3.09	22.92	14.52	1.98
5	7,500	Yes	2.86	19.62	14.27	1.95
6	10,000	Yes	2.44	14.29	15.89	2.17

The transient temperature data was recorded for each thermocouple location for each test. The startup process for the machine was not very robust. It included setting the rotor angular position, timing the control system start and manually adjusting the input voltage using a variable transformer. The parts of the control system were adjusted in order to

find a stable operating condition. The instability of the machine start-up explains the large peaks and valleys and noise at the beginning of each test. The transient data for the 7,500 rpm no load test case shows a small dip in the temperature at the beginning of the test as illustrated in Figure 4.15.

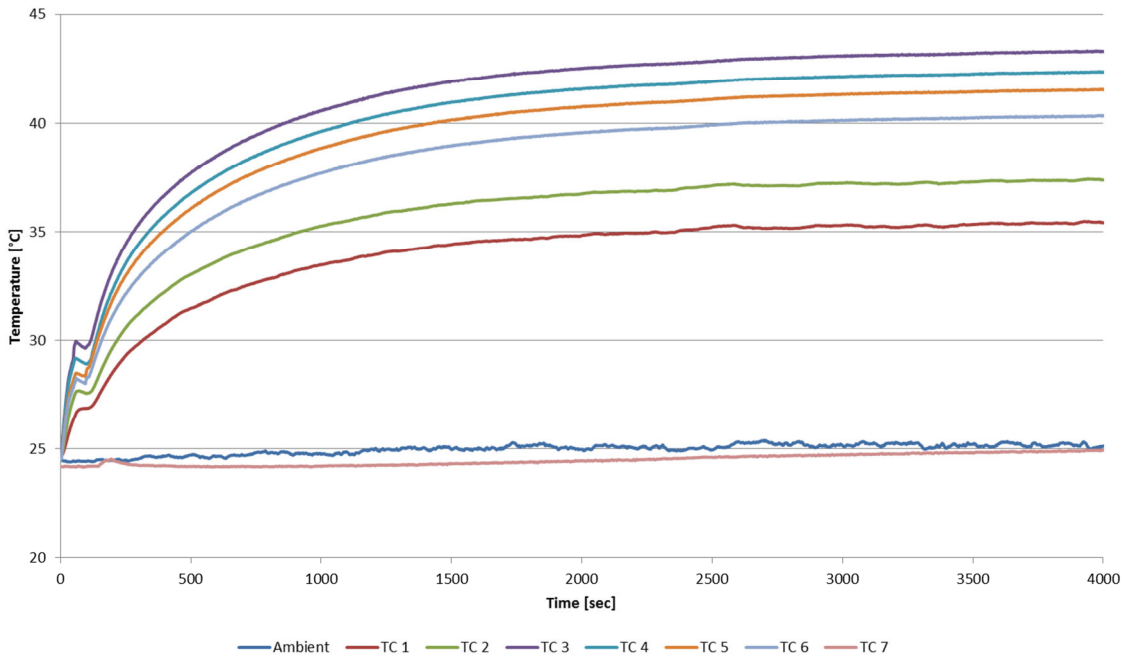

Figure 4.15- Transient temperature data for the 7.5k rpm switched reluctance machine with no external load

This one small dip is result of the first start-up process not being able to reach a steady test speed. The start-up process had to be restarted to reach the correct test speed. The transient temperature data for the 7,500 rpm loaded test, illustrated in Figure 4.16, shows two failed start-up attempts. The steep temperature rise observed in the successful start-up suggests the machine was seeing a larger amount of current. The current was controlled by manually adjusting the input voltage. The machine was able to operate in a stable condition through a range of input current values. The operating current was

recorded and used as an input to the thermal model. The temperature values for the load test were significantly higher when compared to the no load test as is expected.

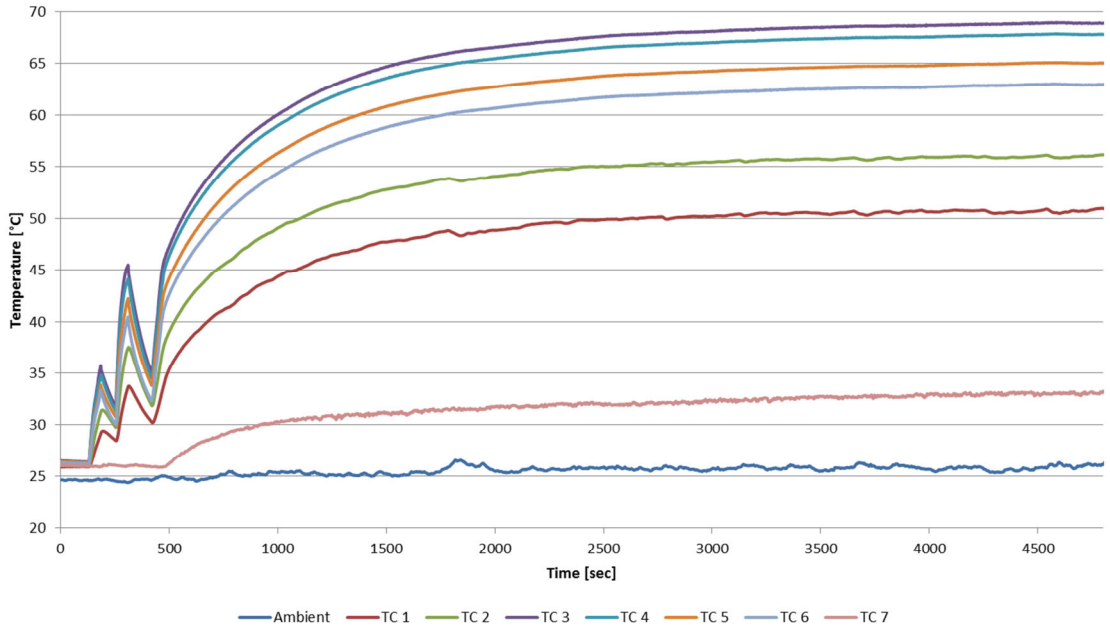

Figure 4.16 - Transient temperature data for the 7.5k rpm switched reluctance machine with external load

The transient data for the 10,000 rpm loaded test case, illustrated in Figure 4.17, exhibits lower maximum temperatures when compared to the 7,500 rpm loaded test. The average currents for the 7,500 and 10,000 rpm loaded cases were 2.86 A and 2.44 A respectively. This suggests that the magnitude of the input current has a greater effect on the magnitude of the maximum temperature than the operational speed.

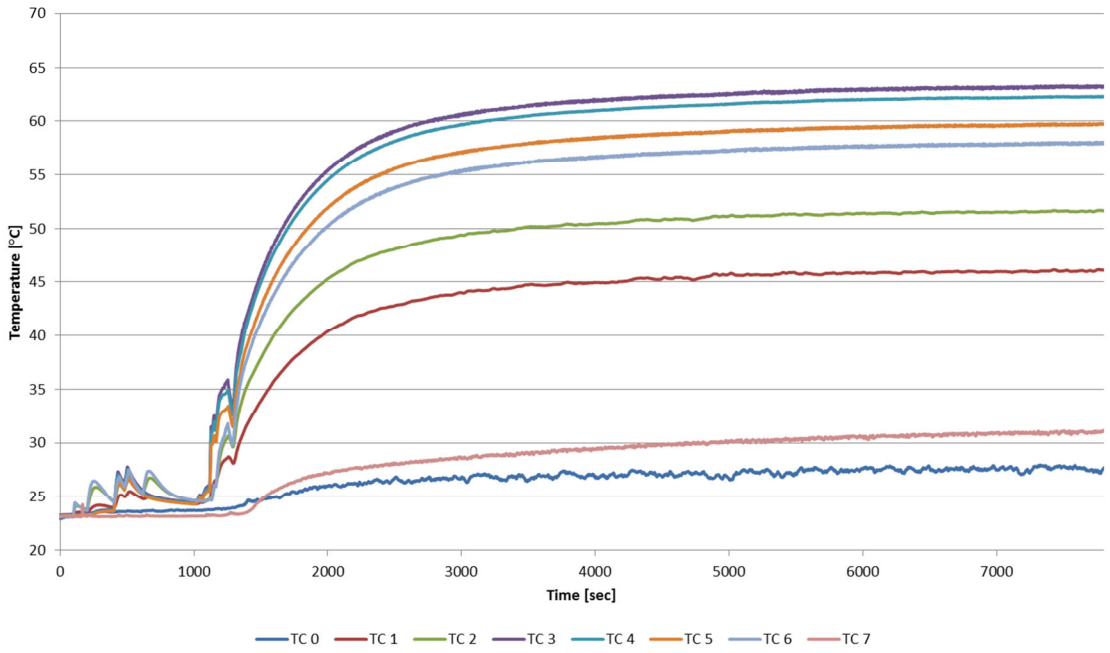

Figure 4.17 - Transient temperature data for the 10.0k rpm switched reluctance machine with external load

The input power to the machine, P_{in}, was calculated using an oscilloscope function. The stator cooper loss for each phase, L_w, was calculated using (4.48).

$$L_w = I_s^{\,2} R_s \tag{4.48}$$

The current per phase, I_s, was measured in situ with the oscilloscope and the winding resistance, R_s, was measured with a multimeter prior to the test. The output power of the DC generator, P_g, in each of the load cases was calculated using (4.49).

$$P_g = \eta_p \cdot \frac{V_g^{\,2}}{R_l} \tag{4.49}$$

The output voltage of the DC generator, V_g, and total load resistance, R_l, was measured using the digital multimeter. The system efficiency of the pulley system, η_p,

was assumed to be 80%. The total core loss of the machine, L_c, was calculated using (4.50).

$$L_c = P_{in} - P_g - L_w \tag{4.50}$$

The total core loss was divided into individual stator and rotor core loss values using a ratio of volumes. The experimental maximum temperature was compared to the resulting FD maximum temperature for each test case. The resulting loss values, maximum measured temperature, maximum FD temperature and comparisons between FD and FEA are illustrated in Table 4.12. The resulting FD temperature distribution for each case is illustrated in Figure 4.18.

Table 4.12 – Switched reluctance machine experimental loads with resulting experimental and FD maximum temperature results

Test Number	Max Measured Temperature [°C]	Max Calculated Temperature [°C]	Temperature Difference between Experimental and FD [°C]	Percentage Difference [%]
1	43.74	46.18	2.44	5.58%
2	43.32	46.96	3.64	8.40%
3	45.85	48.43	2.58	5.63%
4	82.83	87.33	4.50	5.44%
5	68.95	79.75	10.80	15.67%
6	63.3	67.98	4.68	7.39%

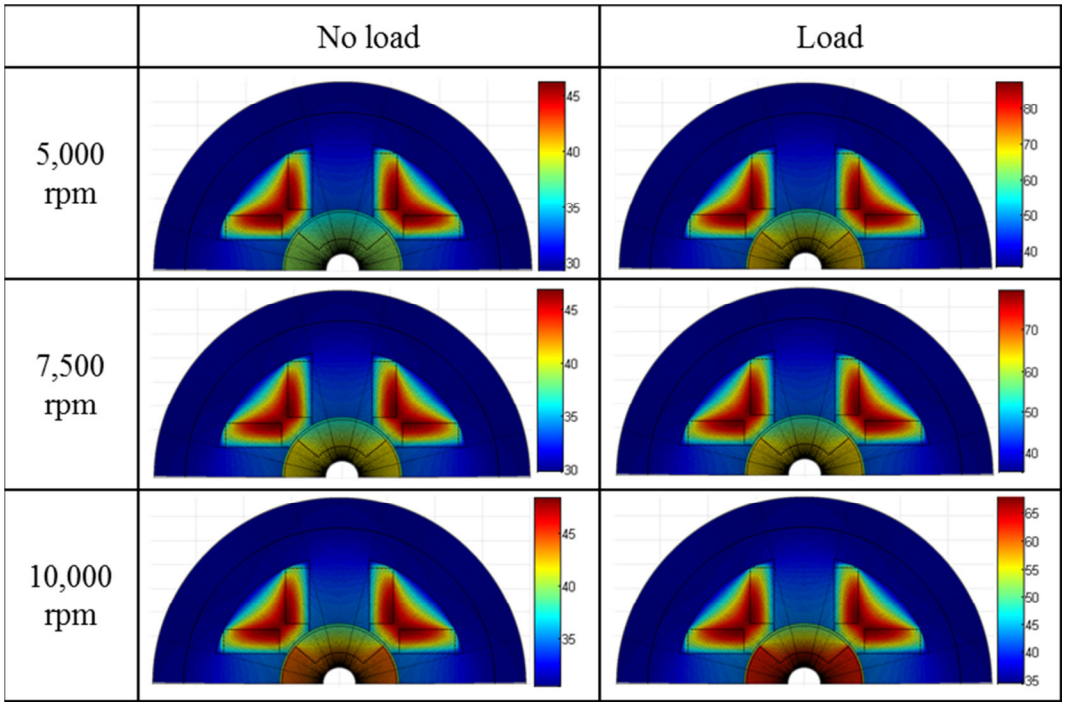

Figure 4.18 - FD temperature distribution for each case of the SRM experimental testing

The FD model overestimated the maximum temperature for each test case. The model exhibited a large error for cases when the machine was run at 7,500 rpm. The experimental maximum temperatures appear to be low for the amount of total power being input into the machine. The boundary conditions for each test were uniform with only a slight variation in ambient temperature. This suggests that the machine and the power electronics run more efficiently at this certain speed. Spot checks on the FD temperature distribution at thermocouple locations were performed to further investigate the accuracy of the model. Comparisons between the measured temperatures and the predicted temperatures are displayed in Table 4.13.

Table 4.13 - Spot location temperature comparison for experimental and FD results for the SRM experimental validation

	Test Case	Experimental Temperature [°C]	FD Temperature [°C]	Temperature Difference [°C]	Percentage Difference
Inner Tooth	1	43.7	46.0	2.3	5.24%
	2	43.3	46.8	3.5	8.10%
	3	45.9	48.3	2.5	5.39%
	4	82.8	86.9	4.1	4.94%
	5	69.0	79.4	10.5	15.17%
	6	63.3	67.8	4.5	7.06%
Middle Tooth	1	41.6	44.5	2.9	6.90%
	2	41.4	45.4	4.0	9.70%
	3	44.1	46.9	2.8	6.35%
	4	77.4	82.1	4.7	6.12%
	5	65.3	75.2	9.9	15.18%
	6	60.1	65.0	4.9	8.14%

The results from the spot checks follow the same trends exhibited in the maximum temperature comparison. The inner tooth location shows slightly smaller errors while the middle tooth location show slight larger errors on the average when compared to the maximum temperatures. The large error for the 7,500 rpm cases is seen for all the comparison locations. More experimental cases around this rotational speed would be helpful in determining the definite cause of this error.

4.9 Discussion

The finite difference approach used in the thermal estimator was adapted from the work of Semidey [5]. Annular fins were added to the frame boundary conditions which already included smooth and axially finned frames experiencing natural and forced convection. The addition of the rotor in the thermal model required a method to describe the heat transfer through the air gap and through the shaft of ambient. The shaft thermal transport initially ignored the heat transfer though the bearing and the end caps. This

resulted in large errors but was fixed by adding the parallel heat path through the bearings and onto the surface of the end caps. The shaft thermal transport was validated using 3D FEA. The Nusselt correlation for the heat transfer in the air gap can be broken into three flow regimes: laminar shear flow, laminar flow with vortices, and turbulent flow. The 3D thermal model validation resulted in higher maximum temperature in the FD module when compared to FEA. The three dimensional FEA shows uniform temperature distribution on the surface of the frame and end caps. The high thermal conductivity of the frame and end caps and the low convection coefficient attribute to this temperature distribution. The shaft has larger temperature gradients due a lower thermal conductivity and a higher convection coefficient. The temperature of the frame in the FD result is slightly higher because it is not connected to the shaft thermal transport. Experimental testing was conducted to further validate the thermal model. The experiment machine and its control system were internally designed and manufactured. This led to uncertainties in the model including the calculation of the effective thermal conductivity of the windings, the efficiency of the pulley system, and the efficiency of the control system.

4.10 Summary

This chapter discussed the finite difference thermal model used to estimate the temperature distribution in a switched reluctance machine. A brief overview of the finite difference approach and solution algorithm was presented. A new frame boundary condition of an annular fin setup was described. A shaft thermal transport approach was discussed and varied. The finite difference model was able to predict the maximum temperature in the rotor with 6.86 °C and an error of 4.10% when compared to the FEA. The heat transfer in the air gap was described for three flow regimes. A 3D comparison

between the FD and FEA temperature distribution in the frame, stator and rotor of the machine was conducted. The finite difference thermal model overestimated the maximum temperature values for a variety of different load cases. The maximum temperature difference and maximum percentage error were 3.80 °C and 3.78% respectively. Data was collected from an experimental switch reluctance machines for six different speed and load cases and compared to the finite difference thermal solution. The finite difference thermal model was able to predict the maximum temperature to within 10.80 °C. Spot check of the temperature distribution showed close correlation to the FD model at two experimental locations as well as the maximum temperature.

CHAPTER 5

INDUCTION THERMAL MODEL

5.1 Introduction

In the previous chapter, the electric machine losses were identified as ohmic loss in the windings, stator core loss and rotor core loss. The induction machine thermal model includes another source of internal heat generation, the ohmic loss in the rotor bars. The current distribution in the rotor bars during start up and acceleration can be difficult to determine due to skin effects [58]. Uneven distribution of current leads to differential heating and causes differential thermal expansion. The cycling of this thermal expansion introduces mechanical stresses that can lead to fatigue related failure. This model examines the temperature distribution of half of an induction machine. Half of the machine was chosen because it is a line of symmetry common to all induction machines with an even umber of stator and rotor teeth.

5.2 Problem Statement

The thermal model is designed to input for the four machine losses and machine geometry and predict the temperature distribution. The result will identify hot spots and help avoid machine failure due to winding insulation and material degradation. This model uses parametric values to describe the dimension of the machine. This allows for quick size adjustments to the machine and future optimization integration. The winding ohmic loss, stator core loss and rotor core loss are determined using the same algorithms as discussed in the SRM thermal model. The induction model includes the addition loss of ohmic heating in the rotor bars. The internal heat generation in the rotor bars, $\dot{q}_{rotor\ bar}$,

is calculated in (5.1) where $\dot{E}_{ohmic}$ is the ohmic loss and $V_{rotor\ bar}$ is the volume of the rotor bar.

$$\dot{q}_{rotor\ bar} = \frac{\dot{E}_{ohmic}}{V_{rotor\ bar}} \tag{5.1}$$

The ohmic loss, calculated in (5.2), is a function of the induced current in the rotor bars, I, and the resistance of the rotor bars, R.

$$\dot{E}_{ohmic} = I^2 \cdot R \tag{5.2}$$

The induced current in the rotor bars can be solved using electromagnetic simulations. The current distribution for the steady state thermal model is assumed to be uniform. This assumption breaks down at machine start up and acceleration. The validation of the thermal model, in which the machine losses are inputs not outputs, uses current density values commonly found in the rotor bar of induction machines [53]. The rotor bar current, calculated in (5.3), is a function of this specified current density, J, and the cross-sectional area of the rotor bar, A.

$$I = J \cdot A \tag{5.3}$$

The resistance in the rotor bar can be found experimental or analytically. The analytical solution, (5.4), is a function of the rotor bar resistivity, ρ, the length of the rotor bar, l, the end ring factor, f, and the cross section area of the rotor bar.

$$R = \frac{\rho \cdot l \cdot f}{A} \tag{5.4}$$

The volume of a rotor bar is calculated in (5.5).

$$V_{rotor\ bar} = f \cdot l \cdot A \tag{5.5}$$

Rearranging (5.1)-(5.5) results in a simplified equation for the rotor bar internal heat generation, displayed in (5.6).

$$\dot{q}_{rotor\ bar} = J^2 \cdot \rho \tag{5.6}$$

The model must be able to accurately capture the temperature distribution of the induction machine to within half of the range between winding insulation classes.

5.3 Finite Element Analysis Study

Finite element analysis was used to initially validate the thermal model. The same input loads and boundary conditions were applied to the FEA and FD models. The first validation study examines the thermal differences between the two dimensional rotor half slots meshed in FEA and the half slot meshed using the algorithms discussed in a previous chapter. The next study compares the three dimensional half machine temperature distribution results from FEA and FD. This study examines how well the thermal circuits used in the model are able to capture the three dimensional effects. The final validation study compares the maximum temperate values and temperature distribution found experimental and using the FD thermal model. The parameters used in each study were measured from a WEG 3 phase ¼ horsepower induction machine (2518OS3EA56) [59]. The dimensions for the machine are illustrated in Figure 5.1.

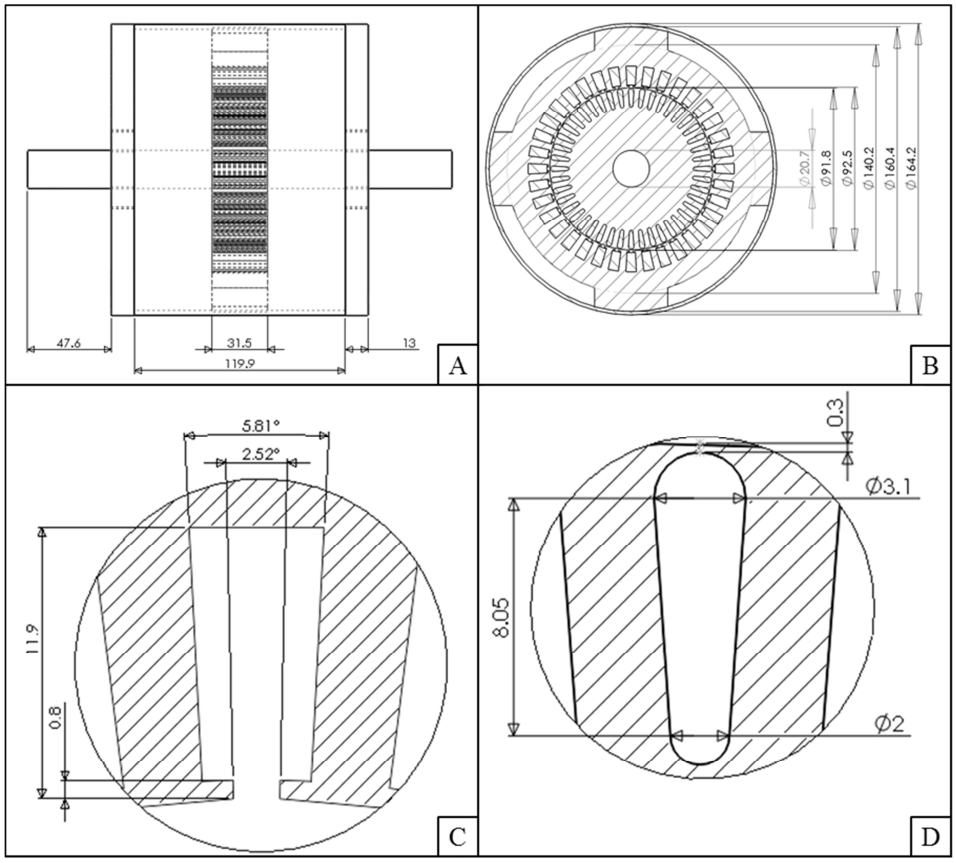

Figure 5.1 - Induction machine axial dimensions (A), radial dimension (B), stator slot dimensions (C) and rotor bar dimensions (D)

The parameters for the 1750 rpm 36/44 induction machine used for all the validation studies are displayed in Table 5.1. The rotor bars used in the study are made of aluminum.

Table 5.1 - Parameters used in the validation studies

Property	Value	Unit
k_{iron}	28.0	W/m K
$k_{rotor\ bar}$	177.0	W/m K
k_{shaft}	60.5	W/m K
$k_{winding}$	1.0	W/m K
k_{frame}	177.0	W/m K
$k_{bearing}$	0.2	W/m K
ρ_{Al}	2.82E-08	Ω-m

5.3.1 2D Half Slot Rotor Bar Study

The two dimensional half slot study is a further validation of the accuracy achieved by the meshing and segmentation algorithms of a previous chapter. The previous study compared the cross-sectional area difference between the meshed rotor bars and the actual rotor bars. This study examines the effect that this difference in area has on the thermal distribution. The cross-sectional areas for the rotor bars calculated by the CAD model and the FD mesh and segmentation algorithms are displayed in Table 5.2.

Table 5.2 - Cross sectional areas of the rotor bar in CAD and in FD

Rotor Bar Geometry	Rotor Bar CAD Area [mm^2]	Rotor Bar FD Area [mm^2]	Area Difference
A	17.10	17.13	0.20%
B	15.98	15.92	-0.36%
C	13.09	13.04	-0.40%
D	11.67	11.73	0.53%
E	12.93	12.93	-0.03%
F	9.98	10.04	0.64%

The mesh and segmentation algorithms slightly over predict the area for rotor bars A, D and F and under predict the area for rotor bars B, C, and E. The difference in areas is predicted to be a factor for the difference in temperature distribution in the thermal

model. An increased amount of area results in more total heat inputted into the model. The internal heat generation for the rotor iron and rotor bar is a factor of the flux density and the current density respectively. The iron loss was determined using manufacturer data provided for Arnon 5 electric steel for 400 Hz at 0.2 T and 1 T. The rotor bar current densities of 2.2 and 7 were chosen using common values described by Harley [53]. Boundary conditions of 10 W/m-K and 50 W/m-K were chosen for the air gap and shaft convection respectively. The test cases which use a high and low value for the flux density and current density are displayed in Table 5.3.

Table 5.3 - Rotor iron and rotor bar load for each test case

Case	Core Loss [W/lbs.]	Rotor Bar Current Density [A/mm^2]
1	2.3	2.2
2	2.3	7
3	4.8	2.2
4	4.8	7

The maximum temperature results for each of the rotor bar geometries at each load case are displayed in Table 5.4.

Table 5.4 - Maximum temperature results from FEA and FD for each test case

Rotor Bar	Case	FEA Max Temp [°C]	FD Max Temp [°C]	Temperature Difference [°C]	Percentage Difference
A	1	60.2	60.2	0.1	0.10%
	2	377.8	378.4	0.6	0.17%
	3	118.8	118.9	0.0	0.01%
	4	436.5	437.0	0.6	0.13%
B	1	58.0	57.9	-0.1	-0.21%
	2	355.0	353.7	-1.3	-0.36%
	3	117.9	117.9	-0.1	-0.05%
	4	414.9	413.7	-1.2	-0.29%
C	1	52.3	52.2	-0.1	-0.19%
	2	295.5	294.5	-1.0	-0.35%
	3	115.5	115.5	0.0	-0.04%
	4	358.7	357.7	-1.0	-0.27%
D	1	49.5	49.6	0.1	0.23%
	2	266.5	267.6	1.2	0.44%
	3	114.4	114.4	0.0	0.03%
	4	331.3	332.4	1.1	0.33%
E	1	52.0	52.0	0.0	-0.01%
	2	292.2	292.2	-0.1	-0.02%
	3	115.4	115.4	0.0	-0.01%
	4	355.6	355.6	-0.1	-0.02%
F	1	46.2	46.3	0.1	0.29%
	2	231.7	233.1	1.4	0.60%
	3	113.0	113.0	0.0	0.04%
	4	298.7	299.7	1.1	0.36%

The results show that the geometries with under predicted area results in lower maximum FD temperatures when compared to FEA. The magnitude of the area difference correlates to the magnitude of the error in the thermal estimation. The temperature distribution of rotor bar E for case 3, illustrated in Figure 5.2, appears linear. The distribution will become less linear with lower rotor bar thermal conductivity, higher rotor bar heat generation, and different boundary conditions.

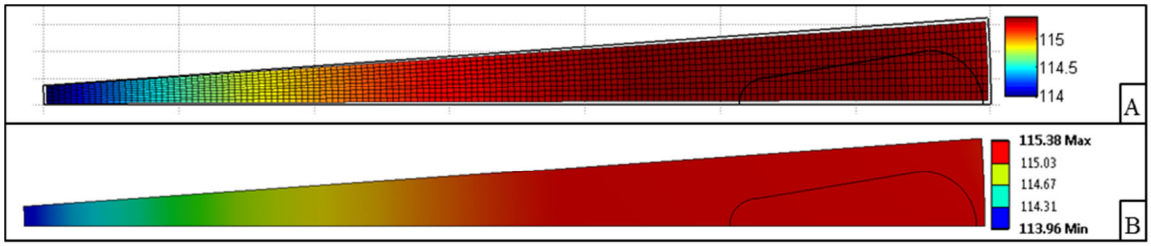

Figure 5.2 - FEA and FD temperature distribution for rotor bar geometry C case 3

5.3.2 3D Half Machine Validation Study

The 3D half machine validation study examines the accuracy of the 2D half machine finite difference temperature distribution compared to the finite element analysis temperature distribution. The thermal model uses the same thermal circuits approach to capture the thermal transport through the shaft to ambient. The machine in this study was modified to remove the air pocket between the stator and frame in the actual machine as illustrated in Figure 5.3. This reduces the uncertainty of the model caused by convection in this air pocket.

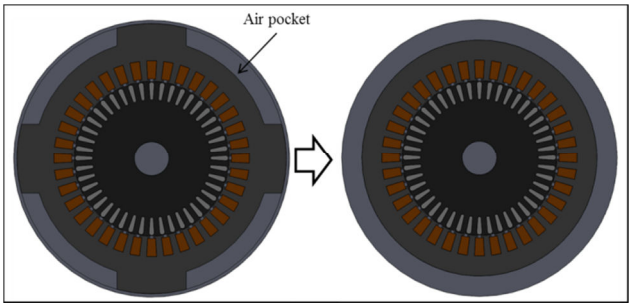

Figure 5.3 - Transformation of the stator and frame to remove the air pocket

The internal heat loads and boundary conditions used as inputs to the FEA model are displayed Table 5.5. The current densities and flux density were taken from common values described by Harley [53]. The heat transfer from the frame to ambient was considered to be natural convection over a horizontal cylinder. The heat transfer from the end cap was considered to be natural convection over a vertical plate. The circular end

cap was converted to a square geometry with an equal area for the vertical plate heat transfer coefficient calculation. The heat transfer on the surface of the shaft extension outside the frame and end cap was modeled as forced convection for a rotating horizontal cylinder using the rotation velocity to calculate air speed. The heat transfer between the stator and rotor in the air gap was modeled using Nusselt correlations described by Howey [46]. All of the correlations are the same as the ones used in the switched reluctance thermal model. The equations defining the convection coefficients can be found in the previous chapter.

Table 5.5 - Loads and boundary conditions for each of the test cases in the 3D half machine validation study

Case	Winding Current Density [A/mm^2]	Stator Iron Loss [W/lbs.]	Rotor Bar Current Density [A/mm^2]	Rotor Iron Loss [W/lbs.]	h_{frame} [W/m_2K]	$h_{end\ cap}$ [W/m_2K]	h_{shaft} [W/m_2K]	$h_{air\ gap}$ [W/m_2K]
1	4	2.3	2	2.3	4.8241	5.1675	33.7448	81.3371
2	4	2.3	2	4.8	5.2065	5.5167	33.6727	85.3523
3	4	2.3	4	2.3	5.2065	5.5167	33.6727	85.3523
4	4	2.3	4	4.8	5.4882	5.7751	33.6158	89.6257
5	4	4.8	2	2.3	5.5137	5.7987	33.6090	84.5493
6	4	4.8	2	4.8	5.7039	5.9749	33.5605	88.7653
7	4	4.8	4	2.3	5.6814	5.9540	33.5659	88.7653
8	4	4.8	4	4.8	5.8926	6.1517	33.5181	92.6658
9	8	2.3	2	2.3	6.2565	6.4999	33.4311	92.4650
10	8	2.3	2	4.8	6.3877	6.6287	33.4029	96.4373
11	8	2.3	4	2.3	6.3877	6.6287	33.4029	96.4373
12	8	2.3	4	4.8	6.5198	6.7563	33.3489	100.3091
13	8	4.8	2	2.3	6.4944	6.7321	33.3588	95.3617
14	8	4.8	2	4.8	6.6057	6.8381	33.3182	99.4487
15	8	4.8	4	2.3	6.6057	6.8381	33.3182	99.4487
16	8	4.8	4	4.8	6.7084	6.9373	33.2804	103.2775

The boundary conditions and internal heat generation values used in the finite difference thermal model were inputted into the FEA model to validate the results. The surfaces and

volumes to which the boundary conditions and internal heat generation values are applied are illustrated in Figure 5.4.

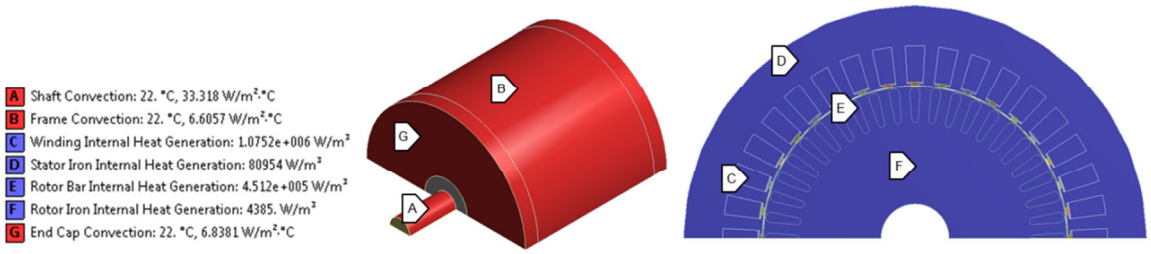

Figure 5.4 - Boundary conditions and internal heat generation location identification

The maximum temperature results for the FD and FEA are displayed in Table 5.6. The temperature distribution for each case from FEA and FD are illustrated in Figure 5.5 through Figure 5.8.

Table 5.6 - Maximum temperature values from FEA and FD for each test case

Case	FD Max [°C]	FEA Max [°C]	Max Diff [°C]	Max Diff [%]
1	59.4	56.5	2.9	5.14%
2	86.5	81.3	5.2	6.35%
3	86.1	80.9	5.2	6.37%
4	114.8	105.4	9.4	8.93%
5	78.6	74.3	4.4	5.87%
6	99.3	95.6	3.6	3.81%
7	99.0	95.4	3.6	3.78%
8	127.1	119.1	8.0	6.69%
9	125.0	118.0	7.1	5.99%
10	134.8	129.7	5.2	3.98%
11	134.7	129.3	5.4	4.16%
12	156.3	151.9	4.4	2.91%
13	141.7	133.6	8.1	6.10%
14	151.4	144.8	6.6	4.59%
15	151.3	144.6	6.7	4.64%
16	168.2	164.8	3.3	2.03%

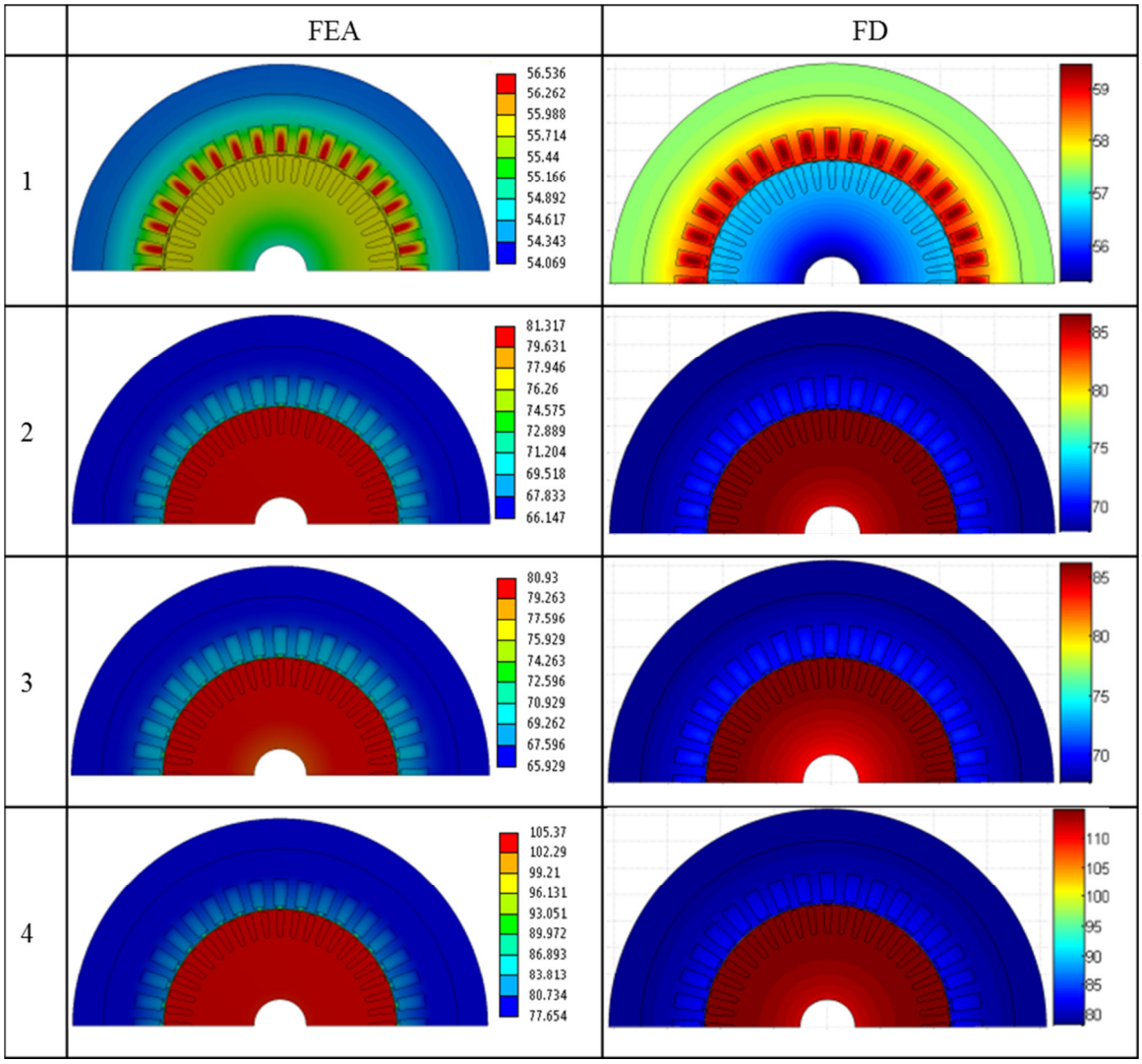

Figure 5.5 - FEA and FD temperature distribution results for cases 1-4

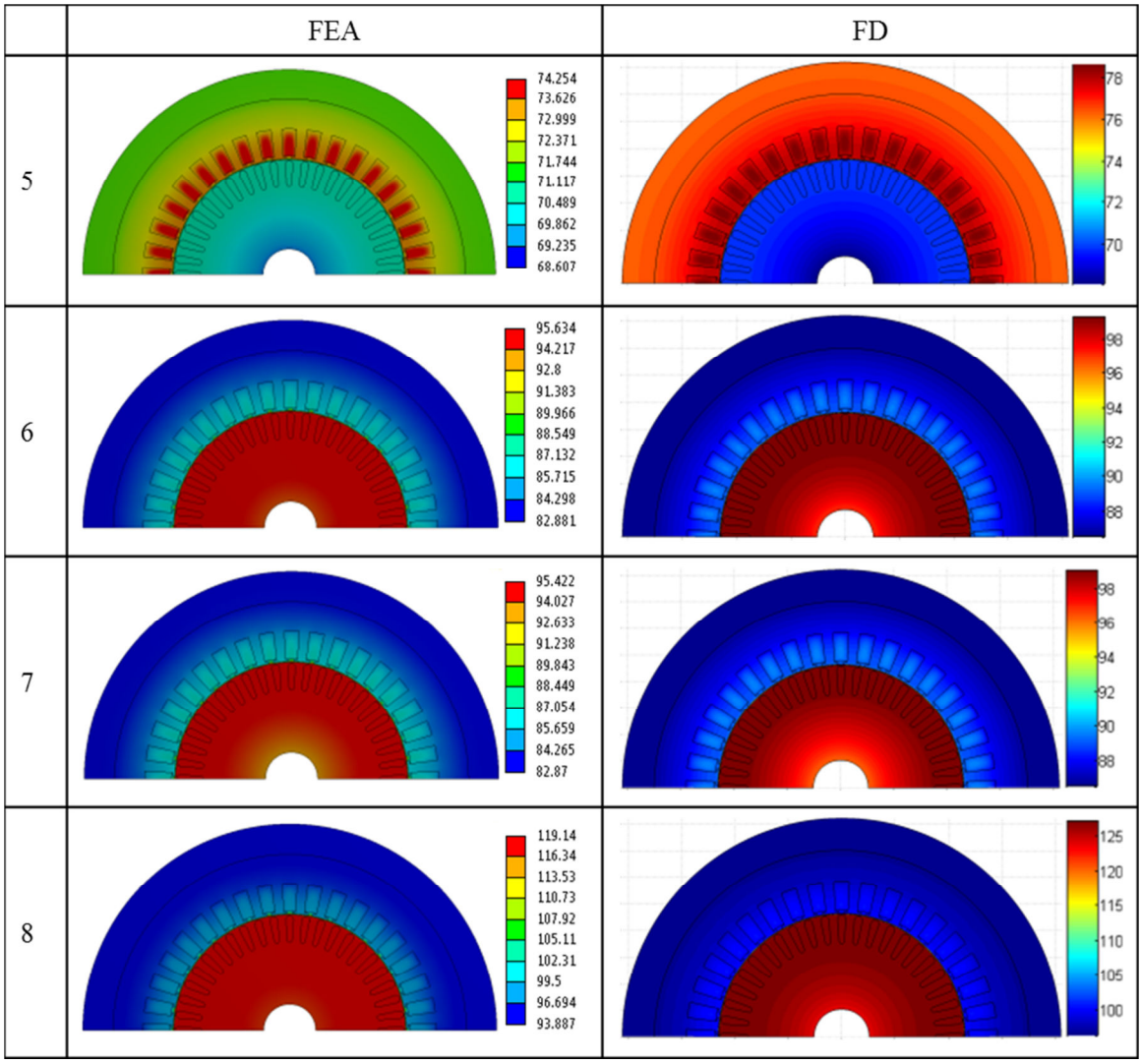

Figure 5.6 - FEA and FD temperature distribution results for cases 5-8

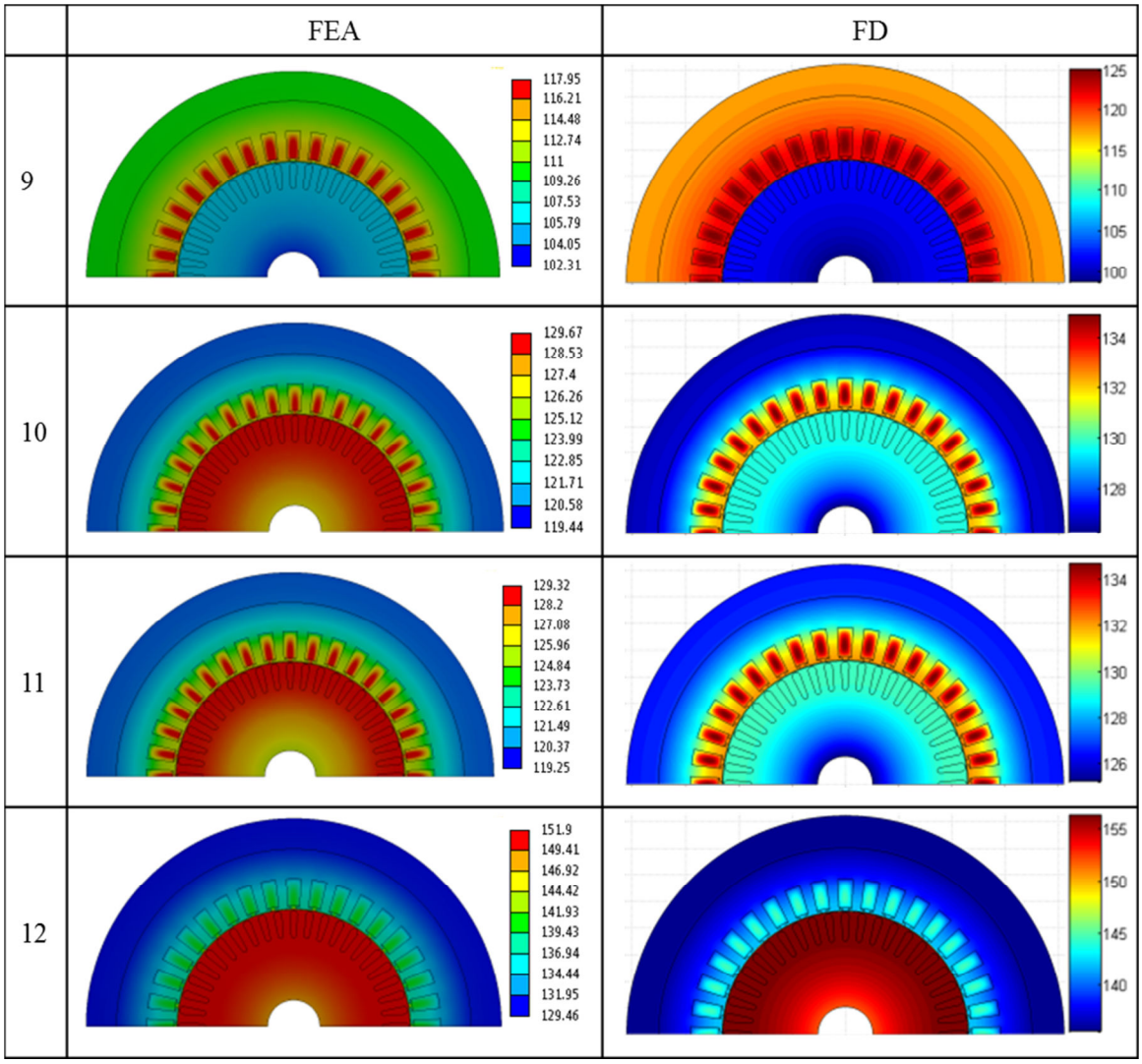

Figure 5.7 - FEA and FD temperature distribution results for cases 9-12

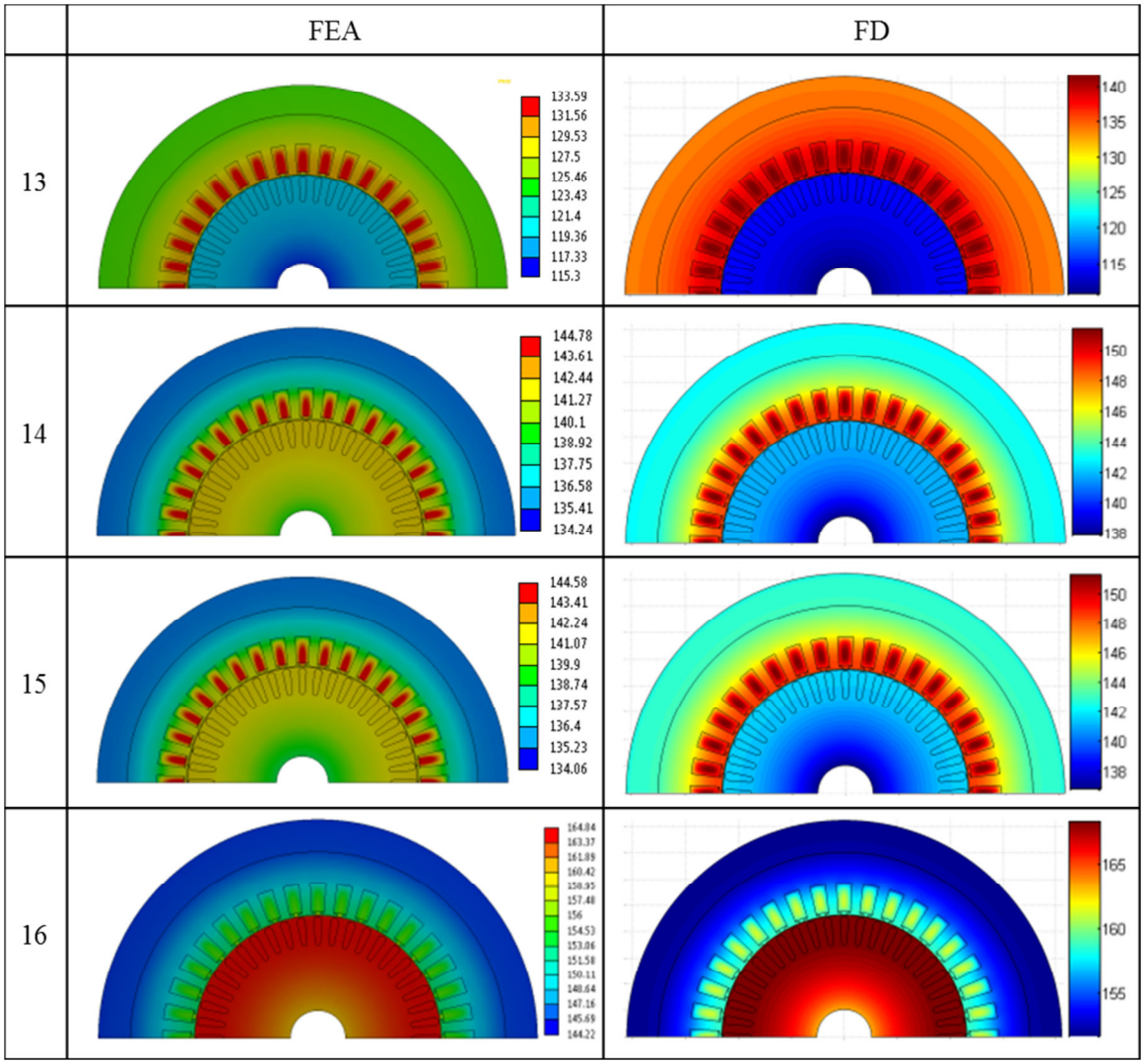

Figure 5.8 - FEA and FD temperature distribution results for cases 13-16

The finite difference model over predicted the maximum temperature when compared to the FEA in each case. The maximum temperature difference of 9.4 °C and percentage error of 8.93%, for case 4, is within half of the range between winding insulation classes (12.5 °C). A majority of the cases have similar average stator temperature to average rotor temperature ratios. The finite difference results for cases 1, 10, 11, 14 and 15 have noticeably cooler rotor temperatures when compared to the results from FEA. The 3D

FEA temperature distribution, 2D FEA temperature distribution, and 2D FD temperature distribution results for case 11 are illustrated in Figure 5.9 for further investigation.

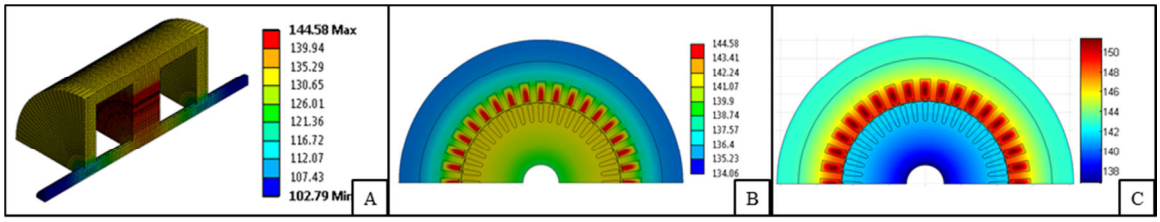

Figure 5.9 - 3D FEA temperature distribution (A), 2D FEA temperature distribution (B), and 2D FD temperature distribution (C) results for case 11

The FEA result shows a cooler frame when compared to the FD result. The 3D FEA temperature distribution suggests a heat flux path from the frame through the end cap, bearing, and shaft to ambient. The finite difference model only captures the heat transport through the frame and end cap to ambient. The omission of the heat transport through the bearing and shaft may cause the higher average temperature values seen in the FD results. Although the rotor temperatures in the FD rotor appear cooler than those of the FEA rotor, the values are quite similar.

5.4 Experimental Validation

The experimental validation was conducted on a 3-phase ¼ horsepower induction machine. The finite difference thermal model is designed to model totally enclosed machines with no internal fans or air circulation. The WEG experimental machine was modified to estimate a totally enclosed machine. Aluminum sheets covers were made to block the ventilation through the end caps. The internal fan on the shaft was removed to reduce the effects of forced convection in the end wells and between the stator and frame of the machine. Four different load cases were studied including no load, system friction load, and two DC generator loads. A duplicate of the no load case was conducted to

verify that there is a negligible variation in the steady state temperature values between cases when the boundary and starting conditions are held constant.

5.4.1 Experimental Setup

The experimental setup for the induction steady state thermal testing is displayed in Figure 5.10. The induction machine was rigidly attached to the motor test frame. The output shaft of the induction machine was coupled with the torque sensor through the use of a jaw type coupling. The torque sensor was coupled to the dc generator using a similar jaw type coupling. The output shaft torque was measured with an in-line rotary torque sensor (Omega TQ501-200) with a range of 0-22.6 N-m (0-200 in-lbs.). The experimental induction machine produces 1.02 N-m at rated load and speed which is well within the range of the sensor. The instantaneous torque value was displayed a digital meter (Omega DPF701). A 7.5 hp DC dynamometer (Westinghouse 12-N-3052) was used to increase the load on the induction machine. The power from the dynamometer was dissipated through a resistive load bank. The induction machine was loaded in order to achieve an input current of 1.1 A and 1.2 A to ensure the motor did not overheat. The load was set by adjusting the DC dynamometer armature voltage.

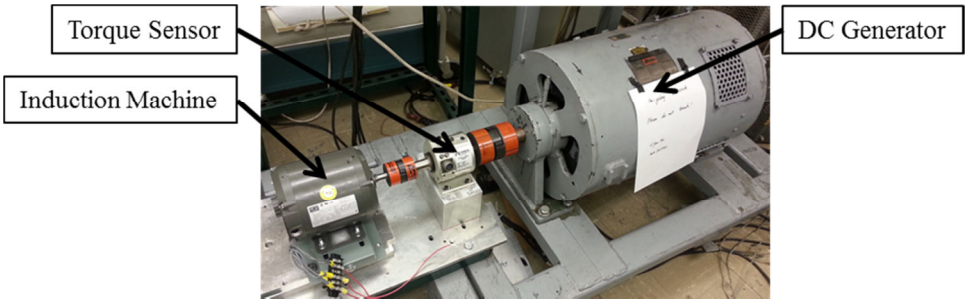

Figure 5.10 - Experimental setup for the induction machine testing

The purpose of the experiments was to collect steady state temperature data at various locations in the machine. The thermocouples were connected to a 16 channel data acquisition (DAQ) system composed of a thermocouple input module (National Instruments NI 9213) and USB carrier (National Instruments NI USB-9162). The DAQ system was connected to a PC running LabVIEW SignalExpress software to record the data. The location of each thermocouple within the machine is displayed in Table 5.7.

Table 5.7 - Thermocouple identification and corresponding induction machine location

TC	Location
0	Ambient
1	Stator winding probe
2	Stator winding probe
3	End winding
4	End winding
5	End winding
6	Stator - middle - top
7	Stator - middle - bottom
8	Stator - end - top
9	Stator - end - bottom
10	End cap - frame
11	End cap - bearing
12	Frame - inner - top
13	Frame - inner - bottom
14	Frame -outer

Thermocouple 0 (Omega 5TC-GG-T-20-36) was placed external to the machine and was used to measure the ambient temperature values throughout the duration of the test. The ambient temperature fluctuates due to movement within in the area, heat dissipated from electronic devices and the HVAC system. Thermocouples 1 and 2 (Omega KMQSS-020G-G) were probe thermocouples that were inserted into two separate

winding slots to measure the winding temperatures at the axial midpoint of the machines. Thermocouples 3, 4 and 5 (Omega SA1-K) were used the measure the end winding temperatures, a common hot spot location, for the same winding slot as the probe thermocouples. Multiple locations on the same winding slot allows for estimation of the winding axial temperature gradient. Thermocouples 6-9 (Omega SA1-K) were placed on the outer radius of the stator top provide spot checks for the validation of the FD temperature distribution. Thermocouples 10 and 11 (Omega SA1-K) were place on the inside of the end cap to capture the temperature gradient between the end cap inner radius near the bearing and the end cap outer radius near the frame. The temperature gradient will help identify the direction of the heat flux in the end cap. The direction of the heat flux can help determine whether the heat from the frame is leaving through the shaft or if the heat from the rotor is being dissipated on the surface of the end caps. Thermocouples 12 and 13 (Omega SA1-K) are located on the inner radius of the frame in the air gap between the stator and frame. This location is an area of uncertainty in the thermal model and these thermocouples provide spot checks for the finite difference solution. Thermocouple 14 (Omega SA1-K) was located on the top of the outer radius of the frame. The location of each thermocouple is illustrated in Figure 5.11.

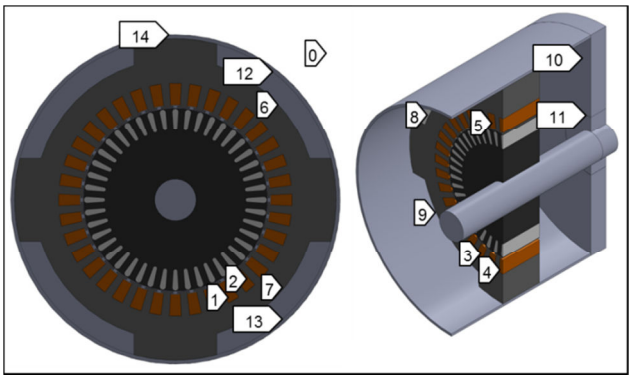

Figure 5.11 - CAD illustration of thermocouple locations

A high voltage probe (P5205) and corresponding cable (012-1605-01) was used to measure the input voltage to the experimental machine. A current probe (Tektronix TCP303) and corresponding amplifier (Tektronix TCPA300) was used to measure the input current to the experimental machine. The voltage and current probe were connected to a digital oscilloscope (Tektronix TDS 5054). The line to line voltage, RMS current and the phase angle was measured using the oscilloscope and used in the calculation of input power seen in (5.7).

$$P = \sqrt{3} V_{LL} I \cos(\phi) \tag{5.7}$$

A digital mulitmeter (Fluke 187) was used to measure the resistance of the rotor bars and machine input leads for the calculation of loss in the rotor bars and winding respectively. The speed of the machine was measured using a non-contact tachometer (Extech 461700). The uncertainty values for each of the instruments used during the experimentation are displayed in Table 5.8.

Table 5.8 - Uncertainties for the instruments used for the induction machine testing

Instrument	Manufacturer	Model Number	Uncertainty
K-Type Probe Thermocouple	Omega	KMQSS-020G-G	±1.5 °C
K-Type Self-Adhesive Thermocouple	Omega	SA1-K	±1.5 °C
T-Type Insulated Thermocouple	Omega	5TC-GG-T-20-36	± 0.5 °C
200 in-lb. In-Line Rotary Torque Sensor	Omega	TQ501-200	±0.18% FS (0.36 in-lbs.)
High Voltage Differential Probe	Tektronix	P5205	
Tekprobe Interface Cable	Tektronic	012-1605-01	±3% of reading
True RMS Multimeter	Fluke	187	DC Voltage 0.025% of reading Resistance 0.15% of reading
Non-Contact Tachometer	Extech	461700	±0.1% of reading
Current Probe	Tektronic	TCP303	
AC/DC Current Probe Amplifier	Tektronic	TCPA300	±3% of reading

5.4.2 Experimental Results

The steady state temperature values measure in each load case is used to validate the accuracy of the finite difference thermal model. The transient temperature data was recorded to observe trends in the data for different load case and to identify areas of future work. The transient temperature values for each thermocouple location for the no external load case are illustrated in Figure 5.12. The two no load test had an average RMS current of 0.99 A, average phase to phase voltage of 212 V, and a phase angle of 83° resulting in an input power of 44.3 W.

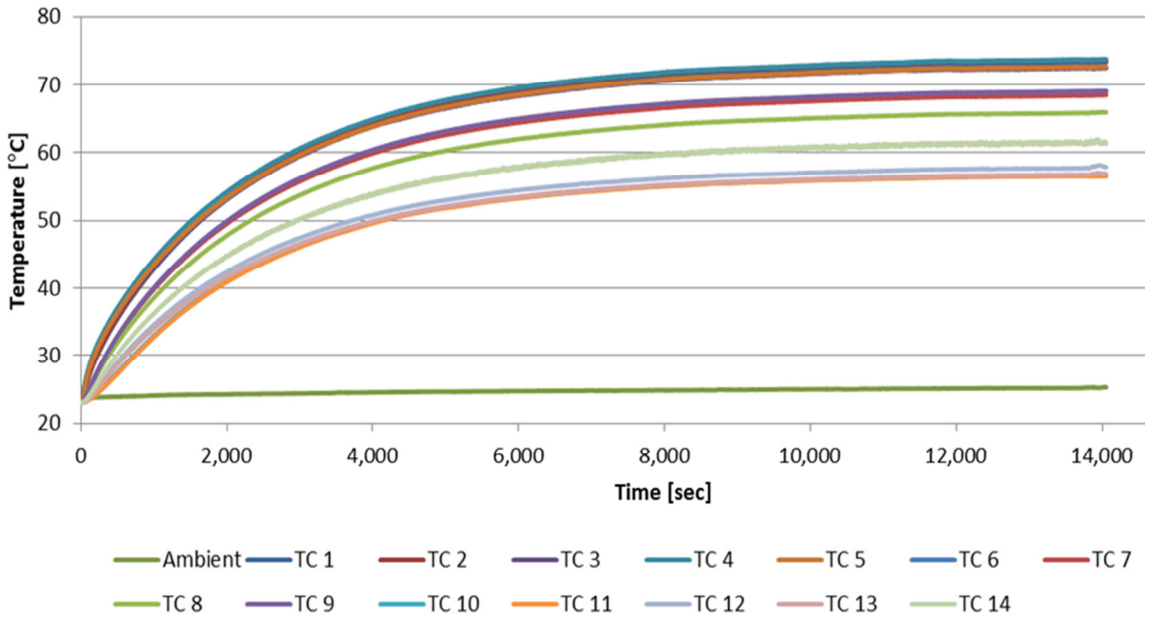

Figure 5.12 - Transient temperature data for the induction machine with no external load

The data shows the winding temperature was the highest temperatures measure as was expected. The steady state temperatures for the each winding locations was within 1 °C of the average winding temperature. This suggest that there is very little axial gradient in the windings for this case. The outer stator temperatures at each location were close in magnitude with the exception of Thermocouple 8. The lower temperature for Thermocouple 8 was seen in each of the test cases and may be due to exact thermocouple location. A lower temperature would suggest that the axial location was further away from the mid-plane than the other stator thermocouples. The thermocouples on the inner surface of the end cap suggest a heat flux direction towards the shaft due to the slightly higher temperature at the frame radius. The temperature on the outer surface of the frame is cooler than the temperatures measured on the inner surface the frame. This is expected as the outer frame location has a short direction conduction path from its location to the

winding hot spot. The inner frame locations have a heat path through the stagnant air pocket between the stator and frame or a long conduction path through the frame.

The temperature data for the friction load test is displayed in Figure 5.13. The friction test was conducted by coupling the experimental induction motor to the torque sensor and the dynamometer. No armature voltage was supplied to the dynamometer. The friction load test had an average RMS current of 1.06 A, average phase to phase voltage of 212 V, and a phase angle of 65° resulting in an input power of 164.8 W. Torque values were recorded during the test and an average value of 0.58 N-m was calculated.

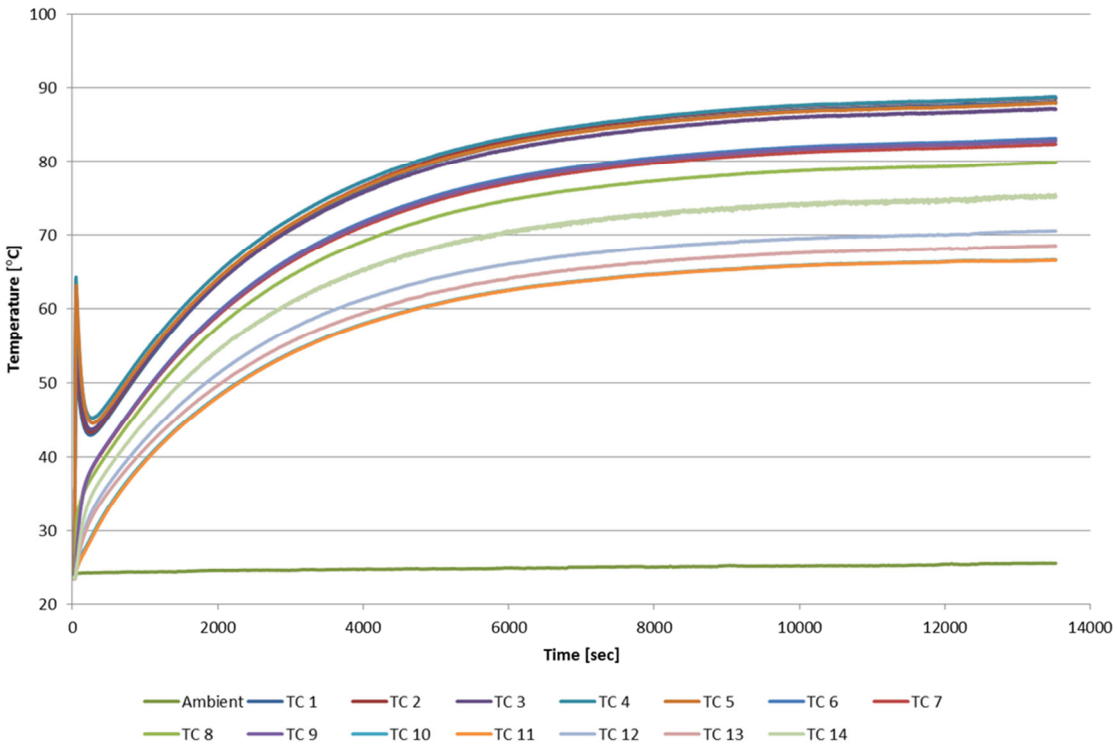

Figure 5.13 - Transient temperature data for the induction machine with friction loading

The steady state temperature values exhibited similar trends for the friction load test as were seen in the no load case include small axial variation in winding temperatures, cooler temperature at Thermocouple 8, heat flux direction towards the shaft, and frame

temperature distribution. The magnitude of the temperature gradient from the windings to the frame is slightly larger for this test. A temperature spike was observed in the transient temperature data at machine start-up. The windings in the machine were drawing larger amounts of current while the machine accelerated up to a steady state speed. The magnitude and effects of these temperature spikes is a topic for future work.

The temperature data for the 1.2 A load test is displayed in Figure 5.14. The load was set by adjusting the armature voltage supplied to the dynamometer. The 1.2 A load test had an average RMS current of 1.26 A, average phase to phase voltage of 210 V, and a phase angle of 50° resulting in an input power of 294.2 W. Torque values were recorded during the test and an average value of 1.19 N-m was calculated.

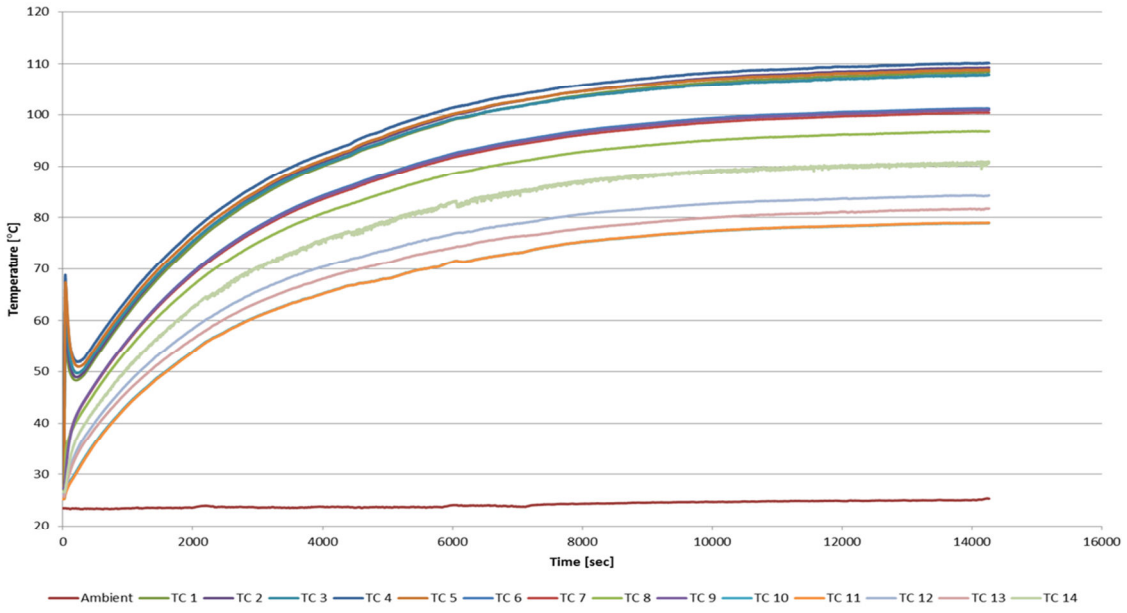

Figure 5.14 - Transient temperature data for the induction machine at 1.2 A current

The direction of heat flux in the end cap of this test was outward toward the frame. This suggests that the rotor was experiencing an increase heat load due to the increase in slip. The temperature spikes seen at the beginning of the loaded test are due to increased

current density. The magnitude of the spike becomes larger with increased load. This temperature spike and the thermal cycling effects are an interesting topic for future work.

5.4.3 Finite Difference Results Comparison

The finite difference thermal model was compared to the measured experimental temperature values. The air between the stator and frame is modeled as stagnant air. The maximum temperature values from the experimental data and the FD model for each case are displayed in Table 5.9.

Table 5.9 - Experimental loads with resulting experimental and FD maximum temperature results

Stator Copper Loss [W]	Stator Core Loss [W]	Rotor Copper Loss [W]	Rotor Core Loss [W]	Max Measured Temp [°C]	Max FD Temp [°C]	Temperature Difference	Percentage Difference
30.98	8.20	5.07	0.07	73.8	78.6	4.8	6.45%
30.94	8.13	5.02	0.07	73.0	78.4	5.4	7.36%
35.71	13.37	8.27	0.08	88.8	93.9	5.1	5.74%
43.13	15.01	9.28	0.09	97.5	104.2	6.7	6.89%
50.01	17.52	10.83	0.11	110.3	115.4	5.2	4.67%

The finite difference model was able to accurately capture the maximum temperature of the experimental machine. The maximum temperature for each test case was located at Thermocouple 4 which was located on an end winding. The measured winding temperatures at the mid-plane of the machine were at most 1.8 °C lower than the maximum temperature. Spot checks of the measured temperature values at the mid-plane of the machine give a better assessment than comparing only the maximum temperature. The FD temperature distribution results for half of the machine are displayed in Figure 5.15.

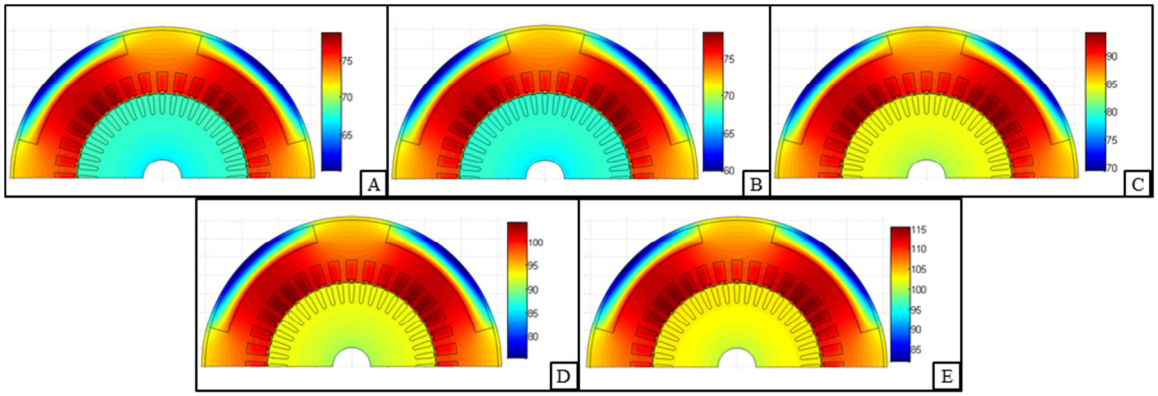

Figure 5.15 - FD temperature distribution for each of the experimental tests

Large temperature gradients can be seen in the air pockets between the stator and frame. This area was model as stagnant air with no internal heat generation. The windings radially inward to the air pocket experience the highest temperature. This is to be expected as the thermal resistance to ambient for these locations is the highest when compared to the other winding locations. A higher percentage of heat is generated in the rotor with increase loading. This explains why the ratio of the average rotor temperature to average stator temperature increases as the load increases. The FD temperature distribution was used to compare spot locations in the solution to the measured thermocouple temperature values. The temperature data for this comparison is displayed in Table 5.10.

Table 5.10 - Spot location temperature comparison for experimental and FD results

Thermocouple ID	Experimental Temperature [°C]	FD Temperature [°C]	Temperature Difference [°C]	Percentage Difference
1	73.32	78.03	4.71	6.42%
	72.56	77.82	5.26	7.25%
	88.09	93.18	5.09	5.78%
	96.34	103.30	6.96	7.22%
	108.49	114.20	5.71	5.26%
2	73.67	78.55	4.88	6.62%
	72.90	78.29	5.39	7.39%
	88.60	93.80	5.20	5.87%
	96.89	104.10	7.21	7.44%
	109.36	115.30	5.94	5.43%
6 & 7	68.78	75.67	6.90	10.03%
	67.99	74.67	6.68	9.82%
	82.76	90.21	7.46	9.01%
	89.90	99.18	9.29	10.33%
	100.88	108.20	7.33	7.26%
12 & 13	57.63	60.58	2.95	5.12%
	56.91	60.43	3.52	6.19%
	69.59	71.52	1.93	2.77%
	74.61	78.51	3.91	5.23%
	83.02	83.50	0.48	0.58%
14	61.94	72.08	10.14	16.37%
	61.16	71.88	10.72	17.53%
	75.50	85.45	9.95	13.18%
	81.42	92.40	10.98	13.49%
	91.01	103.80	12.79	14.05%

The mid-plane probe thermocouples (Thermocouples 1 and 2) were able to accurately capture the winding temperature to within 7.21 °C and 7.44%. This is within the accepted range of half the winding insulation class. The FD results over predicted the temperature which is desired in the design for protection of the winding insulation. The thermocouples on the stator outer radius (Thermocouples 6 and 7) over predict the temperature by a larger magnitude than the thermocouples on the inner radius of the

frame (Thermocouples 12 and 13). This suggests that the model is under predicting the heat transfer in the air pocket between the stator and frame. A decrease in the thermal resistance would decrease the estimated outer stator temperature and rise the inner frame temperature. This would also affect the temperature at the outer frame location (Thermocouples 14). Less heat would reach the location of Thermocouples 14 with greater heat transfer through the air pocket, thus resulting in a lower estimated temperature value. The convection on the surface of the frame is bases on an average frame temperature. The increase in heat transfer in the air pocket would decrease the temperature gradient seen in the frame and thus have smaller deviation from the average temperature used in the convection calculation.

5.5 Discussion

The finite difference thermal model discussed in this chapter was able to capture the maximum temperature to within the appropriate range. The internal heat generation values were calculated using typical values experienced in induction machines. More accurate calculation of the internal heat generation would improve the accuracy of the model. Factors such as stator and rotor flux densities, frequencies, and current values could be analytically solved in an electromagnetic simulation module. The thermal model uses correlation to describe the convection heat transfer in the air gap, on the surface of the frame, on the surface of the end caps and on the rotating surface of the shaft. These correlations are used to estimate of the heat transfer and are not meant to replace finite element analysis or computational fluid dynamics used in detailed analysis. The heat transfer in the air pocket between the stator and frame of the experimental machine is an area of uncertainty in the thermal model. The thermal model was created to estimate the

temperature in total enclosed machines but could be modified to encompass a wider variety of machines. Another area of future work is to determine a method to include internal heat generation in the bearings. The bearings become a large source of internal heat at higher speeds and loads. Linking the two separate frame and shaft thermal transport circuits into one circuit with the bearing heat generation is proposed to improve the model.

5.6 Summary

This chapter discussed the finite difference thermal model used to estimate the temperature distribution in an induction machine. Induction machines require the addition of rotor bar internal heat generation to the thermal model. The area error from the mesh and segmentation of the rotor bars was studied to determine the effects on the thermal distribution. As was expected, the rotor bars that had under predicted areas resulted in lower FD temperatures when compared to the FEA temperatures. The magnitude of the temperature difference correlated with the magnitude of the area error. An acceptable temperature error of less the 1% was achieved in each of the cases. A 3D comparison between the FD and FEA temperature distribution in the frame, stator and rotor of the machine was conducted. The finite difference thermal model slightly overestimated the maximum temperature values for a variety of different load cases. The maximum temperature difference and maximum percentage error were 9.4 °C and 8.93% respectively. Data was collected from an experimental induction machines for four different load cases and compared to the finite difference thermal solution. The finite difference thermal model was able to predict the maximum temperature to within 6.7 °C.

Spot check of the temperature distribution resulted in larger errors around the air pocket between the stator and frame of the machine.

CHAPTER 6

CONCLUSIONS

6.1 Summary and Conclusions

This work has addressed a thermal estimator for the design selection of switched reluctance and induction machines. A hybrid finite difference and thermal circuits approach was chosen to solve the temperature distribution of the machine due to its efficient use of computational power and time. The first objective was to address the mesh generation and segmentation of common rotor geometries in polar coordinates. This included how to sufficiently size the mesh nodes to accurately capture the cross section area of the features. A second objective was to develop a method for capturing the heat transfer between the stator and rotor across the air gap. The third objective was to develop a method to capture the heat rejection through the shaft to the ambient. The final objective was to create a thermal estimator for the switched reluctance and induction machines.

The mesh generation and segmentation algorithms created were able demonstrate that non-polar geometries can be modeled in polar coordinates with small percentage error in area. It was suggested that a radial step size of 0.5% of the air gap radius was adequate for a majority of features sizes. This starting step size was a balance of area accuracy and computational speed. The segmentation algorithm checks the error of the segmented feature and redefines the radial step size if the error is greater than 1%. Data showed that small angles and small feature sizes required smaller node sizing. This is due to the feature size approaching the circumferential step size of the node. Complex rotor bar

geometries were able to be modeled using a combination of the primitive feature algorithms.

The finite difference thermal model was able to capture the heat transfer in the air gap and the thermal transport from the rotor through the shaft to ambient. The convection coefficient was able to be calculated for three different flow regimes. The air gap in the finite difference model was meshed with only one radial node. The resistance values from the surface of the rotor to the center of the air gap node and the surface of the stator to the air gap node were calculated using the resulting convection heat transfer coefficient. The temperature at the center of this node (i.e. the temperature of the air gap) was solved *in situ.* A thermal circuit approach was used to capture the thermal transport from the rotor to ambient. The thermal circuit had to two parallel paths including convection from the surface of the shaft and convection on the surface of the end caps. The approach was tested using FEA and was able to predict the maximum temperature in the rotor to within 6.86 °C and an error of 4.10%.

A thermal estimator for switched reluctance machines using a hybrid finite difference approach was discussed. A 3D comparison between the FD and FEA temperature distribution in the frame, stator and rotor of the machine was conducted. The finite difference thermal model overestimated the maximum temperature values for a variety of different load cases. The maximum temperature difference and maximum percentage error were 3.80 °C and 3.78% respectively. Data was collected from an experimental switch reluctance machines for six different speed and load cases and compared to the finite difference thermal solution. The finite difference thermal model was able to predict the maximum temperature to within 10.80 °C. Spot check of the temperature distribution

showed close correlation to the FD model at two experimental locations as well as the maximum temperature.

The thermal estimator for induction machines required the addition of rotor bar internal heat generation to the thermal model. The area error from the mesh and segmentation of the rotor bars was studied to determine the effects on the thermal distribution. As was expected, the rotor bars that had under predicted areas resulted in lower FD temperatures when compared to the FEA temperatures. The magnitude of the temperature difference correlated with the magnitude of the area error. An acceptable temperature error of less the 1% was achieved in each of the cases. A 3D comparison between the FD and FEA temperature distribution in the frame, stator and rotor of the machine was conducted. The finite difference thermal model slightly overestimated the maximum temperature values for a variety of different load cases. The maximum temperature difference and maximum percentage error were 9.4 °C and 8.93% respectively. Data was collected from an experimental induction machines for four different load cases and compared to the finite difference thermal solution. The finite difference thermal model was able to predict the maximum temperature to within 6.7 °C. Spot checks of the temperature distribution resulted in larger errors around the air pocket between the stator and frame of the machine.

Pursuant to the work described here and in the previous chapters, the following conclusion can be made:

- A parametric, self-segment tool was able to capture the complex geometries found in switched reluctance or induction machines.

- An optimal starting radial node size of 0.5% of the air gap radius was found balancing computational time and segmented area accuracy.
- The shaft thermal transport was able to predict the maximum temperature in the rotor to within 6.86 °C and an error of 4.10%.
- The heat transfer in the air gap for three different flow regimes was able to be captured within the finite difference solution space by using Nusselt correlation and resulting thermal resistance values.
- The switched reluctance machine thermal estimator was able to predict the maximum temperature value to within 3.80 °C and an error of 3.78% when compared to FEA
- The switched reluctance machine thermal estimator was able to predict the maximum temperature value to within 10.80 °C when compared to experimental results
- The induction machine thermal estimator was able to predict the maximum temperature value to within 9.4 °C and an error of 8.93% when compared to FEA
- The induction machine thermal estimator was able to predict the maximum temperature value to within 6.7 °C when compared to experimental results

6.2 Contributions

In the work presented in the previous chapter, the following contributions were made:

- A parametric, self-segmenting method for defined complex geometries found in switched reluctance machine or induction machine rotors.

- A thermal circuit approach to capture the thermal transport from the rotor through the shaft to ambient.
- A unique thermal design tool for the rapid design selection for switched reluctance and induction machines.
- The following papers are currently under review
    1. C. Bednar, S. A. Semidey, and J. R. Mayor, "A Parametric, Self-Segmenting Steady State Thermal Estimation for Switched Reluctance Machines" submitted for inclusion in IET 7th International conference on Power Electronics, Machines and Drives, April 8-10 2014, Manchester, U.K.
    2. C. Bednar, S. A. Semidey, and J. R. Mayor, "A Parametric, Self-Segmenting Mesh Generation Tool for the Steady State Thermal Estimation of Induction Machines" submitted for inclusion in IET 7th International conference on Power Electronics, Machines and Drives, April 8-10 2014, Manchester, U.K.

6.3 Recommendation and Future Work

During the course of this study, several possible extensions were identified and presented here.

- Thermal model thermal circuit improvements

Further investigation into the thermal circuit of shaft and frame could be conducted. The ability to link the two individual circuits would better capture the heat transfer from the boundaries of the finite difference solution space to ambient. This would create a new heat path from the stator to the rotor to supplement the heat transfer through the air gap.

- Transient thermal modeling

Modeling of the rotor temperatures as a function of time will give a more accurate analysis of the conditions seen in a varying loads and speeds. Transient conditions, duty cycles, EPA driving cycles could all be used to enhance the design of new electric machines.

- Bearing internal heat generation and heat transfer

The thermal model used experimental data to calculate an effective thermal conductivity for the bearings. The internal heat generation within the bearing was ignored due to the low speed assumption. The bearing heat generation becomes a signification heat source at high speeds and high load conditions. The calculation of the heat transfer through the bearing is a complex problem including multiple bearing geometries, Hertzian contact, and complex fluid dynamics.

- Integration of an electromagnetic module

The inputs for the thermal model are calculated from experimental results or from manufacturer tables. The model uses average flux densities to define the core loss in the machine. An electromagnetic simulation could define the flux distribution could lead to non-uniform spatial heat generation.

- Integration of a mechanical module

The mechanical module would consider bearing and shaft sizing, static and dynamic loads, fit and tolerances, and the manufacturing aspects. The module would be able to size the machine shaft to account for beam bending, bearing sizing, rotor dynamics, and air gap interference limits. Windage losses and friction loss could also be estimated to further advance the model. Consideration of centrifugal acceleration effects leading to

magnet separation could also be studied. The thermal expansion and thermal cycling experienced in the rotor bars of induction machines could be used for reliability and life studies.

REFERENCES

[1] (2013). *Borg Warner eBooster*. Available: http://www.turbos.bwauto.com/products/eBooster.aspx Date cited: 7/25/2013.

[2] *Sirona Instruments*. Available: http://www.sirona.com/en/products/instruments/t1-line/?tab=264 Date cited: 7/25/2013.

[3] *NSK Nakanishi Electric Spindles*. Available: http://www.artcotools.com/nsk-electric-spindles/ Date cited: 7/25/2013.

[4] Y. Duan, "Method for design and optimization of surface mount permanent magnet machines and induction machines," Doctor of Philosophy, Electrical Engineering, Georgia Institute of Technology, Atlanta, GA, 2010.

[5] S. A. Semidey, "Thermal Design and Optimization of High Torque Density Electric Machines," Doctor of Philosophy, G.W. Woodruff School of Mechanical Engineering, Georgia Institute of Technology, 2012.

[6] E. M. Dede, J. Lee, Y. Liu, B. Robert, and S. H. Yonak, "Computational methods for the optimisation and design of electromechanical vehicle systems," *International Journal of Vehicle Design,* vol. 58, pp. 159-180, 2012.

[7] Y. Takano, M. Takeno, N. Hoshi, A. Chiba, M. Takemoto, S. Ogasawara*, et al.*, "Design and analysis of a switched reluctance motor for next generation hybrid vehicle without PM materials," in *2010 International Power Electronics Conference - ECCE Asia -, IPEC 2010, June 21, 2010 - June 24, 2010*, Sapporo, Japan, 2010, pp. 1801-1806.

[8] I. Ozawa, T. Kosaka, and N. Matsui, "Less rare-earth magnet-high power density hybrid excitation motor designed for hybrid electric vehicle drives," in *2009 13th European Conference on Power Electronics and Applications, EPE '09, September 8, 2009 - September 10, 2009*, Barcelona, Spain, 2009.

[9] I. Husain, "Minimization of torque ripple in SRM drives," *IEEE Transactions on Industrial Electronics,* vol. 49, pp. 28-39, 2002.

[10] V. Subrahmanyam, *Electric Drives*: The McGraw-Hill Companies, 1996.

[11] S. Kozuka, N. Tanabe, J. Asama, and A. Chiba, "Basic characteristics of 150,000r/min switched reluctance motor drive," in *IEEE Power and Energy Society 2008 General Meeting: Conversion and Delivery of Electrical Energy in the 21st Century, PES, July 20, 2008 - July 24, 2008*, Pittsburgh, PA, United states, 2008.

[12] T. J. E. Miller, "Optimal design of switched reluctance motors," *IEEE Transactions on Industrial Electronics,* vol. 49, pp. 15-27, 2002.

[13] H. J. Brauer and R. W. De Doncker, "Thermal modeling of a high-speed switched reluctance machine with axial air-gap flow for vacuum cleaners," in *2011 14th European Conference on Power Electronics and Applications, EPE 2011, August 30, 2011 - September 1, 2011*, Birmingham, United kingdom, 2011.

[14] J. Kunz, S. Cheng, D. Yao, J. R. Mayor, R. Harley, and T. Habetler, "Design of a 750,000 rpm switched reluctance motor for micro machining," in *2010 2nd IEEE Energy Conversion Congress and Exposition, ECCE 2010, September 12, 2010 - September 16, 2010*, Atlanta, GA, United states, 2010, pp. 3986-3992.

[15] P. H. Mellor, D. Roberts, and D. R. Turner, "Lumped parameter thermal model for electrical machines of TEFC design," *IEE Proceedings B: Electric Power Applications,* vol. 138, pp. 205-218, 1991.

[16] A. Boglietti, A. Cavagnino, D. A. Staton, M. Popescu, C. Cossar, and M. I. McGilp, "End space heat transfer coefficient determination for different induction motor enclosure types," *IEEE Transactions on Industry Applications,* vol. 45, pp. 929-937, 2009.

[17] D. A. Staton, M. Popescu, D. Hawkins, A. Boglietti, and A. Cavagnino, "Influence of different end region cooling arrangements on end-winding heat transfer coefficients in electrical machines," in *2010 2nd IEEE Energy Conversion Congress and Exposition, ECCE 2010, September 12, 2010 - September 16, 2010*, Atlanta, GA, United states, 2010, pp. 1298-1305.

[18] A. Boglietti, A. Cavagnino, D. A. Staton, and M. Popescu, "Experimental assessment of end region cooling arrangements in induction motor endwindings," *IET Electric Power Applications,* vol. 5, pp. 203-209, 2011.

[19] C. Kral, A. Haumer, and S. B. Lee, "Innovative thermal model for the estimation of permanent magnet and stator winding temperatures," in *4th Annual IEEE Energy Conversion Congress and Exposition, ECCE 2012, September 15, 2012 - September 20, 2012*, Raleigh, NC, United states, 2012, pp. 2704-2711.

[20] A. Boglietti, A. Cavagnino, D. Staton, M. Shanel, M. Mueller, and C. Mejuto, "Evolution and modern approaches for thermal analysis of electrical machines," 445 Hoes Lane / P.O. Box 1331, Piscataway, NJ 08855-1331, United States, 2009, pp. 871-882.

[21] H. Sun, J. Gao, Y. Dong, and Y. Zheng, "Analysis of temperature field in switched reluctance motor based on finite-element," in *11th International Conference on Electrical Machines and Systems, ICEMS 2008, October 17, 2008 - October 20, 2008*, Wuhan, China, 2008, pp. 597-601.

[22] S. Inamura, T. Sakai, and K. Sawa, "A temperature rise analysis of switched reluctance motor due to the core and copper loss by FEM," *IEEE Transactions on Magnetics,* vol. 39, pp. 1554-1557, 2003.

[23] S. Balamurugan and P. Sumathi, "Analysis of temperature rise in switched reluctance motor due to the core and copper loss by coupled field finite element analysis," in *2004 International Conference on Power System Technology, POWERCON 2004, November 21, 2004 - November 24, 2004*, Singapore, 2004, pp. 630-634.

[24] A. Boglietti, R. Bojoi, A. Cavagnino, P. Guglielmi, and A. Miotto, "Analysis and modeling of rotor slot enclosure effects in high speed induction motors," in *3rd Annual IEEE Energy Conversion Congress and Exposition, ECCE 2011, September 17, 2011 - September 22, 2011*, Phoenix, AZ, United states, 2011, pp. 154-161.

[25] C. Jungreuthmayer, T. Bauml, O. Winter, M. Ganchev, H. Kapeller, A. Haumer, *et al.*, "A detailed heat and fluid flow analysis of an internal permanent magnet synchronous machine by means of computational fluid dynamics," *IEEE Transactions on Industrial Electronics,* vol. 59, pp. 4568-4578, 2012.

[26] H. G. Park, Y. J. Kwon, S. J. Hwang, H. D. Lee, and T. S. Kwon, "A study for the estimation of temperature and thermal life of traction motor for commercial HEV," in *2012 IEEE Vehicle Power and Propulsion Conference, VPPC 2012, October 9, 2012 - October 12, 2012*, Seoul, Korea, Republic of, 2012, pp. 160-163.

[27] J. R. Mayor and S. A. Semidey, "Generic electric machine thermal model development using an," in *2009 IEEE International Electric Machines and Drives Conference, IEMDC '09, May 3, 2009 - May 6, 2009*, Miami, FL, United states, 2009, pp. 137-143.

[28] S. A. Semidey, Y. Duan, J. R. Mayor, R. G. Harley, and T. G. Habetler, "Optimal electromagnetic-thermo-mechanical integrated design candidate search and selection for surface-mount permanent-magnet machines considering load profiles," *IEEE Transactions on Industry Applications,* vol. 47, pp. 2460-2468, 2011.

[29] Y. Duan and R. G. Harley, "A novel method for multiobjective design and optimization of three phase induction machines," *IEEE Transactions on Industry Applications,* vol. 47, pp. 1707-1715, 2011.

[30] Y. Duan, R. G. Harley, and T. G. Habetler, "A useful multi-objective optimization design method for PM motors considering nonlinear material properties," in *2009 IEEE Energy Conversion Congress and Exposition, ECCE 2009, September 20, 2009 - September 24, 2009*, San Jose, CA, United states, 2009, pp. 187-193.

[31] G. I. Taylor, "Distribution of velocity and temperature between concentric rotating cylinders," *Proceedings of the Royal Society of London,* vol. 151A, pp. 494-512, 1935.

[32] H. Aoki, H. Nohira, and H. Arai, "Convective heat transfer in annulus with inner rotating cylinder," *Japan Society of Mechanical Engineers -- Bulletin,* vol. 10, pp. 523-532, 1967.

[33] K. M. Becker, "Measurements of Convective Heat Transfer From a Horizontal Cylinder Rotating in a Tank of Water," *International Journal Heat Mass Transfer,* vol. 6, pp. 1053-1062, 1963.

[34] K. V. Chalapathi Rao and V. M. K. Sastri, "Heat transfer in annulus with rotating inner cylinder," *Chemical engineering and processing,* vol. 26, pp. 173-177, 1989.

[35] S. A. Gilchrist, C. Y. Ching, and D. Ewing, "Enhanced heat transfer in a taylor-couette heat exchanger," *Journal of Enhanced Heat Transfer,* vol. 14, pp. 307-314, 2007.

[36] A. A. Kendoush, "An approximate solution of the convective heat transfer from an isothermal rotating cylinder," *International Journal of Heat and Fluid Flow,* vol. 17, pp. 439-441, 1996.

[37] Y. N. Lee and W. J. Minkowycz, "Heat transfer characteristics of the annulus of two-coaxial cylinders with one cylinder rotating," *International Journal of Heat and Mass Transfer,* vol. 32, pp. 711-22, 1989.

[38] Y. Lei and B. Farouk, "Three-dimensional mixed convection flows in a horizontal annulus with a heated rotating inner circular cylinder," *International Journal of Heat and Mass Transfer,* vol. 35, pp. 1947-56, 1992.

[39] M. Molki, K. N. Astill, and E. Leal, "Convective heat-mass transfer in the entrance region of a concentric annulus having a rotating inner cylinder," *International Journal of Heat and Fluid Flow,* vol. 11, pp. 120-8, 1990.

[40] S. Seghir-Ouali, D. Saury, S. Harmand, O. Phillipart, and D. Laloy, "Convective heat transfer inside a rotating cylinder with an axial air flow," *International Journal of Thermal Sciences,* vol. 45, pp. 1166-78, 2006.

[41] T. Sheng-Chung, "Heat transfer in a small gap between co-axial rotating cylinders," *International Communications in Heat and Mass Transfer,* vol. 33, pp. 737-43, 2006.

[42] K. S. Ball, B. Farouk, and V. C. Dixit, "Experimental study of heat transfer in a vertical annulus with a rotating inner cylinder," *International Journal of Heat and Mass Transfer,* vol. 32, pp. 1517-1527, 1989.

[43] J. Walowit and S. Tsao, "Stability of flow between arbitrarily spaced concentric cylindrical surfaces including effect of radial temperature gradient," *American Society of Mechanical Engineers -- Transactions -- Journal of Basic Engineering,* vol. 31, pp. 585-593, 1964.

[44] T. Hayase, J. A. C. Humphrey, and R. Greif, "Numerical calculation of convective heat transfer between rotating coaxial cylinders with periodically embedded cavities," *Transactions of the ASME. Journal of Heat Transfer,* vol. 114, pp. 589-97, 1992.

[45] L. Cuiping, P. Yulong, N. Ronggang, and C. Shukang, "Analysis of 3D static temperature field of water cooling induction motor in mini electric vehicle," in *2011 International Conference on Electrical Machines and Systems, ICEMS 2011, August 20, 2011 - August 23, 2011*, Beijing, China, 2011.

[46] D. A. Howey, P. R. N. Childs, and A. S. Holmes, "Air-gap convection in rotating electrical machines," *IEEE Transactions on Industrial Electronics,* vol. 59, pp. 1367-1375, 2012.

[47] Y.-S. Wang, Z. Liu, and H.-F. Zhu, "Heat generation of bearing," in *2011 International Conference on Materials Engineering for Advanced Technologies, ICMEAT 2011, May 5, 2011 - May 6, 2011*, Singapore, Singapore, 2011, pp. 962-967.

[48] A. Bairi, N. Alilat, J. G. Bauzin, and N. Laraqi, "Three-dimensional stationary thermal behavior of a bearing ball," *International Journal of Thermal Sciences,* vol. 43, pp. 561-568, 2004.

[49] K. Mizuta, T. Inoue, Y. Takahashi, S. Huang, K. Ueda, and H. Omokawa, "Heat transfer characteristics between inner and outer rings of an angular ball bearing," *Heat Transfer - Asian Research,* vol. 32, pp. 42-57, 2003.

[50] J. Takabi and M. M. Khonsari, "Experimental testing and thermal analysis of ball bearings," *Tribology International,* vol. 60, pp. 93-103, 2013.

[51] C. M. Tarawneh, A. A. Fuentes, J. A. Kypuros, L. A. Navarro, A. G. Vaipan, and B. M. Wilson, "Thermal Modeling of a Railroad Tapered-Roller Bearing Using Finite Element Analysis," *Journal of Thermal Science and Engineering Applications,* vol. 4, 2012.

[52] K. Nakajima, "Thermal contact resistance between balls and rings of a bearing under axial, radial, and combined loads," *Journal of thermophysics and heat transfer,* vol. 9, pp. 88-95, 1995.

[53] R. G. Harley, "Traditional Design of Cage Rotor Induction Motors," Y. Duan, Ed., ed. Georgia Institute of Technology, 2009.
[54] C. S. Wang, M. M. Yovanonich, and J. R. Culham, "Modeling natural convection from horizontal isothermal annular heat sinks," *Journal of Electronic Packaging, Transactions of the ASME,* vol. 121, pp. 44-49, 1999.
[55] D. Incropera, Bergman, Lavine, *Fundamentals of Heat and Mass Transfer*, 2007.
[56] *Arnold Magnetic Technologies*. Available: http://www.arnoldmagnetics.com/Non_Grain_Oriented_Electrical_Steel.aspx Date cited: 8/3/2013.
[57] *OMAX Corporation.* Available: http://www.omax.com/waterjet-cutting/machine/model/2626 Date cited: 8/3/2013.
[58] S. Williamson and C. I. McClay, "Optimization of the geometry of closed rotor slots for cage induction motors," *IEEE Transactions on Industry Applications,* vol. 32, pp. 560-568, 1996.
[59] *Electric Motors - Fractional Motors - Three-Phase: NEMA 56 Frame - ODP*. Available: http://www.weg.net/us/Products-Services/Electric-Motors/Fractional-Motors/Three-Phase-NEMA-56-Frames-ODP Date cited: 8/26/2013.